Small Scales, Vast Ocean

Submesoscale Ocean Topography with Bistatic Synthetic-aperture Radar Interferometry

Theodosiou, A.

DOI
10.4233/uuid:d42be52f-b322-4a99-9ae9-9845225aaffe

Publication date
2025

Document Version
Final published version

Citation (APA)
Theodosiou, A. (2025). *Small Scales, Vast Ocean: Submesoscale Ocean Topography with Bistatic Synthetic-aperture Radar Interferometry*. [Dissertation (TU Delft), Delft University of Technology]. https://doi.org/10.4233/uuid:d42be52f-b322-4a99-9ae9-9845225aaffe

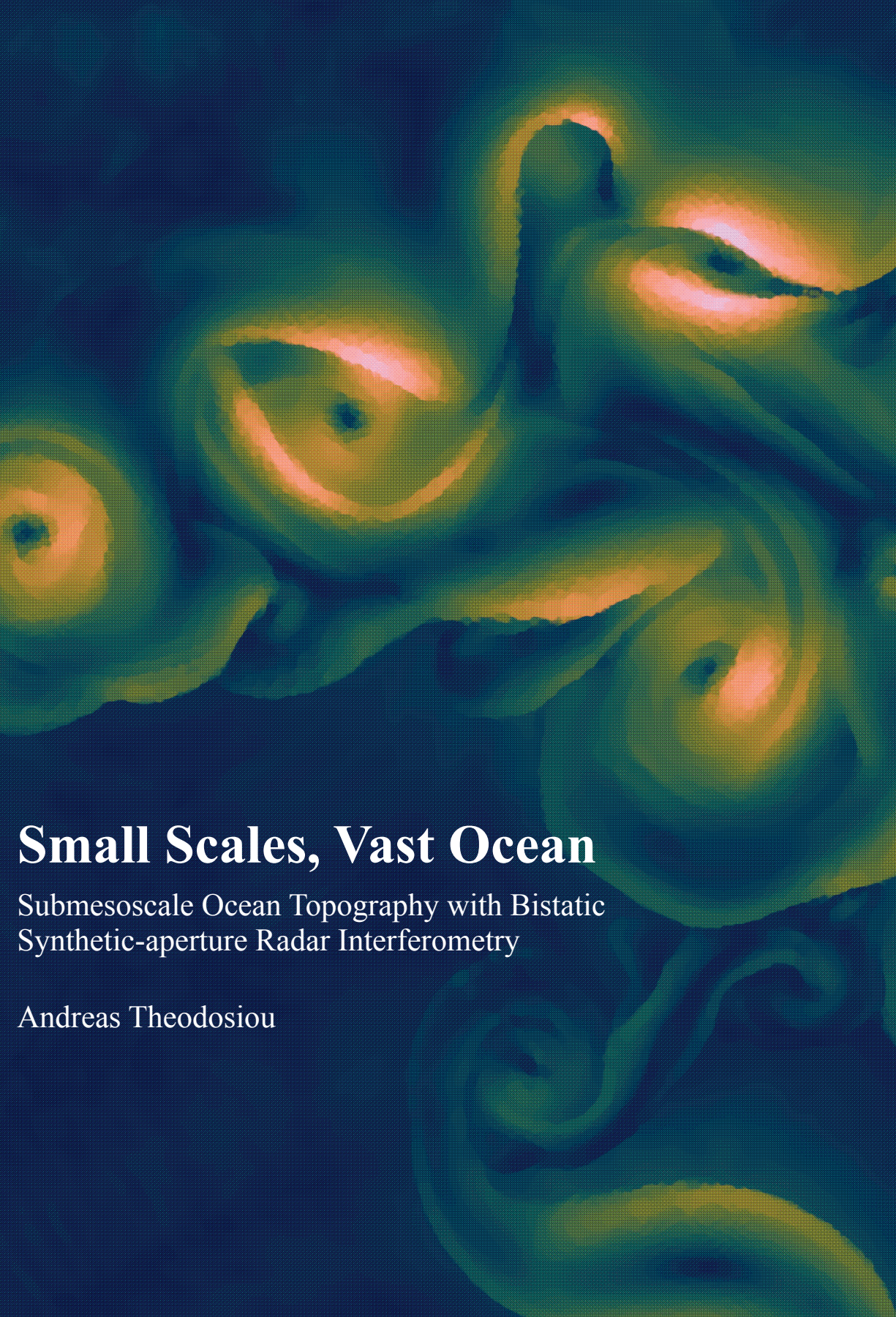

Small Scales, Vast Ocean

Submesoscale Ocean Topography with Bistatic Synthetic-aperture Radar Interferometry

Andreas Theodosiou

Small Scales, Vast Ocean

Submesoscale Ocean Topography with Bistatic Synthetic-aperture Radar Interferometry

Small Scales, Vast Ocean

Submesoscale Ocean Topography with Bistatic Synthetic-aperture Radar Interferometry

Dissertation

for the purpose of obtaining the degree of doctor
at Delft University of Technology
by the authority of the Rector Magnificus, prof. dr. ir. T.H.J.J. van der Hagen,
chair of the Board for Doctorates
to be defended publicly on
Tuesday 16 September 2025 at 10:00 o'clock

by

Andreas THEODOSIOU

Master of Engineering,
University of Cambridge, United Kingdom,
born in Egkomi, Cyprus.

This dissertation has been approved by the promotors.

Composition of the doctoral committee:

Rector Magnificus,	chairperson
Prof. dr. ir. R.F. Hanssen	Delft University of Technology, *promotor*
Prof. dr. ir. F. López-Dekker	Delft University of Technology, *promotor*

Independent members:

Prof. dr. J.J. Mallorqui Franquet	Universitat Politècnica de Catalunya, Spain
Dr. D. Moller	University of Auckland, New Zealand
Dr. -Ing. M. Rodríguez-Cassolà	Deutsches Zentrum für Luft- und Raumfahrt, Germany
Prof. dr. S. Tebaldini	Politecnico di Milano, Italy
Prof. dr. A. Yarovoy	Delft University of Technology
Prof. dr. ir. S.C. Steele-Dunne	Delft University of Technology, reserve member

Keywords: synthetic-aperture radar, synthetic-aperture radar interferometry, cross-track interferometry, wide-swath ocean altimetry, submesoscale currents, data-driven calibration, data-driven phase synchronization, bistatic synthetic-aperture radar

Printed by: Ridderprint

Cover: Velocity field of a baroclinically unstable front, simulated using Oceananigans.jl. Layout by Ridderprint.

ISBN 978-94-6384-828-2

An electronic copy of this dissertation is available at
https://repository.tudelft.nl/.

Πάντα χωρεῖ καὶ οὐδὲν μένει - All is flow, nothing is stationary.

Plato's Cratylus, 402a

Contents

Summary

Ocean surface topography (OST), the hills and valleys of the ocean surface, provides information on several physical phenomena at different spatial and temporal scales. At scales between $100\,\mathrm{km}$ and $500\,\mathrm{km}$, the mesoscales, the currents of the ocean flow between the topographic highs and lows. OST measurements from nadir radar altimeters have facilitated the study of the mean oceanic flow and substantially improved oceanographic knowledge. At the smaller submesoscales, $10\,\mathrm{km}$ to $100\,\mathrm{km}$, variations of the OST are related to eddies and fronts. Additionally, tropical and extratropical cyclones produce strong disturbances of the surface topography. At the lower end of the submesoscales, with wavelengths of only a few kilometers, internal waves produced by the interaction of tidal currents and bottom topography leave perturbations on the height of the surface.

There is growing evidence that submesoscale eddies, and fronts are crucial in the transport of energy, mixing of heat and nutrients, and the sea state. Furthermore, scientists have inferred that a proportion of tidal energy is dissipated in the form of internal waves. Several processes, related to tropical and extratropical cyclones, are poorly parameterized due to a lack of observations. Observations of the OST at the submesoscales are crucial in helping scientists study these phenomena.

Synthetic-aperture radar (SAR) is a unique remote sensing instrument, particularly at C-band, capable of sensing the ocean surface at the submesoscales, with a wide swath, and in nearly all weather conditions. Harmony, the European Space Agency's 10th Earth Explorer, features two SAR companion satellites. Two, out of a total of five, years of the mission's life will be spent in a formation where the system will operate as a cross-track interferometer. Cross-track interferometry (XTI) is a technique that estimates the relative height of the surface from two SAR images of the same scene. Thus, Harmony could theoretically retrieve variations of the OST. In other words, the system could operate as a bistatic wide-swath ocean altimeter (WSOA). At the same time, Harmony will retrieve stress-equivalent wind fields, and instantaneous surface currents. Therefore, Harmony has the potential of providing an unprecedented wealth of co-located simultaneous data related to the ocean and the atmosphere. The aim of this thesis is to devise a method to estimate submesoscale ocean surface topography with a bistatic SAR interferometer, such as Harmony.

Estimating the relative topography, the relative sea-surface height (RSSH), from SAR images using XTI is challenging when the radars operate bistatically with a squinted line of sight, as is the case for Harmony. Although performing XTI to estimate land topography is part of Harmony's requirements, this does not ensure that retrieving ocean topography with the same technique is feasible. There are

two factors that complicate the retrieval of ocean topography: the dynamism of the surface, and the small dynamic range of the geophysical signal.

XTI combines two SAR images taken from two locations with a cross-track separation to estimate the relative height of the surface. If the surface moves during the elapsed time between the acquisition of the two images, then the two images lose coherence from one another and the interferometric estimate is noisy. Thus, a key challenge in designing a bistatic WSOA is to reduce the temporal lag between acquisitions sufficiently to minimize loss of coherence without reducing the along-track separation of the satellite companions to the point where there is risk of collision. At the same time, since the dynamic range of the geophysical signal is small, the instrument sensitivity should be maximized.

Assessing the design of a bistatic WSOA requires knowledge of the interferometric sensitivity, and temporal lag. The first obstacle that we encountered was that there is no model or analytical expression for these parameters that apply to a bistatic SAR with a squinted line of sight. The established relations found in the literature assume a zero-squint geometry. Hence, we use the Fourier Diffraction Slice Theorem to derive an analytical expression for the interferometric sensitivity, and the temporal lag. We show that forming an interferogram aligns the regions of support of the two images in the Fourier domain at each resolution cell, and that the temporal lag is the time offset that aligns the two regions. The sensitivity is equal to the vertical component of the aligned wave vectors projected on the elevation direction. We verify our results using simulations and confirm that our analytical expressions agree with the well-established relations for sensitivity and temporal lag for zero-squint systems.

We use the analytical expressions of sensitivity and temporal lag to build an interferometric performance model that computes the standard error of the height estimate for a formation-flying cross-track interferometer. The model considers the following random error sources: temporal decorrelation, thermal noise, spectral shift, volumetric decorrelation, and the effect of removing the phase due to motion of the surface using the individual phase centers of the instruments. Additionally, we derive a relation between the formation parameters that, when satisfied, minimizes the effective temporal lag, while maximizing the interferometric sensitivity. We then proceed to assess the performance over an orbit and along the $250\,\mathrm{km}$-swath of an optimized formation.

Our findings show that Harmony can achieve a standard error of $1\,\mathrm{cm}$ to $8\,\mathrm{cm}$ over the entire swath at a wind speed of $5\,\mathrm{m\,s^{-1}}$, except for towards the poles. By converting the error to a spectral noise floor and comparing it to models of the OST's power spectral density, we translate the performance to spatial scales of $38.7\,\mathrm{km}$ to $36.4\,\mathrm{km}$ depending on the slope of the spectral model. The resolution improves with wind speed because the instrument performance is noise-driven, and in the Bragg scattering regime electromagnetic scattering increases with surface roughness, which increases with wind. At $10\,\mathrm{m\,s^{-1}}$ Harmony resolves OST at wavelengths of $26\,\mathrm{km}$ to $11\,\mathrm{km}$ depending on the spectral slope.

In addition to the random errors, we assess the effect of systematic errors on the performance. We provide models for the effect of the tropospheric path delay on

the interferometric height estimate, for baseline errors, and set a maximum phase synchronization error that would allow retrieval of heights at the submesoscales. The error budget allocation for the synchronization error is $1\,\mathrm{cm}$, which translates to 0.045° of phase at C-band. Finally, we mathematically analyze the sea-state bias in depth and show that the bias depends on the integral of the product of the modulation transfer function and the surface elevation variance spectrum.

Simulations based on the aforementioned error budget suggest that Harmony, and other bistatic radar satellite formations with similar design, can resolve submesoscale topography. However, recent studies suggest that Harmony's global navigation system (GNSS)-based synchronization scheme reduces the synchronization error to approximately 1.6°; leaving a residual two orders of magnitude larger than the synchronization error allocation in Harmony's OST error budget. We devise a data-driven synchronization algorithm to eliminate the phase synchronization residual that remains post-GNSS correction.

The algorithm uses multisquint processing and the difference in interferometric phase between regions that are sampled twice with a small time lag to estimate the derivative of the residual, and integrates the derivative to obtain an estimate of the residual. The algorithm achieves an unbiased root mean square error of 0.010°, reducing the phase synchronization error to within the error budget allocation. We use the wind, currents, ocean topography, significant wave height, and directional wave spectra from ocean-atmosphere coupled models to simulate the RSSH retrieval over a realistic scene. Our simulations confirm that before the data-driven calibration the synchronization residual dominates the signal, making the retrieval of RSSH extremely challenging, while retrieval after calibrating the data with the proposed algorithm becomes possible, and is only limited by instrument noise.

Overall, the thesis presents how one can design, analyze, and retrieve relative ocean topography at the submesoscales with a bistatic SAR interferometer. It sets the foundations for an experimental OST product for the Harmony mission. Adding such a product to the mission would offer the first simultaneously acquired observations of wind field, current field, directional wave spectrum, and relative sea-surface height at high resolution and over a $250\,\mathrm{km}$-wide swath.

Samenvatting

Topografie van het oceaanoppervlak (Ocean surface topography, OST), de heuvels en dalen van het oceaanoppervlak, geeft inzicht in verschillende fysische fenomenen op verschillende ruimtelijke en temporele schalen. Op schalen tussen $100\,\mathrm{km}$ en $500\,\mathrm{km}$, de zogenaamde submesoscales, bewegen de zeestromen zich tussen de heuvels en dalen van de oceaan. Metingen van de OST door nadir altimeters hebben de studie van de gemiddelde oceaanstroming mogelijk gemaakt en de oceanografische kennis substantieel verbeterd. Op de kleinere submesoscales, $10\,\mathrm{km}$ tot $100\,\mathrm{km}$, zijn variaties van de OST gerelateerd aan eddies en fronten. Daarnaast veroorzaken tropische en extratropische cyclonen sterke verstoringen van de oppervlaktetopografie. Aan de onderkant van de submesoscales, met golflengtes van slechts een paar kilometer, laten inwendige golven, geproduceerd door de interactie van getijdenstromingen en bodemtopografie, verstoringen achter op de hoogte van het oppervlak.

Er is steeds meer bewijs dat submesoscale eddies en fronten cruciaal zijn voor het transport van energie, het mengen van warmte en voedingsstoffen en de staat van de zee. Bovendien hebben wetenschappers afgeleid dat een deel van de getijdenenergie verloren gaat in de vorm van inwendige golf. Verschillende processen die verband houden met tropische en extratropische cyclonen zijn slecht geparametriseerd door een gebrek aan metingen. Metingen van de OST op submesoscales zijn cruciaal om wetenschappers te helpen deze fenomenen te bestuderen.

Synthetic-aperture radar (SAR) is een uniek remote sensing instrument, vooral in C-band, waarmee het oceaanoppervlak op submesoscales kan worden waargenomen, met een grote swath en in bijna alle weersomstandigheden. Harmony, de 10e Earth Explorer van het Europees Ruimteagentschap, bestaat uit twee SAR-satellieten. Twee van de in totaal vijf jaar van de levensduur van de missie zullen worden doorgebracht in een formatie waarin het systeem zal werken als een cross-track interferometer. Cross-track interferometry (XTI) is een techniek die de relatieve hoogte van het oppervlak schat uit twee SAR-beelden van dezelfde scène. Harmony zou dus theoretisch variaties van de OST kunnen schatten. Met andere woorden, het systeem zou kunnen werken als een bistatische wide-swath ocean altimeter (WSOA). Tegelijkertijd zal Harmony stres-equivalente windvelden en instantane zeestromen schatten. Daarom heeft Harmony het potentieel om een ongekende rijkdom aan gelijktijdige gegevens vanaf dezelfde locatie over de oceaan en de atmosfeer te leveren. Het doel van dit proefschrift is om een methode te ontwikkelen om de topografie van het oceaanoppervlak op de submesoscales te schatten met een bistatische SAR-interferometer, zoals Harmony.

Het schatten van de relatieve topografie, de relatieve hoogte van het zeeoppervlak (RSSH) genoemd, uit SAR-beelden met behulp van XTI is een uitdaging als de

radars bistatisch werken met een squinted line of sight, zoals het geval is bij Harmony. Hoewel het uitvoeren van XTI om landtopografie te schatten deel uitmaakt van de Harmony-vereisten, garandeert dit niet dat het schatten van oceaantopografie met dezelfde techniek mogelijk is. Er zijn twee factoren die het schatten van oceaantopografie ingewikkeld maken: De dynamiek van het oppervlak; het kleine dynamische bereik van het geofysische signaal.

XTI combineert twee SAR-beelden afkomstig van twee locaties met een cross-track afstand om de relatieve hoogte van het oppervlak te schatten. Als het oppervlak beweegt tijdens de tijd die verstrijkt tussen de opnames van de twee beelden, verliezen de twee beelden hun onderlinge coherentie en is de interferometrische schatting noisy. Een belangrijke uitdaging bij het ontwerpen van een bistatische WSOA is dus om het tijdsverschil tussen de opnames voldoende te verkleinen om het verlies aan coherentie te minimaliseren zonder de along-track afstand tussen de satellieten zodanig te verkleinen dat er een risico op botsingen ontstaat. Tegelijkertijd moet de gevoeligheid van het instrument worden gemaximaliseerd omdat het dynamische bereik van het geofysische signaal klein is.

Het beoordelen van het ontwerp van een bistatische WSOA vereist kennis van de interferometrische gevoeligheid en de temporele lag. Het eerste obstakel dat we tegenkwamen was het ontbreken van een model of analytische uitdrukking voor deze parameters die van toepassing zijn op een bistatische SAR met een squinted line of sight. De gevestigde relaties die we in de literatuur vinden, gaan uit van een geometrie met een zero squint. Daarom gebruiken we de Fourier Diffraction Slice Theorem om een analytische uitdrukking af te leiden voor de interferometrische gevoeligheid en de temporele lag. We laten zien dat het vormen van een interferogram het support van de twee beelden in het Fourier-domein uitlijnen bij elke resolutiecel en dat de temporele lag het tijdsverschil is dat de twee supports uitlijnen. De gevoeligheid is gelijk aan de verticale component van de uitgelijnde golfvectoren geprojecteerd op de hoogterichting. We verifiëren onze resultaten met behulp van simulaties en bevestigen dat onze analytische uitdrukkingen overeenkomen met de gevestigde relaties voor gevoeligheid en temporele lag voor een zero-squint system.

We gebruiken de analytische uitdrukkingen van gevoeligheid en temporele lag om een interferometrisch prestatiemodel op te stellen dat de standaardfout van de hoogteschatting berekent voor een interferometer die in formatie vliegt. Het model houdt rekening met de volgende willekeurige foutbronnen: temporele decorrelatie, thermische ruis, spectrale verschuiving, volumetrische decorrelatie en het effect van het verwijderen van de fase door beweging van het oppervlak met behulp van de individuele fasecenters van de instrumenten. Daarnaast leiden we een relatie af tussen de formatieparameters die, als eraan voldaan wordt, de effectieve temporele lag minimaliseert en tegelijkertijd de interferometrische gevoeligheid maximaliseert. Vervolgens beoordelen we de prestaties voor een rotatie om de aarde en langs de $250\,\mathrm{km}$ lange swath van een geoptimaliseerde formatie.

Onze bevindingen laten zien dat Harmony een standaardfout van $1\,\mathrm{cm}$ tot $8\,\mathrm{cm}$ bereiken over het hele swath bij een windsnelheid van 5 m/s, behalve in de richting van de polen. Door de fout om te rekenen naar een spectrale noise floor en

deze te vergelijken met modellen van de power spectral density van de OST, vertalen we de prestaties naar ruimtelijke schalen van $38.7\,\mathrm{km}$ tot $36.4\,\mathrm{km}$, afhankelijk van de spectral slope. De resolutie verbetert met de windsnelheid omdat de prestaties van het instrument worden bepaald door ruis en in het Bragg-regime neemt de elektromagnetische scattering toe met de surface roughness, die toeneemt met de wind. Bij $10\,\mathrm{m\,s^{-1}}$ lost Harmony OST op golflengten van $26\,\mathrm{km}$ tot $11\,\mathrm{km}$ op, afhankelijk van de spectral slope.

Naast de willekeurige fouten beoordelen we het effect van systematische fouten op de prestaties. We produceren modellen voor het effect van de troposferische path delay op de interferometrische hoogteschatting, voor baseline errors en stellen een maximale fase synchronisatiefout vast waarmee hoogtes op submesoscales kunnen worden geschat. Het foutenbudget voor de synchronisatiefout is $1\,\mathrm{cm}$, wat overeenkomt met $0.045°$ van de fase op C-band. Tot slot analyseren we op wiskundige wijze de bias van de zeestaat en laten we zien dat de bias afhangt van de integraal van het product van de modulation transfer function en het spectrum van de surface elevation.

Simulaties gebaseerd op het bovengenoemde foutenbudget suggereren dat Harmony, en andere bistatische radarsatellietformaties met een vergelijkbaar ontwerp, topografie op submesoscales kunnen schatten. Recente studies suggereren echter dat het op het Global Navigation Satellite System (GNSS) gebaseerde synchronisatie van Harmony de synchronisatiefout vermindert tot ongeveer $1.6°$; er blijft een residu dat twee ordes van grootte groter is dan de synchronisatiefout die is toegewezen in het OST-foutenbudget van Harmony. We ontwikkelen een data-driven synchronisatiealgoritme om het fasesynchronisati residu dat overblijft na de GNSS-correctie te elimineren.

Het algoritme gebruikt multisquint processing en het verschil in interferometrische fase tussen gebieden die twee keer gesampled worden met een klein tijdsverschil, om de afgeleide van het residu te schatten, en integreert de afgeleide om een schatting van het residu te verkrijgen. Het algoritme bereikt een gemiddelde unbiased fout van $0.010°$, waardoor de fasesynchronisatie error binnen het toegewezen foutbudget blijft. We gebruiken de wind, zeestromen, oceaantopografie, significante golfhoogte en directionele golfspectra van oceaan-atmosfeer gekoppelde modellen om het schatten van RSSH over een realistische scène te simuleren. Onze simulaties bevestigen dat voorafgaand aan de data-driven kalibratie het synchronisatieresidu het signaal domineert, waardoor het schatten van RSSH extreem uitdagend wordt, terwijl het schatten na kalibratie van de data met het voorgestelde algoritme mogelijk wordt en alleen beperkt wordt door instrument noise.

In het algemeen laat dit proefschrift zien hoe men relatieve oceaantopografie op submesoscales kan ontwerpen, analyseren en ophalen met een bistatische SAR-interferometer. Het legt de basis voor een experimenteel OST-product voor de Harmony-missie. Het toevoegen van zo'n product aan de missie zou de eerste gelijktijdig verkregen metingen van windveld, stromingsveld, directioneel golfspectrum en relatieve hoogte van het zeeoppervlak bieden met een hoge resolutie en over een $250\,\mathrm{km}$ brede swath.

Σύνοψη

Η ωκεανική επιφανειακή τοπογραφία (Ocean Surface Topography OST), η διακύμανση της θαλάσσιας στάθμης σε σχέση με το γεωειδές, παρέχει πληροφορίες σχετικά με πολλά φυσικά φαινόμενα σε διάφορες χωρικές και χρονικές κλίμακες. Στις κλίμακες μεταξύ $100\,\mathrm{km}$ και $500\,\mathrm{km}$, επίσης γνωστές ως μεσαίες κλίμακες, τα ωκεανικά ρεύματα ρέουν ανάμεσα στους λόφους και τις κοιλάδες της επιφάνειας. Οι μετρήσεις της ωκεανικής επιφανειακής τοπογραφίας από δορυφορικά αλτίμετρα έχουν καταστήσει τη μελέτη της μέσης ωκεανικής ροής δυνατή και έχουν εξελίξει την ωκεανογραφική γνώση σε αξιοσημείωτο βαθμό. Στις μικρότερες, ούτω καλούμενες υπομεσαίες, κλίμακες μεταξύ $10\,\mathrm{km}$ με $100\,\mathrm{km}$, οι διακυμάνσεις της τοπογραφίας σχετίζονται με θαλάσσιες δίνες και μέτωπα. Επίσης, οι τροπικοί και εξωτροπικοί κυκλώνες προκαλούν ισχυρές διαταραχές στο ύψος της επιφάνειας. Στο χαμηλό όριο των υπομεσαίων κλιμάκων, όπου τα φυσικά φαινόμενα έχουν μήκος κύματος μερικών μόλις χιλιομέτρων, τα παλιρροϊκά ρεύματα αλληλεπιδρούν με τα εσωτερικά κύματα και αφήνουν το αποτύπωμα τους στην επιφάνεια υπό τη μορφή υψομετρικών διακυμάνσεων.

Υπάρχουν αυξανόμενα στοιχεία ότι οι δίνες και τα μέτωπα με μεγέθη υπομεσαίας κλίμακας είναι κρίσιμα στη μεταφορά ενέργειας, στην ανάμιξη θερμότητας και θρεπτικών ουσιών, και στην κατάσταση θαλάσσης. Επιπλέον, οι επιστήμονες έχουν συμπεράνει πως μέρος της παλιρροϊκής ενέργειας διαχέεται υπό τη μορφή εσωτερικών κυμάτων. Αρκετές φυσικές διαδικασίες που σχετίζονται με τροπικούς και εξωτροπικούς κυκλώνες, είναι ελλιπώς παραμετροποιημένες λόγω έλλειψης μετρήσεων. Μετρήσεις της ωκεανικής τοπογραφίας στις υπομεσαίες κλίμακες είναι αναγκαίες για τη μελέτη αυτών των φαινομένων.

Το ραντάρ συνθετικού ανοίγματος (synthetic-aperture radar SAR) είναι ένα μοναδικό όργανο τηλεπισκόπησης, ειδικά στη ζώνη συχνότητας C, που δύναται να ανιχνεύσει την ωκεανική επιφάνεια στις υπομεσαίες κλίμακες, με μεγάλο εύρος και σε σχεδόν όλες τις καιρικές συνθήκες. Η αποστολή Harmony, το δέκατο Earth Explorer του Ευρωπαϊκού Οργανισμού Διαστήματος (ΕΟΔ), αποτελείται από δύο δορυφόρους SAR. Στα δύο από τα πέντε χρόνια ζωής της αποστολής, οι δορυφόροι θα είναι σε σχηματισμό μεταξύ τους επιτρέποντάς τους να λειτουργούν ως ένα εγκάρσιο συμβολόμετρο. Η εγκάρσια συμβολομετρία (cross-track interferometry XTI) είναι μία τεχνική που εκτιμά το σχετικό ύψος της επιφάνειας από δύο εικόνες SAR της ίδιας περιοχής. Επομένως, η Harmony θα έχει, θεωρητικά, τη δυνατότητα να εκτιμήσει τις μεταβολές του OST. Με άλλα λόγια, το σύστημα θα μπορούσε να λειτουργήσει ως ένα διστατικό ωκεανικό αλτίμετρο μεγάλου πλάτους (wide-swath ocean altimeter WSOA). Ταυτόχρονα, η Harmony θα μετρά πεδία τασικού αντίστοιχου ανέμου και επιφανειακά ρεύματα. Άρα, η Harmony θα έχει τη δυνατότητα να παρέχει έναν άνευ προηγουμένου πλούτο

ταυτόχρονων ταυτόχωρων (στην ίδια τοποθεσία) ωκεανικών και ατμοσφαιρικών δεδομένων. Ο στόχος αυτής της διατριβής είναι η επαγωγή μίας μεθόδου εκτίμησης της ωκεανικής τοπογραφίας υπομεσαίας κλίμακας με τη χρήση ενός διστατικού συμβολόμετρου SAR, όπως το Harmony.

Η εκτίμηση της σχετικής τοπογραφίας, το σχετικό ύψος της επιφάνειας της θάλασσας (RSSH), από εικόνες SAR μέσω του XTI αποτελεί πρόκληση όταν τα ραντάρ λειτουργούν διστατικά με λοξή (μη κάθετη στην κατεύθυνση κίνησης του δορυφόρου) οπτική γραμμή, όπως συμβαίνει στο Harmony. Ενώ η χρήση του XTI για την εκτίμηση της τοπογραφίας στη στεριά αποτελεί μέρος των απαιτήσεων του Harmony, αυτό δεν εξασφαλίζει ότι η εκτίμηση της ωκεανικής τοπογραφίας με την ίδια τεχνική είναι εφικτή. Υπάρχουν δύο παράγοντες που περιπλέκουν την εκτίμηση της ωκεανικής τοπογραφίας: Η κίνηση της επιφάνειας, και το μικρό δυναμικό εύρος του γεωφυσικού σήματος.

Το XTI συνδυάζει δύο εικόνες SAR της ίδιας περιοχής που έχουν ληφθεί από δύο τοποθεσίες με κάθετη γραμμή βάσης για να εκτιμήσει το σχετικό ύψος της επιφάνειας. Εάν η επιφάνεια κινείται κατά τη διάρκεια του χρόνου που μεσολαβεί μεταξύ της λήψης των δύο εικόνων, τότε οι δύο εικόνες χάνουν τη συνοχή τους και η συμβολομετρική εκτίμηση γίνεται θορυβώδης. Έτσι, μια βασική πρόκληση στον σχεδιασμό ενός διιστατικού WSOA είναι η μείωση της χρονικής υστέρησης μεταξύ των λήψεων αρκετά ώστε να ελαχιστοποιηθεί η απώλεια συνοχής χωρίς να μειωθεί ο διαχωρισμός κατά μήκος της τροχιάς των δορυφόρων σε σημείο που να υπάρχει κίνδυνος σύγκρουσης. Ταυτόχρονα, καθώς το δυναμικό εύρος του γεωφυσικού σήματος είναι μικρό, η ευαισθησία του οργάνου πρέπει να μεγιστοποιηθεί.

Η αξιολόγηση του σχεδιασμού ενός διστατικού WSOA απαιτεί τη γνώση της συμβολομετρικής ευαισθησίας και της χρονικής υστέρησης. Το πρώτο εμπόδιο που συναντήσαμε ήταν ότι αυτές οι παράμετροι δεν έχουν κάποιο μοντέλο ή αναλυτική παράσταση που να ισχύει στην περίπτωση ενός διστατικού SAR με λοξή οπτική γραμμή, καθώς οι υπάρχουσες παραστάσεις στη βιβλιογραφία υποθέτουν μία γεωμετρία χωρίς λοξή οπτική γραμμή. Ως εκ τούτου, χρησιμοποιούμε το θεώρημα Fourier Diffraction Slice για να εξάγουμε μια αναλυτική έκφραση για τη συμβολομετρική ευαισθησία και τη χρονική υστέρηση. Δείχνουμε ότι η δημιουργία ενός συμβολογραφήματος ευθυγραμμίζει το πεδίο υποστήριξης των δύο εικόνων, στο πεδίο Fourier, σε κάθε κελί και ότι η χρονική υστέρηση είναι η χρονική μετατόπιση που ευθυγραμμίζει τα δύο πεδία. Η ευαισθησία είναι ίση με την προβολή της κάθετης συνιστώσας της διαφοράς των ευθυγραμμισμένων διανυσμάτων κύματος στην κατεύθυνση του ύψους. Επαληθεύουμε τα αποτελέσματά μας χρησιμοποιώντας προσομοιώσεις και επιβεβαιώνουμε ότι οι αναλυτικές εξισώσεις συμφωνούν με τις καθιερωμένες σχέσεις για την ευαισθησία και τη χρονική υστέρηση για συστήματα μηδενικής λοξότητας.

Χρησιμοποιούμε τις αναλυτικές παραστάσεις της ευαισθησίας και της χρονικής υστέρησης για να ορίσουμε ένα μοντέλο συμβολομετρικής απόδοσης που υπολογίζει το τυπικό σφάλμα της εκτίμησης του ύψους ενός εγκάρσιου συμβολόμετρου που αποτελείται από δορυφόρους σε σχηματισμό. Το μοντέλο λαμβάνει υπόψη τις ακόλουθες τυχαίες πηγές σφαλμάτων: χρονική αποσυσχέτιση,

θερμικό θόρυβο, φασματική μετατόπιση, ογκομετρική αποσυσχέτιση, και την επίδραση της αφαίρεσης της φάσης λόγω της κίνησης της επιφάνειας χρησιμοποιώντας τα ξεχωριστά κέντρα φάσης των οργάνων. Επιπλέον, εξάγουμε μια σχέση μεταξύ των παραμέτρων σχηματισμού που όταν ικανοποιείται ελαχιστοποιεί τη χρονική υστέρηση, ενώ μεγιστοποιεί τη συμβολομετρική ευαισθησία. Στη συνέχεια, προχωρούμε στην αξιολόγηση της απόδοσης σε μια τροχιά και κατά μήκος του πλάτους εικόνας $250\,\mathrm{km}$ ενός βελτιστοποιημένου σχηματισμού.

Τα ευρήματά μας δείχνουν ότι το Harmony μπορεί να επιτύχει ένα τυπικό σφάλμα $1\,\mathrm{cm}$ με $8\,\mathrm{cm}$ όταν η ταχύτητα ανέμου ισούται με $5\,\mathrm{m\,s^{-1}}$ σε ολόκληρη την τροχιά, με εξαίρεση τις πολικές περιοχές. Μετατρέποντας το σφάλμα σε φασματικό θόρυβο και συγκρίνοντας το με μοντέλα της φασματικής πυκνότητας ισχύος του OST, μεταφράζουμε την απόδοση στη δυνατότητα του οργάνου να διακρίνει χωρικές κλίμακες $38.7\,\mathrm{km}$ με $36.4\,\mathrm{km}$, ανάλογα της κλίσης του φασματικού μοντέλου. Η ανάλυση βελτιώνεται με την ταχύτητα του ανέμου επειδή η απόδοση του οργάνου εξαρτάται από το θόρυβο και στο καθεστώς σκέδασης Bragg η ηλεκτρομαγνητική σκέδαση αυξάνεται με την τραχύτητα της επιφάνειας, η οποία αυξάνεται με τον άνεμο. Σε $10\,\mathrm{m\,s^{-1}}$ το Harmony διακρίνει το OST σε μήκη κύματος $26\,\mathrm{km}$ με $11\,\mathrm{km}$ ανάλογα της φασματικής κλίσης.

Πέρα από τα τυχαία σφάλματα, αξιολογούμε την επίδραση των συστηματικών σφαλμάτων στην απόδοση. Παρέχουμε μοντέλα για την επίδραση της τροποσφαιρικής καθυστέρησης διαδρομής στην εκτίμηση του συμβολομετρικού ύψους, για τα σφάλματα της γραμμής βάσης και ορίζουμε ένα μέγιστο σφάλμα φασικού συγχρονισμού που θα επέτρεπε την διάκριση του μετρημένου ύψος στις υπομεσαίες κλίμακες. Η συνεισφορά του σφάλματος συγχρονισμού στον προϋπολογισμού σφάλματος είναι $1\,\mathrm{cm}$, το οποίο μεταφράζεται σε φάση $0.045°$ στη ζώνη C. Εν τέλει, αναλύουμε μαθηματικά τη μεροληψία της κατάστασης θαλάσσης και δείχνουμε ότι η μεροληψία εξαρτάται από το ολοκλήρωμα του γινομένου της συνάρτησης μεταφοράς διαμόρφωσης και του φάσματος διακύμανσης επιφανειακού ύψους.

Οι προσομοιώσεις που βασίζονται στον προαναφερθέντα προϋπολογισμό σφαλμάτων δείχνουν ότι το Harmony, και άλλοι δορυφορικοί σχηματισμοί διστατικών ραντάρ με παρόμοιο σχεδιασμό, μπορούν να διακρίνουν την τοπογραφία σε υπομεσαία κλίμακα. Ωστόσο, πρόσφατες μελέτες δείχνουν ότι ο συγχρονισμός του Harmony που βασίζεται στο Παγκόσμιο Δορυφορικό Σύστημα Πλοήγησης (Global Navigation Satellite System GNSS) μειώνει το σφάλμα συγχρονισμού σε περίπου $1.6°$· άρα υπολείπεται ένα σφάλμα δύο τάξεις μεγέθους μεγαλύτερο απ' ό,τι θα έπρεπε βάσει του προϋπολογισμού. Έχουμε σχεδιάσει έναν αλγόριθμο συγχρονισμού που χρησιμοποιεί τα δεδομένα για να αφαιρέσει το υπολειπόμενο σφάλμα συγχρονισμού.

Ο αλγόριθμος χρησιμοποιεί την τεχνική multisquint και τη διαφορά της συμβολομετρικής φάσης περιοχών που δειγματοληπτούνται δύο φορές με μικρή χρονική υστέρηση, για να εκτιμήσει την παράγωγο του υπολοίπου και να ολοκληρώσει την παράγωγο και να εκτιμήσει το υπολειπόμενο σφάλμα. Ο αλγόριθμος επιτυγχάνει ένα αμερόληπτο μέσο τετραγωνικό σφάλμα $0.010°$, μειώνοντας το σφάλμα συγχρονισμού κάτω από το όριο του προϋπολογισμού σφάλματος.

Χρησιμοποιούμε τον άνεμο, τα ρεύματα, την τοπογραφία, το σημαντικό ύψος κύματος και το κυματικό φάσμα από μοντέλα ωκεανού-ατμόσφαιρας για τη ρεαλιστική προσομοίωση της εκτίμησης του RSSH. Οι προσομοιώσεις μας επιβεβαιώνουν ότι πριν από τη βαθμονόμηση βάσει δεδομένων το υπολειπόμενο σφάλμα συγχρονισμού κυριαρχεί στο σήμα, καθιστώντας τη διάκριση του RSSH δύσκολη, ενώ η διάκριση μετά την εφαρμογή του προτεινόμενου αλγόριθμου καθίσταται δυνατή και περιορίζεται μόνο από το θόρυβο του οργάνου.

Η διατριβή στο σύνολό της παρουσιάζει τον τρόπο σχεδιασμού, ανάλυσης, και εκτίμησης του σχετικού θαλάσσιου ύψους στις υπομεσαίες κλίμακες με τη χρήση διστατικού συμβολόμετρου SAR. Θέτει τις βάσεις για την πειραματική μέτρηση του OST από την αποστολή Harmony. Η προσθήκη αυτής της μέτρησης στην αποστολή θα προσέφερε τις πρώτες ταυτόχρονες μετρήσεις του πεδίου ανέμου, του πεδίου ρεύματος, του κυματικού φάσματος και του σχετικού ύψους της θαλάσσιας επιφάνειας σε υψηλή ανάλυση και με πλάτος $250\,\mathrm{km}$.

1

Introduction

Our planet is a dynamic system where a series of processes and feedback mechanisms regulate the transport of heat and nutrients. The processes occur at several spatial and temporal scales, and interact with one another due to their non-linear physics. Any picture of these processes would be wholly inadequate without the body of water that receives the majority of solar radiation and transports heat, carbon, and nutrients globally: the ocean. Currents are the primary mechanism through which the ocean transports these properties. Thus, understanding the ocean currents is of critical importance to understanding the ocean's role in the planet's uptake of heat and the exchange of heat, carbon, and nutrients with the atmosphere.

The vastness of the ocean makes in situ measurement of the global circulation on a regular basis impractical. It is for this reason that oceanographers have turned to remote sensing to study the ocean. Since the 1980s and the launch of Seasat, the data collected by remote sensing satellites, particularly radar nadir altimeters, have been instrumental in improving oceanographic knowledge [1]. Despite their contributions, limitations in the spatial footprint and the spatial sampling of nadir altimeters mean that the instruments do not resolve processes that occur below scales of $100\,\mathrm{km}$.

Without information on these smaller scales, we cannot form a complete picture of the role that currents play on the climate, on the lateral, and on the vertical transport of heat and nutrients in the ocean. At the same time, there has been growing interest in multistatic synthetic-aperture radar (SAR) in the form of companion satellites because of its flexibility and cost-effectiveness. This thesis explores the modeling, design, and calibration of multistatic SAR instruments and answers the question of how to design such an instrument to resolve ocean submesoscale currents.

1.1. Oceanic Submesoscale Currents

In the previous paragraphs we have talked about processes with spatial scales smaller than $100\,\mathrm{km}$. It is more apt to adopt the proper oceanographic terms for

the processes, the mesoscales, and the submesoscales. The oceanic submesoscale currents are flows in the form of fronts, wakes, and vortices at the surface and interior of the ocean. They have horizontal scales in the order of $0.1\,\mathrm{km}$ to $10\,\mathrm{km}$, vertical scales from $0.01\,\mathrm{km}$ to $1\,\mathrm{km}$, and temporal scales in the order of hours to days [2]. Their name alludes to their intermediate size between mesoscale currents and microscale turbulence.

There is growing evidence, through theoretical and numerical studies, that submesoscale currents play a critical role in the energy transfer, the mixing of heat and nutrients, and the sea state. Studies suggest that the submesoscales act as a conduit between the mesoscale eddies and the microscale turbulence, by breaking the geostrophic balance and forming an energy cascade to the dissipating microscales [2–4]. Submesoscale currents lead to the formation of fronts and vortices with large vertical velocities [5], transferring properties from the upper to the deep ocean [6]. Finally, SAR and altimeter observations confirm that submesoscale currents interact with waves, driving a significant part of their variability [7, 8].

1.2. Geostrophy: From Heights to Currents

You might be wondering why we have used currents and the need for their measurement as a motivation for ocean altimeters, which are instruments that measure surface height. The answer lies in a phenomenon known as *geostrophy*. We briefly introduce geostrophy in this section.

Over scales of tens of kilometers and away from the edges of the Ekman layer the flow of the ocean is horizontally and vertically balanced. Horizontally, the pressure gradient force due to currents, tides, and changes in barometric pressure balances the Coriolis force due to Earth's rotation. This balance is known as the geostrophic balance, or simply as geostrophy[9]. Vertically, the pressure gradient force balances the gravitational force. These two balances are approximately true for the major current systems of the globe, such as the Gulf Stream, the Kuroshio, and the Antarctic Circumpolar Current[10].

We will arrive at the geostrophic equations by starting from the Navier-Stokes momentum balance

$$\mathrm{D}_t\mathbf{v} = -\frac{1}{\rho}\nabla p - \nabla\Phi - 2\boldsymbol{\Omega}\times\mathbf{v} + \mathbf{F_f}, \tag{1.1}$$

where $\mathbf{v}$ is the parcel velocity, D_t represents the material derivative with respect to time, ρ is the density of the water, ∇f is the gradient of scalar field f, p is the pressure, Φ is the geopotential, $\boldsymbol{\Omega}$ is Earth's angular velocity, and $\mathbf{F_f}$ represents the friction force per unit mass. The geopotential is the sum of the true gravitational potential and the centrifugal potential. The term $2\boldsymbol{\Omega}\times\mathbf{v}$ is the Coriolis acceleration.

We assume that the flow is steady and that the non-linear terms and the friction terms are small compared to the pressure and gravitational terms. Then (1.1) becomes

$$2\boldsymbol{\Omega}\times\mathbf{v} = -\frac{1}{\rho}\nabla p - \nabla\Phi. \tag{1.2}$$

Writing the horizontal and vertical components separately gives

$$\partial_x p = \rho f v, \tag{1.3}$$
$$\partial_y p = -\rho f u, \tag{1.4}$$
$$\partial_z p = -\rho g, \tag{1.5}$$

where in (1.3), and (1.4) $f = 2\Omega \sin\varphi$ is the Coriolis parameter with φ representing the latitude. In (1.5) we have assumed that the vertical coordinate is small compared to the distance to the Earth's center of mass to approximate the geopotential as $\Phi = \Phi_0 + gz$[9]. Equation (1.5) gives the well-known expression of hydrostatic balance, while (1.3), and (1.4), are the geostrophic equations.

The geostrophic and hydrostatic relations tell us that the horizontal pressure gradients determine the horizontal flow of the ocean. If we define $z = 0$ to be the surface of the geoid, $-h$ to be a level surface at a shallow depth below the geoid and ζ to be the height of the sea surface, then integrating (1.5) gives the pressure at the shallow depth

$$p = p_0 + \int_{-h}^{\zeta} \rho(z) g(\varphi, z)\, \mathrm{d}z, \tag{1.6}$$

where p_0 is the atmospheric pressure at the geoid. Assuming a vertically homogeneous ocean over the small shallow layer between the sea surface and depth $-h$, and assuming that the changes in the gravitational acceleration within the shallow layer are negligible allows us to take ρ and g out of the integral in (1.6). Substituting into (1.3) and (1.4) gives

$$v = \frac{g}{f}\, \partial_x \zeta, \tag{1.7}$$
$$u = -\frac{g}{f}\, \partial_y \zeta. \tag{1.8}$$

Equations (1.7), and (1.8) relate the horizontal components of the velocity to the horizontal derivatives of the topography ζ. This property of geostrophic currents allows us to estimate the mean currents from satellite altimeter measurements of the ocean topography.

1.2.1. Note on Terminology

In this thesis we investigate the retrieval of ocean topography from SAR data with a technique called cross-track interferometry. There are several terms of art relating to the topography of the ocean. To help the reader disambiguate between them, we explain the terms most relevant to this thesis and illustrate them in Figure 1.2.1.

- The geoid is the level surface that the ocean would form if it was at rest.
- The reference ellipsoid is a smooth approximation of the geoid, and it is used to define Earth-based coordinate systems.
- The sea-surface height (SSH) is the distance between the sea surface and the reference ellipsoid.

1

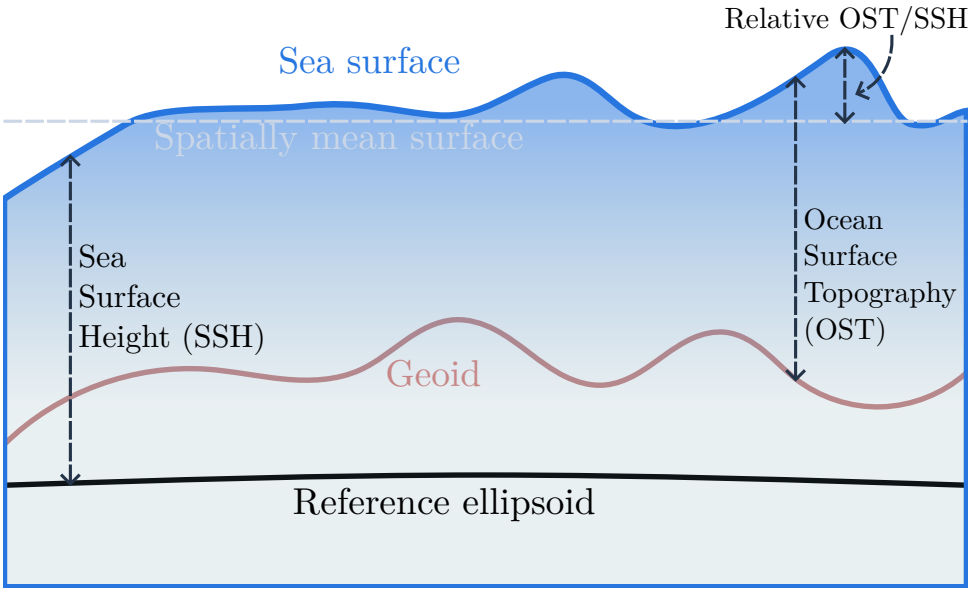

Figure 1.1.: Ocean topography terms that are relevant to this thesis.

- The ocean surface topography (OST) is also a measurement of the surface height, but with respect to the geoid instead of the reference ellipsoid.
- The spatially mean surface is the mean of the sea surface at a given instant of time.
- The relative OST or relative SSH (RSSH) is the height of the surface above the level of the spatially mean surface.
- The sea-surface height anomaly (SSHA) is the surface height relative to a temporal mean of the SSH.

A cross-track interferometer senses variations in the surface height as changes in the phase of the interferometric signal from $-\pi$ rad to π rad. Thus, the interferometer is sensitive to the relative height with respect to the mean height of the surface being imaged. In this thesis, we call this quantity relative SSH or relative OST. It should not be confused with SSHA, which is the height relative to the temporal mean of the surface not the instantaneous spatial mean.

1.3. Tropical and Extratropical Cyclones

Tropical (TC) and extratropical cyclones (ETC) have a large impact on the ocean and the atmosphere, and thus are an important part of understanding climate change. They also have a significant societal impact, as they are one of the deadliest weather phenomena. Tropical and extratropical cyclones produce a series of dangerous weather events such as extreme winds, high sea states, storm surges, and intense rainfall. Accurate modeling and forecasting of these cyclones are important for both climate science and society.

TCs and ETCs draw most of their energy from the ocean in the form of heat, and they interact with the atmosphere and the ocean through a series of feedback mechanisms. Wind variations over the ocean drive waves, which exchange energy with cyclones. Strong winds enhance the transport of heat from the ocean, while at the same time increasing the vertical transfer of heat in the ocean, lowering the sea surface temperature and reducing the flow of heat to the cyclone. ETCs can also be the focal point of wave energy from which swell waves originate [11]. These processes are not included in models or forecasts due to a lack of parametrization.

As cyclones move over the ocean, they leave behind them a wake, either in the form of a plume or of inertial waves. The waves have strong, persistent signatures that can be observed through several physical parameters. The strongest anomalies are seen in temperature, and height and persist after the cyclone has passed [12]. TCs interact with the sea surface temperature through heat transport to the atmosphere, vertical mixing, and Ekman upwelling [13]. The strong variations of wind that cyclones induce form cold wakes, which present as anomalies in the sea surface temperature with values up to $10\,^{\circ}\mathrm{C}$ [14]. The strong pressure variations within the cyclone cause vertical displacements, which manifest as sea surface height anomalies. SSHAs can reach up to $30\,\mathrm{cm}$ to $50\,\mathrm{cm}$ [15, 16]. These temperature and height phenomena play a role in the intensification of the cyclone [13].

The interaction of cyclones with several geophysical properties of the ocean at kilometer scale highlights the beneficial potential of high-resolution wide-swath co-located observations of surface roughness, stress-equivalent wind, currents, directional wave spectra, and relative SSH that a SAR can offer. Specifically, C-band radar has less rain attenuation than higher-frequency radars or scatterometers, allowing it to receive scattering from within the eye of the cyclone. Currently, no remote sensing instrument is capable of observing these geophysical parameters within the inner core of cyclones. Sentinel-1 data offers an opportunity to study TC and ETC cases in terms of surface roughness, stress-equivalent wind speed, and wave spectra [16]. However, the instrument is limited to a single line of sight, precluding the retrieval of topography and of the asymmetric components of the aforementioned parameters.

1.4. Harmony

Harmony is the European Space Agency's tenth Earth Explorer. Earth Explorers are breakthrough research missions proposed by the scientific community, and

1

focused on delivering findings to improve the scientific understanding of our planet. Harmony is a multi-domain mission that will provide measurements of surface motion over land, ice, and the ocean.

The mission consists of two satellites, called companions, orbiting in convoy with a Copernicus Sentinel-1 synthetic-aperture radar (SAR) satellite. Each companion has two instruments: a passive SAR, which uses Sentinel-1's radar as an illuminator, and a multi-view Thermal Infra-red (TIR) instrument. Since the SARs of the companions use Sentinel-1's radar as the illuminator, they are bistatic radars.

The convoy will alternate between two different phases during the lifetime of the mission. In the stereo phase, the convoy will share the orbital plane with Sentinel-1. One companion will lead, while the other will lag Sentinel-1 with each of them having a mean separation of $350\,\mathrm{km}$ from Sentinel-1. In this phase, Harmony will use the different lines of sight of the companions to estimate velocity vectors of the surface. Over the oceans, this translates to kilometer-scale estimates of the instantaneous surface current velocity, stress-equivalent wind velocity, and directional wave spectra. Harmony will be the first mission to provide simultaneous estimates of these parameters at kilometer scale.

The second phase is known as the cross-track interferometry (XTI) phase. In this configuration, the companions fly in a close formation $350\,\mathrm{km}$ behind Sentinel-1. The formation is designed for cross-track interferometry, a technique that combines two SAR images of the same scene taken from different positions to estimate the surface height. The objectives of the XTI phase are to produce estimates of three-dimensional land deformation, and surface elevation time series of glaciers, icebergs, and volcanoes.

The mission has no ocean-related objectives in the XTI phase. The reason is that single-pass XTI of the ocean surface with a multisatellite bistatic system has numerous challenges. The concept of using interferometry to estimate ocean topography has been proposed by Rodríguez et al. as Wide-swath Ocean Altimetry (WSOA)[17]. The concept employs two side-looking SARs, placed on a single satellite with a cross-track separation, to interferometrically estimate the relative surface heights over a swath of tens of kilometers together with a nadir altimeter that provides absolute estimates of the surface topography. WSOA solves the sampling limitations of nadir altimeters that render them unable to resolve oceanic processes with wavelengths below $100\,\mathrm{km}$. On the 16th of December 2022, NASA and CNES launched the Surface Water and Ocean Topography mission that is the evolution of the WSOA concept.

Bringing the WSOA concept to Harmony would provide two years of additional data of ocean surface topography at the submesoscales. Furthermore, the height estimates from Harmony complement the data from SWOT nicely, as an interferometer with a medium- to far-range incidence angle, as is the case with Harmony, will receive a signal with a high normalized radar cross-section (NRCS) at medium to high winds, while an almost nadir-looking interferometer will receive a signal with declining NRCS as the wind increases due to the dominant scattering mechanisms being Bragg and specular at these incidence angles, respectively. Importantly, the synergy of a potential RSSH product with the other ocean-related

Harmony products will provide an unprecedented opportunity to study submesoscale eddies, fronts, cyclones, and internal waves.

In the XTI phase, Harmony loses one of its two views because one of the companions moves from being symmetrically displaced from Sentinel-1 to a close formation with the second companion. However, the system will maintain two views (Sentinel-1 and the companions), making retrieval of two-dimensional stress-equivalent wind vectors, and surface currents possible, albeit with degraded performance. Directional wave spectra retrieval also remains viable. Thus, the addition of RSSH to the capabilities of Harmony will provide the first set of high-resolution, wide-swath estimates of stress-equivalent wind vectors, surface current vectors, directional wave spectra, and RSSH. This will be unique, particularly in the case of TCs and ETCs, as it will allow scientists to study at least one projection of the inertial motion that the cyclone injects into the ocean, as well as the vertical displacement of the surface, and the low-pressure surge. Due to the persistence of the cold wake after the cyclone's passing, the sea-surface temperature of the cold wake might be visible at a later acquisition through Harmony's TIR instrument.

However, designing a multi-satellite bistatic interferometer is, as explained in the following chapters, challenging. The work in this thesis aims to answer the question of how to model and design a bistatic wide-swath ocean altimeter, how to overcome the challenge of sensing a dynamic decorrelating surface, and how to calibrate the data to retrieve ocean surface topography. The ultimate aim is to introduce an experimental ocean surface topography product for Harmony.

1.5. Research Objectives

This thesis focuses on the following objective at the intersection of remote sensing and oceanography: estimating submesoscale ocean surface topography with bistatic SAR interferometry. The objective is multifaceted and touches several topics. Firstly, to determine if we can achieve it, we need to accurately model the performance of an interferometer estimating the ocean topography. Accurate modeling requires studying the stochastic processes governing the surface and its relationship with the scattered electromagnetic signal. Secondly, the performance depends on parameters such as the sensitivity to height and the temporal lag which do not have models for cases with highly squinted beams, as is the case for Harmony. Finally, one of the big challenges with bistatic systems is phase synchronization. Thus, any interferometer that aims to estimate small signals such as ocean topography needs a calibration algorithm to remove dominant time- varying systematic errors such as phase synchronization residuals. The research presented in the next chapters aims to answer the following questions:

Question 1. *What is the expected accuracy of interferometric estimates of ocean surface topography obtained from a bistatic system?*

To answer the question, we need to identify the sources of error, random and systematic, and model their effect on the interferometric estimate. One of the

primary sources of error in interferometric estimates of the ocean topography is temporal decorrelation. Temporal decorrelation occurs when the two SAR images that form the interferogram lose coherence because of changes in the scene during the time that elapses between their acquisition. Formation-flying systems have a tangential separation that varies along the orbit. Such systems have a lower bound on the tangential separation that safe satellite operations permit. The lower bound is larger than the coherence time of the ocean surface. Thus, retrieving ocean surface topography from a formation-flying interferometer is challenging.

The accuracy of the interferometric estimate in terms of standard deviation does not tell us the spatial scales that the instrument will resolve. In an oceanographic context, spatial resolution is defined in terms of the wavelength. Thus, to assess the spatial resolution, we determine the spectral envelope of the instrument and compare it against the power spectral density (PSD) of the ocean surface topography.

Question 2. *What is the sensitivity of an interferometer with a significantly squinted beam?*

The performance of an interferometer depends, particularly in cases where the geophysical signal is small such as ocean surface topography, on the sensitivity to height and motion. Mathematical formulations of the sensitivity assume a monochromatic signal and planar zero-Doppler viewing geometry. Assumptions that break down in forward- or backward-looking systems. Therefore, to assess the performance of an interferometer with a squinted beam, we require a new model for interferometric sensitivity.

Question 3. *To what degree can we correct the data to reduce the phase-synchronization error with a data-driven algorithm?*

In answering the first research question, we developed an error budget for the OST estimate of a formation-flying interferometer. The error budget shows that for a bistatic system, the phase synchronization error dominates the error budget. Specifically, in the case of Harmony, the error, if left unmitigated, will render OST retrieval impossible. Furthermore, it will impact core mission products. The Harmony engineers have designed a GNSS-based synchronization scheme to mitigate the error. Initial studies suggest that the suppression achieved by this scheme is not enough to allow retrieval of OST. Thus, we need to suppress the residual that remains after synchronizing the phases of the Harmony radars with the GNSS-based scheme further. Our approach is to use information included in the data to do so.

1.6. Outline

In Chapter 2, we introduce a measurement concept for the retrieval of OST with a multisatellite interferometer. We investigate two different systems: one with the design of Harmony, featuring a separate illuminator and two bistatic companions, and a quasi-monostatic system with one satellite acting as both transmitter

and receiver, and a bistatic companion. We optimize the formation to leverage the squint to reduce the effective temporal lag sufficiently to avoid complete temporal decorrelation of the received signals. By identifying and characterizing the sources of random error, we build a model for the standard deviation of the OST estimate. We then convert the noise floor to a spectral envelope and intercept it with different models of the PSD of the sea surface height to assess the spatial resolution of the instrument. Furthermore, we analyze the main sources of systematic errors and mathematically analyze in-depth the sea-state bias of the estimate.

Chapter 3 studies the fundamental relation between viewing geometry, and interferometric sensitivity and spectral shift. Instead of using a geometric approximation, as is commonly done in the literature, we use the Fourier Diffraction Slice Theorem to derive the sensitivity from the region of support of the signals in the Fourier domain. The analytical form of the sensitivity that we derive is valid for both planar configurations, and configurations with widely squinted beams. Furthermore, it works for monostatic, and multistatic systems. Thus, Chapter 3 answers the second research question.

In Chapter 4 we set out to answer the third research question. We present an algorithm that estimates the first order time derivative of the post-GNSS synchronization residual, and then integrates it to estimate the residual. The algorithm estimates the derivative by combining two techniques: multisquint processing, which divides SAR images into subapertures and forms the differential interferograms between the subapertures, computing the differential interferogram of certain regions in the SAR images that are acquired twice with a small lag between the two acquisitions due to the sensing timeline of the instrument.

We evaluate the algorithm by simulating the interferometric acquisitions of Harmony over an oceanic scene. We start from a scene described by ocean topography, wind, currents, and a directional wave spectrum, obtained from the MARC dataset. Then, we feed these geophysical parameters into the performance model that we created to answer the first research question. Simultaneously, we use the method developed in answering the second research question to compute the sensitivity and temporal lag of Harmony's XTI formation at the scene. Additionally, we simulate the phase synchronization residual that the measurement will have after the GNSS-based correction. Finally, we produce simulated interferograms with the random errors coming from the performance model, and the phase synchronization residual. We run the algorithm on the simulated data, and assess its performance.

Lastly, Chapter 5 lists the conclusions and succinctly answers the research questions. Furthermore, we acknowledge the limitations of the work in this thesis, and recommended improvements for the future.

2

Wide-Swath Ocean Altimetry Using Multisatellite Single-Pass Interferometry

Prologue

This chapter is an updated version of [18].

The results in the publication were based on a geometric method of calculating the interferometric sensitivity and the temporal lag. The method uses the expressions of sensitivity, and temporal lag of a monostatic system, and adjusts them to work for a bistatic system with a squinted line of sight. At the time of writing the article, this method was in line with the state of the art. Nevertheless, we were aware that the method begins to lose its validity as the squint becomes significant. Thus, we investigated a new method that would not assume a monostatic system, or a zero-squint line of sight. We explain the new method in depth in Chapter 3.

Our findings showed that the differences in the two methods are significant. Thus, we have adapted this chapter from the publication by re-calculating the results using the spectral method of Chapter 3.

[18] A. Theodosiou, M. Kleinherenbrink and P. López-Dekker. 'Wide-Swath Ocean Altimetry Using Multisatellite Single-Pass Interferometry'. In: *IEEE Transactions on Geoscience and Remote Sensing* 61 (2023), pp. 1–21

Estimating sea surface height using cross-track interferometry requires high sensitivity because the ocean surface signal is in the order of $10\,\mathrm{cm}$. *Additionally, the interferometer requires a temporal delay of a few milliseconds to ensure coherency of the moving ocean surface. We show that a squinted line of sight, in combina-*

tion with a Helix satellite formation allows optimizing the effective perpendicular and along-track baselines to satisfy these conditions. This chapter presents a model to estimate the performance of a formation-flying cross-track interferometer with a squinted line of sight. The tenth Earth Explorer, Harmony, which features two bistatic SAR companions, and a theoretical system with one monostatic and one bistatic SAR are used as case studies. The standard deviation of the height estimate is $1\,\mathrm{cm}$ *to* $8\,\mathrm{cm}$ *from the near to the far range respectively, at a wind speed of* $5\,\mathrm{m\,s^{-1}}$ *over an orbit except towards the polar latitudes. The power spectral density of the elevation shows that spatial scales of approximately* $39\,\mathrm{km}$ *to* $26\,\mathrm{km}$ *can be resolved, depending on the elevation spectrum. The performance improves at higher wind speeds due to higher backscattering. At a wind speed of* $15\,\mathrm{m\,s^{-1}}$*, wavelengths of approximately* $23\,\mathrm{km}$ *to* $8\,\mathrm{km}$ *can be resolved. The performance over a* $250\,\mathrm{km}$ *swath enables the instantaneous estimation of the surface elevation at the submesoscales for the first time.*

2.1. Introduction

Satellite remote sensing instruments have significantly contributed to our understanding of ocean dynamics. Estimates of the sea surface height (SSH) made by radar altimeters have advanced oceanographic knowledge. Despite the plethora of SSH data that has been made available in the past decades by remote sensing instruments, ocean processes that occur at scales of $10\,\mathrm{km}$ to $100\,\mathrm{km}$, the so- called *submesoscales*, are not captured in the present data. Submesoscale ocean motion plays an important role in the vertical transport of heat and nutrients [6], and the observational gap of capturing these scales has been identified [19].

Cross-track interferometry (XTI) is a technique that combines two complex-valued SAR images of the same surface, taken from different sensor positions, to estimate the relative surface height. Typical SAR instruments have swath widths in the range of $30\,\mathrm{km}$ to $250\,\mathrm{km}$ with geometric resolutions of meters up to tens of meters. Thus, an interferometric height estimate, computed at sufficiently high resolution (depending on the amount of averaging), could provide relative SSH estimates with sufficient sampling to resolve submesoscale ($10\,\mathrm{km}$ to $100\,\mathrm{km}$) phenomena such as eddies, currents, tides, and wakes from tropical cyclones.

Two properties of a cross-track interferometer that determine its performance are the perpendicular and along-track baselines. Firstly, the perpendicular baseline, defined as the distance perpendicular to the line of sight (LoS) between the two sensor positions, is directly proportional to the height sensitivity. However, the maximum useful perpendicular baseline is constrained by decorrelation and the height of ambiguity. Secondly, the along-track baseline is the distance corresponding to the temporal lag between acquisitions of a given resolution cell on the imaged surface. If the surface changes during the temporal lag, the signals of the two acquisitions become decorrelated. The decorrelation manifests as noise in the interferogram and its degree depends on the rate of change of the surface. Therefore, topographic mapping of dynamic surfaces, such as the ocean, requires

minimizing the along-track baseline while keeping a sufficient perpendicular baseline for sensitivity.

The requirement of a minimum along-track baseline precludes repeat-pass interferometry as a possible technique of estimating SSH. Single-pass interferometry can satisfy the requirement in the form of a single-platform interferometer or a formation-flying system of two SAR satellites. Single-platform cross-track interferometers, such as the Wide-swath Ocean Altimetry (WSOA) concept [17], overcome the issue by mechanically fixing the two SAR antennas on the satellite to physically eliminate their along-track separation. Thus, due to structural and manufacturing limitations, the two SAR antennas cannot be further apart than several meters. This limit on the cross-track separation between the antennas puts, for a given power budget, an upper bound on the sensitivity. Therefore, single-platform interferometers trade geometric sensitivity for temporal coherence.

A formation-flying interferometer achieves, given appropriate formation parameters, larger interferometric baselines between the sensors. Specifically, the Helix formation [20] allows optimizing the along-track and perpendicular separation of the satellites as a function of latitude. The formation can be configured so that the radial separation results in an along-track separation that tends to a minimum at polar latitudes and a maximum at mid-latitudes. Nevertheless, safe proximity operation constrains the minimum along-track separation above $100\,\mathrm{m}$. For an interferometer with lines of sight perpendicular to the along-track direction, which causes the along-track baseline to equal the along-track separation, this is too large for coherent acquisitions of the ocean surface.

In this chapter we propose an alternative: introducing a squinted line of sight to decrease the effective along-track baseline of a helix interferometer to allow estimation of relative sea-surface heights while keeping a safe radial separation. Optimizing the formation parameters allows for acquisitions with perpendicular baselines of hundreds of meters and effective along-track baselines of meters. Therefore, sensitivity is maintained while temporal decorrelation is minimized. The result is estimates of SSH with an accuracy in the order of $10\,\mathrm{cm}$ over wide swaths, enabling the recovery of mesoscale and submesoscale processes of the ocean surface in a single pass.

This chapter is structured as follows: Section 2.2 explains the measurement concept, the bistatic geometry and formation, and the performance model. In Section 2.3 we discuss the performance of two interferometers: Harmony, the tenth Earth Explorer [21], and a hypothetical quasi-monostatic system of two SARs without a separate illuminator. Section 2.4 identifies the main sources of systematic errors and outlines an estimate of their impact. Finally, Section 2.5 introduces the oceanic and atmospheric biases, with a mathematical derivation of the sea-state bias in appendix A, and their effect on the relative height estimate.

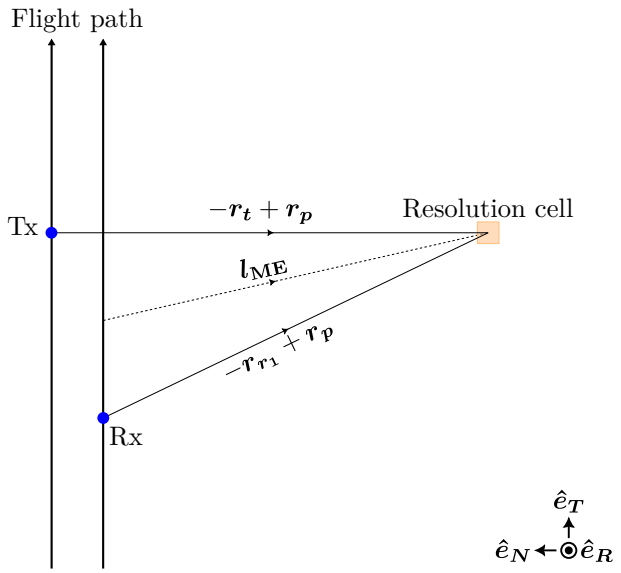

Figure 2.1.: Top view of the line of sight of the monostatic equivalent. $\mathbf{r_t}$, $\mathbf{r_{r_1}}$, and $\mathbf{r_p}$ represent the position vectors of the transmitter, the first receiver, and the resolution cell on the surface. The line of sight of the monostatic equivalent is parallel to the angle bisector, $\mathbf{l_{ME}}$, of the transmitter and receiver lines of sight.

2.2. Measurement Concept and Related Work

2.2.1. Interferometric SAR Geometry

The purpose of this chapter is to present a performance model for single-pass cross-track SAR interferometry over the oceans. One of the key findings that will be discussed in the subsequent sections is that a squinted line of sight, in contrast to the conventional zero-Doppler line of sight, combined with a Helix formation enables coherent acquisitions of the ocean surface. In the performance analysis, we model the formation geometry using two monostatic equivalent SARs with squinted lines of sight. The equivalent systems can represent monostatic sensors or a bistatic system. The definition of the monostatic equivalent, the relative motion of two spacecraft in close formation, and the effective along-track and perpendicular baselines, quantities that are relevant to the interferometric performance, are discussed in the following subsections.

Bistatic SAR and Monostatic Equivalent

The geometry of a bistatic system forms an important link with performance through the interferometric baselines. The different transmitter-to-target and target-to-receiver paths of a bistatic SAR complicate the calculation of the interferometric

baseline, particularly in the case of two receivers where there is a pair of surface-to-receiver paths. The complication due to the asymmetry of the bistatic range is well known in SAR processing, where an analytic formulation of the 2-D point-target spectrum does not exist for this reason. A workaround is to locate the position where a monostatic radar would measure approximately the same signal as the bistatic system. This concept is known as the monostatic equivalent in the literature [22], and has been used to process bistatic SAR data with monostatic focusing algorithms.

Geometrically, an equivalent system reduces an illuminator and receiver pair to a single monostatic SAR. In the case of two bistatic receivers, the illuminator and the two companions are transformed to two equivalent monostatic SARs. The interferometric baseline becomes the distance between the points where the two monostatic equivalents observe a given point on the ground with the same geometry.

The monostatic equivalent of each bistatic system lies along the bisector of the bistatic angle formed by the illuminator-to-surface and the surface-to-receiver range and has a line of sight parallel to:

$$\mathbf{l_{ME}} = \frac{-\mathbf{r_t} + \mathbf{r_p}}{\|-\mathbf{r_t} + \mathbf{r_p}\|} + \frac{-\mathbf{r_{r_i}} + \mathbf{r_p}}{\|-\mathbf{r_{r_i}} + \mathbf{r_p}\|}, \tag{2.1}$$

where $\mathbf{r_t}$ is the position vector of the transmitter, $\mathbf{r_p}$ the position vector of the point scatterer on the illuminated surface, and $\mathbf{r_{r_i}}$ the position vector of the ith receiver where $i \in \{1, 2\}$. Figure 2.1 shows a visual representation of (2.1).

Relative Motion

Flying the SAR satellites in a Helix formation allows optimizing the along- and cross-track separation for cross-track interferometry. The formation-flying elements discussed in this section apply equally to a monostatic and a bistatic SAR. In the case of Harmony, the mission consists of two passive companion satellites, which we refer to as Concordia and Discordia, flying in close formation with Sentinel-1 (S1) as the illuminator. In the XTI mission phase, Concordia and Discordia will fly behind S1, in a Helix formation [23] with a configurable along and cross-track separation, as shown in Figure 2.2. We employ the relative inclination and eccentricity vector formulation of relative motion [20] to model the effect of the formation on interferometric performance.

The orbital frame of reference is used as the basis for all calculations. It consists of three unit vectors moving together: $\hat{\mathbf{e}}_\mathbf{R}$ along the radial direction (positive away from the Earth's center), $\hat{\mathbf{e}}_\mathbf{T}$ in the along-track (tangential) direction of the satellite motion, and the unit vector $\hat{\mathbf{e}}_\mathbf{N}$ normal to the orbital plane in the direction of the positive angular momentum vector (cross track). This triad denotes a right-handed system, with two time-dependent vectors $\hat{\mathbf{e}}_\mathbf{R}$ and $\hat{\mathbf{e}}_\mathbf{T}$; $\hat{\mathbf{e}}_\mathbf{N}$ is time invariant under the Keplerian approximation [20].

The relative motion of the second satellite (deputy), indicated by C in Figure 2.3, with respect to the first (main), indicated by M, is expressed in the orbital frame

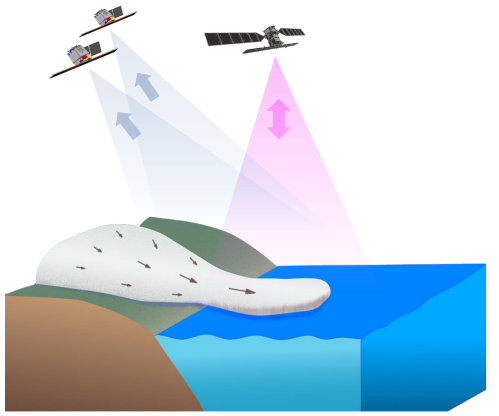

Figure 2.2.: The Harmony XTI configuration. The two companions, Concordia and Discordia, fly in close formation behind Sentinel-1D.

centered on the main satellite

$$\begin{aligned}\Delta\mathbf{r} &= \mathbf{r_2} - \mathbf{r_1} \\ &= \Delta r_R \hat{\mathbf{e}}_\mathbf{R} + \Delta r_T \hat{\mathbf{e}}_\mathbf{T} + \Delta r_N \hat{\mathbf{e}}_\mathbf{N},\end{aligned} \tag{2.2}$$

where $\mathbf{r_j}$ for $j = \{1,2\}$ is the position vector of the main and deputy satellites respectively and $\Delta r_R, \Delta r_T, \Delta r_N$ are the distances between the two satellites along the directions corresponding to each unit vector.

For near-circular orbits in close formation, which is the case for the orbits discussed in this chapter, we linearize the motion according to [20]. Thus, the components of the relative position vector Δr are

$$\begin{bmatrix}\Delta r_R/a \\ \Delta r_T/a \\ \Delta r_N/a\end{bmatrix} = \begin{bmatrix}\Delta a/a & 0 & -\Delta e_X & -\Delta e_Y \\ \Delta u & -3\Delta a/(2a) & -2\Delta e_Y & +2\Delta e_X \\ 0 & 0 & -\Delta i_Y & +\Delta i_X\end{bmatrix} \times \begin{bmatrix}1 \\ u - u_0 \\ \cos u \\ \sin u\end{bmatrix}, \tag{2.3}$$

where a is the semi-major axis of the orbit, $\Delta\mathbf{e}$ and $\Delta\mathbf{i}$ are the differences between the eccentricity and inclination vectors, respectively; the subscripts X, Y represent the first and second components of the vector, u is the mean argument of latitude, and $u - u_0$ is the argument at reference epoch t_0.

Setting $\Delta e_X = 0$ and $\Delta i_X = 0$ and the second component of the relative eccentricity and inclination vectors to a non-zero value provides passive stability to the formation because the two orbits are spatially separated. The two orbits pass over one another near the poles, when $u = \pi/2$, where the normal separation goes to 0 but the radial separation tends to its maximum. The opposite occurs near the equator, where the radial component goes to 0 and the normal is maximized. The oscillation of Δr_R and Δr_N with a phase difference of $\pi/2$ forms the known helix-like formation introduced in [20]. For the purposes of relative topography estimation, constant orbital anomaly and semi-major axis offsets are counterproductive,

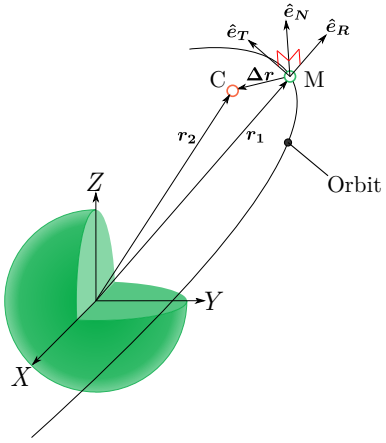

Figure 2.3.: Orbital frame of reference for the relative motion between two satellites.

hence Δu and Δa are set to 0. Thus, the relative position vector of the formation is determined by Δe_Y and Δi_Y. The latter is approximated by

$$\Delta i_Y \approx \Delta\Omega \sin i, \tag{2.4}$$

where i is the inclination of the orbit and $\Delta\Omega$ is the difference in the right ascension of the ascending node of the two spacecraft.

Along-Track Baseline

A time interval between the two SAR acquisitions forming an interferogram produces a phase difference directly proportional to the velocity of the imaged surface [24]. We refer to the distance traveled in the flight direction during this time interval as the along-track (interferometric) baseline. In a conventional interferometer where both images are acquired by monostatic instruments looking along the zero-Doppler plane, the along-track baseline equals the along-track separation. For a cross-track interferometer, an along-track baseline reduces the accuracy of the height estimate because a part of the interferometric phase comes from the velocity of the surface rather than the topography.

Figure 2.4 illustrates the top-view geometry of two SAR satellites separated in the along and cross-track directions. The lines of sight of the two SAR antennas are looking forward with respect to the zero-Doppler direction. We give the term "squint" to the angle between the lines of sight and the zero-Doppler plane. The ground-projected squint of the antenna is labeled η. In this projection the antenna look angle is not visible as it is directed into the page.

The figure shows that for a zero Doppler configuration ($\eta = 0°$) the along-track baseline is equal to the physical separation of the two satellites in the tangential direction. If η is non-zero, the baseline that arises due to the temporal lag is no

longer the same as the physical separation. The squinted line of sight and the normal separation Δr_N cause the second satellite to observe the same point as M, e.g. resolution cell P in the diagram, before it moves Δr_T along $\hat{\mathbf{e}}_T$. The effective baseline becomes

$$B_{\parallel} = \Delta r_T - \Delta r_N \tan\eta. \tag{2.5}$$

Equation (2.5) shows that setting $\tan\eta = \Delta r_T/\Delta r_N$ gives a zero effective along-track baseline. According to (2.3), the two components of interest depend on the following formation parameters $\Delta u, \Delta a, \Delta\mathbf{e}, \Delta\mathbf{i}$. For a stable formation, the dependence reduces to Δe_Y and $\Delta\Omega\sin i$. Substituting (2.3) into (2.5) and setting the baseline to zero yields the condition that the ratio $\Delta e_Y/\Delta\Omega$ must meet:

$$\frac{\Delta e_Y}{\Delta\Omega} = \frac{\sin i}{2}\tan\eta. \tag{2.6}$$

Figure 2.5 shows the along-track physical separation and the effective along-track baseline at the near range for a set of formation parameters that have been optimized according to (2.6). We note that while the separation reaches $230\,\mathrm{m}$ the effective baseline has a maximum magnitude of $38\,\mathrm{m}$. The variation of the effective along-track baseline follows this sinusoidal pattern for all incidence angles with decreasing amplitude towards the middle range and increasing amplitude from the middle to the far range. The effective baseline does not exceed $80\,\mathrm{m}$ for this set of formation parameters.

Perpendicular Baseline

To discuss the calculation of the perpendicular baseline we start from a non-squinted configuration where the two SAR sensors are in the same radial-normal plane. We consider the projection along the radial-normal plane as illustrated in Figure 2.6. The perpendicular baseline $B_\perp$ is the distance between the two planes spanned by the flight direction (along-track) and the line of sight (antenna beam-pointing direction) of each satellite:

$$\begin{aligned} B_\perp &= b_{X_1} + b_{X_2}, \\ &= \Delta r_N\cos\theta + \Delta r_R\sin\theta. \end{aligned} \tag{2.7}$$

Introducing a squint to the line of sight changes the effective perpendicular baseline, as was the case for the along-track baseline. Figure 2.7 illustrates such a configuration. To find the effective baseline, the line of sight and the co-registration need to be taken into account. As discussed in Section 2.2.1, after co-registration of the two SAR images, the along-track separation of the two sensors becomes $\Delta r_N\tan\eta$. This is equivalent to rolling forwards the position of the deputy satellite along its orbital path so that it shares the same radial-line-of-sight plane as the main satellite.

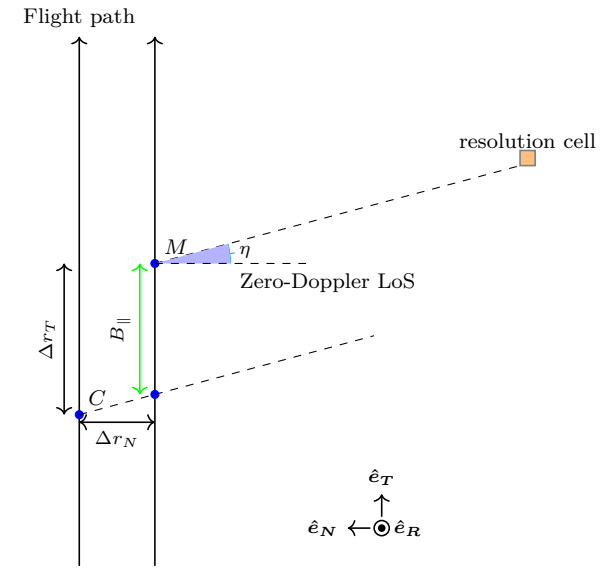

Figure 2.4.: Top view of the formation with a squinted line of sight. M represents the position of the main and C of the deputy.

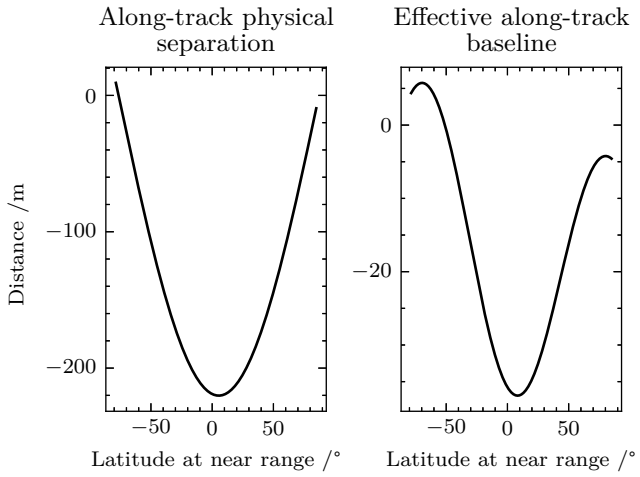

Figure 2.5.: The left panel shows the along-track physical separation of a formation with parameters $a\Delta e = 117\,\mathrm{m}$ and $a\Delta\Omega = 650\,\mathrm{m}$ and the right panel shows the effective along-track baseline for the same formation.

At the point where the two satellites view the same resolution cell their separa-

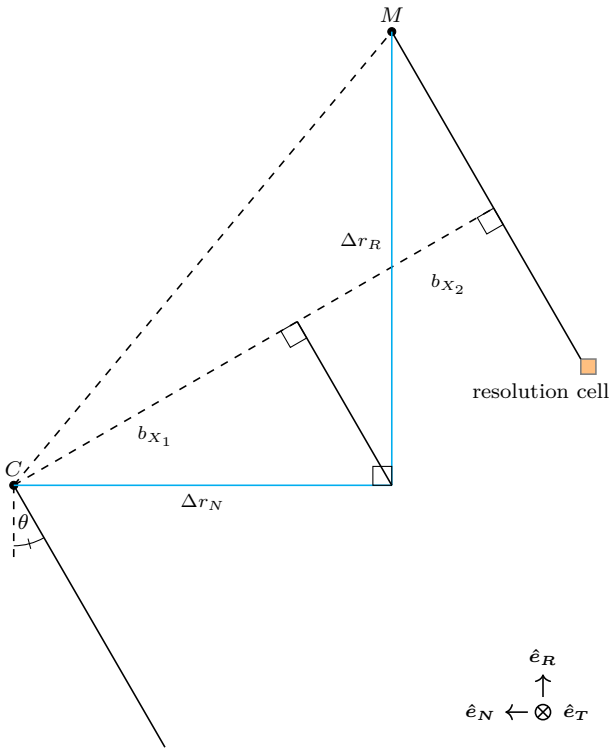

Figure 2.6.: View along the radial-normal plane. The squint angle in this view would be into/out of the page. The look angle θ is the angle formed by the direction of the beam center and the nadir.

tion is given by

$$\mathbf{b_{3D}} = \begin{pmatrix} \Delta r_R \\ \Delta r_N \tan\eta \\ \Delta r_N \end{pmatrix}, \tag{2.8}$$

where $\tan\eta$ is the tangent of the ground-projected squint. $\tan\eta$ is also given by the ratio of the along-track component to the normal component of the unit vector parallel to the line of sight $\hat{\mathbf{l}}$. The perpendicular baseline is given by

$$\begin{aligned} B_\perp &= \|\mathbf{b_{3D}}\| \sin\psi, \\ &= \|\mathbf{b_{3D}} \times \hat{\mathbf{l}}\|, \end{aligned} \tag{2.9}$$

where ψ is the angle between $\mathbf{b_{3D}}$ and $\hat{\mathbf{l}}$. Equation (2.9) shows that the physical separation components and the ground-projected squint can be tuned to give a $B_\perp$ that is sufficiently large to offer good sensitivity to height. At the same time,

Δr_T does not affect $B_\perp$, thus it can be selected together with angle η to minimize $B_\parallel$ according to (2.5). Equation (2.9) shows that the effective perpendicular baseline is the projection of the physical separation perpendicular to the line of sight, after aligning the lines of sight of the two receivers. Therefore, it largely follows the perpendicular baseline of the formation, which varies sinusoidally with the mean argument of latitude with a maximum around $0°$ and minima towards the poles where the two satellites cross each other. Due to the squint the amplitude of the sinusoidal variation decreases slightly with incidence angle.

2.2.2. Cross-track Interferometry Model

In monostatic systems, the two-way range difference between the two instruments and the surface can directly be coupled to surface elevation. For single-transmitter systems, such as a single-pass interferometer where only one SAR transmits, the same is true except that it depends solely on the single-way range difference. The interferometric phase between two images of the same scene obtained from two SARs is

$$\phi = -p\frac{2\pi}{\lambda}\Delta R_s, \tag{2.10}$$

where $p = 2$ for "ping-pong" systems and $p = 1$ for single-transmitter systems, λ is the carrier wavelength and ΔR_s is the slant range difference from a point on the surface to the two antennas. The expression for the phase difference can be approximated by

$$\phi \approx -\frac{2\pi}{h_a}\Delta h, \tag{2.11}$$

where Δh is the relative height of the surface and h_a is the height of ambiguity:

$$h_a = \frac{\lambda R_s \sin\theta_i}{pB_\perp}, \tag{2.12}$$

where R_s is the slant range and θ_i is the incident angle. The height of ambiguity is used in the performance model to convert the interferometric phase error to the height estimate error.

2.2.3. Measurement Error

General Model

The interferometric phase measured by a single-pass cross-track interferometer, where the two satellites are in a close formation, will have contributions both from the topography of the scene ϕ_{topo}, and from motion in the direction of the line of sight $\phi_\parallel$ due to the perpendicular and along-track baseline respectively. Additionally, the interferometric phase signal ϕ will be modified by white noise ϕ_n due to the thermal noise of the SAR electronics and the decorrelation of the scene

$$\phi = \phi_{\text{topo}} + \phi_\parallel + \phi_n. \tag{2.13}$$

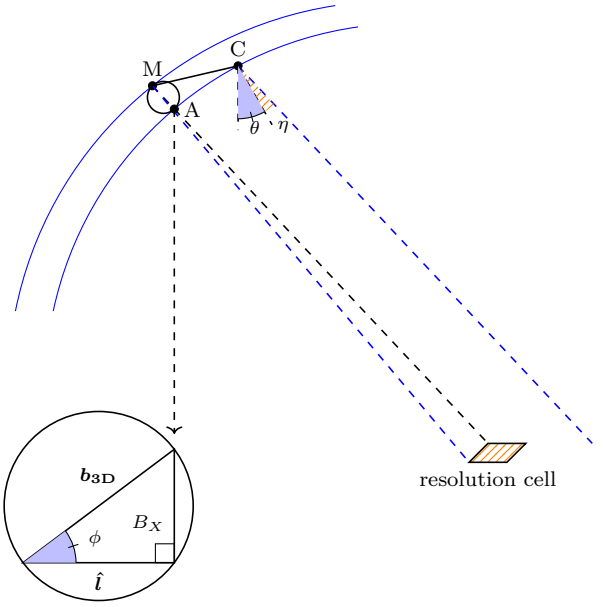

Figure 2.7.: Cross-track baseline with squinted line of sight.

We assume that the receiving SAR instruments follow the design of the Harmony companions. Each has a planar antenna made from two subapertures separated along the antenna's longitudinal axis. One subaperture is at the aft of the antenna structure, and the other at the fore as illustrated in Figure 2.8. Each of the two subapertures forms a separate SAR image. The instrument forms an improved SAR image by combining the images from the individual phase centers, resulting in a better Noise-equivalent Sigma Zero (NESZ) and Azimuth Ambiguity to Signal Ratio (AASR). Unless stated otherwise, the imaging and interferometric performance discussed in the chapter refer to the performance of the combined signal rather than that of the single-channel signal.

Each receiving SAR estimates the phase due to the motion of the surface $\phi_{\|}$, also known as the "along-track interferometry (ATI) phase", using its two individual phase centers. The estimate $\hat{\phi}_{\|}$ is subtracted from the measured phase to remove the undesired motion component, giving an estimate of the topographic phase. The error of the height estimate includes the error of estimating the ATI phase $\epsilon_{\|}$

$$\hat{\phi}_{\text{topo}} = \phi_{\text{topo}} + \epsilon_{\|} + \phi_n, \tag{2.14}$$

$$\epsilon_{\|} = \phi_{\|} - \frac{B_{\|}}{B_{\|s}}\hat{\phi}_{\|}, \tag{2.15}$$

where the estimate of the ATI phase acquired using the two on-board phase centers is scaled by $B_{\|}/B_{\|s}$. The scaling factor arises because the estimate of the

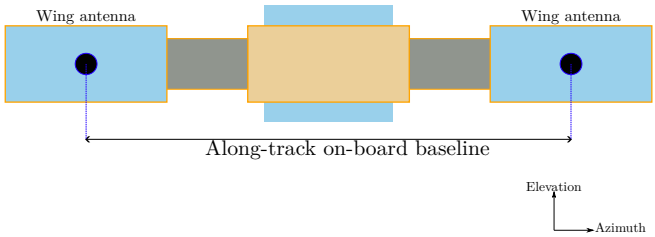

Figure 2.8.: The planar antenna array assumed by the performance model. Two phase centers are positioned at the aft and fore of the antenna structure.

motion phase is obtained with the on-board along-track baseline, $B_{\parallel s}$, which is different from the effective baseline of the formation.

We use the Cramer-Rao lower bound [25] to estimate the standard deviation of the interferometric phase

$$\sigma_\phi = \sqrt{\frac{1-\gamma^2}{2N_l\gamma^2}}, \tag{2.16}$$

where γ is the coherence and N_l is the number of independent looks. The coherence is the product of the partial coherence factors [26]

$$\gamma \approx \gamma_{\mathrm{SNR}}\gamma_B\gamma_t\gamma_{\mathrm{Amb}}\gamma_{\mathrm{Vol}}, \tag{2.17}$$

where the right-hand side of the equation describes the contributions to the error due to noise including quantization errors (γ_{SNR}), baseline decorrelation (γ_B), temporal decorrelation (γ_t), ambiguities (γ_{Amb}), and volumetric scattering (γ_{Vol}). Since the effect of ambiguities on Harmony is addressed in [27], we do not consider it in this chapter.

At C-band, the electromagnetic signal practically does not propagate into the water. However, scatterers within a resolution cell follow the highly varying surface topography of the ocean, which produces volumetric decorrelation. We follow the same approach as in [28] and model the mean topographic height of the ocean surface as a Gaussian variable with zero mean. The volumetric decorrelation due to the surface waves is given by

$$\gamma_{\mathrm{Vol}} = \mathrm{e}^{-\frac{1}{2}(2\pi/h_a)^2\sigma_h^2}, \tag{2.18}$$

where the standard deviation of the ocean height is related to the significant wave height (SWH) by $\mathrm{SWH} = 4\sigma_h$.

The coherence due to temporal decorrelation depends on the temporal lag between acquisitions [29]

$$\gamma_t = \mathrm{e}^{-\tau^2/\tau_c^2}, \tag{2.19}$$

where $\tau = \frac{B_\parallel}{2v}$ is the lag between acquisitions due to the effective along-track baseline $\frac{B_\parallel}{2}$ and platform velocity v, and $\tau_c \approx 3.29\lambda/U$ approximates the coherence time at wind speed U [26].

Baseline decorrelation occurs due to spectral shifts between SAR acquisitions with different incidence angles. However, filtering the two SAR signals to a common frequency band avoids the decorrelation [30] at the cost of reducing the effective number of looks. We assume that the SAR signals are filtered to correct for the spectral shift. Therefore, we assume $\gamma_B = 1$ and account for the reduction in the number of looks by a factor $\gamma_B = 1 - B_\perp/B_{\perp,c}$, where $B_{\perp,c}$ is the critical baseline [31].

Instrument Specific Parameters

The coherence due to noise depends on the signal-to-noise ratio (SNR), which is a function of the NESZ and the normalized radar cross-section (NRCS), σ^0, of a given resolution cell [32] [33]

$$\gamma_{\mathrm{SNR}} = \frac{1}{1 + \mathrm{SNR}\,(\sigma^0, \mathrm{NESZ})^{-1}}. \tag{2.20}$$

The NESZ depends on the system parameters and the antenna gains of both the transmitter and receiver. Thus, to produce performance estimates, assumptions need to be made about the antenna gain and pattern. In the Harmony case study, the antenna pattern of the transmitter is calculated using the specification of Sentinel-1. The effective area of the Harmony companions is computed for three elements with identical, $2.6\,\mathrm{m} \times 0.66\,\mathrm{m}$, fore and aft elements that are separated by $10\,\mathrm{m}$. The dimensions were selected to match the design from industry. When all phase centers on-board the Harmony satellites are used as a single antenna, the NESZ varies from $-22\,\mathrm{dB}$ to $-28.5\,\mathrm{dB}$ as shown in Figure 2.9. In the quasi-monostatic case study, the transmit and receive antennas are the same, and any realistic parameters can be used. However, as will be explained in the next section, the aim of the quasi-monostatic case is to illustrate the effect of optimizing the squint without being constrained by the need to have a good overlap of the receiver and transmitter beams on the surface. Thus, all system parameters, including the NESZ, NRCS, and on-board phase center separation, are kept the same as those in the Harmony case except for the antenna squint.

The backscattering coefficient of a SAR system observing the ocean surface depends on many factors such as the instrument viewing geometry, surface roughness, the dielectric properties of the sea, and the waves being driven by the wind. Three mechanisms drive the wave-induced changes to the backscattered power: specular reflection, Bragg scattering, and wave breaking. We apply a multistatic NRCS model based on the model developed by Yuan [34] to the geometry of Harmony, i.e. the incident and scattered azimuth and incidence angles due to the separation of transmitter and receiver, to estimate σ^0 at different wind speeds. The NRCS for $5\,\mathrm{m\,s^{-1}}$, $10\,\mathrm{m\,s^{-1}}$ and $15\,\mathrm{m\,s^{-1}}$ downwind is shown in Figure 2.10.

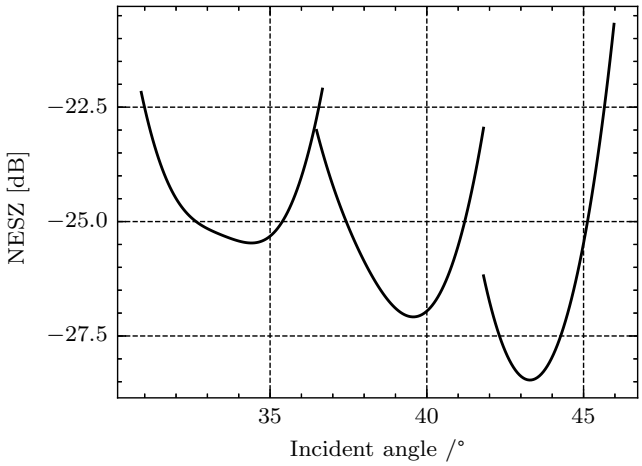

Figure 2.9.: The estimated NESZ of Harmony with Sentinel-1 as the illuminator. The three subswaths of Sentinel-1's IW mode are visible by the discontinuities between the three quadratic curves.

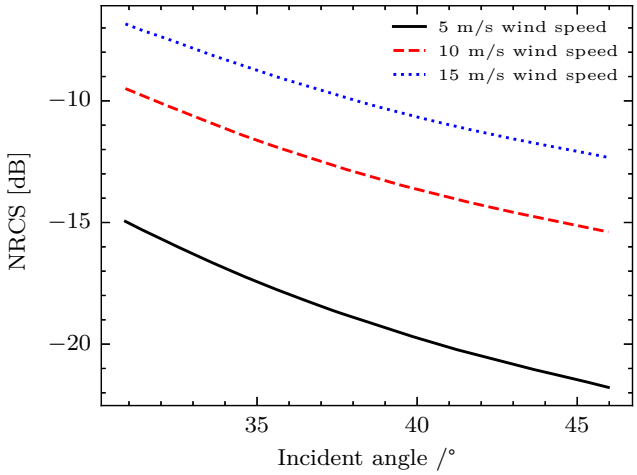

Figure 2.10.: The estimated NRCS in the vertical co-polarized channel for Harmony over a sea surface that is driven by a wind with speeds $5\,\mathrm{m\,s^{-1}}$, $10\,\mathrm{m\,s^{-1}}$ and $15\,\mathrm{m\,s^{-1}}$. The magnitude of the normalized radar cross-section falls as the incidence angle moves towards the far range. .

The number of independent looks is the ratio of the product resolution ρ_{L2} and

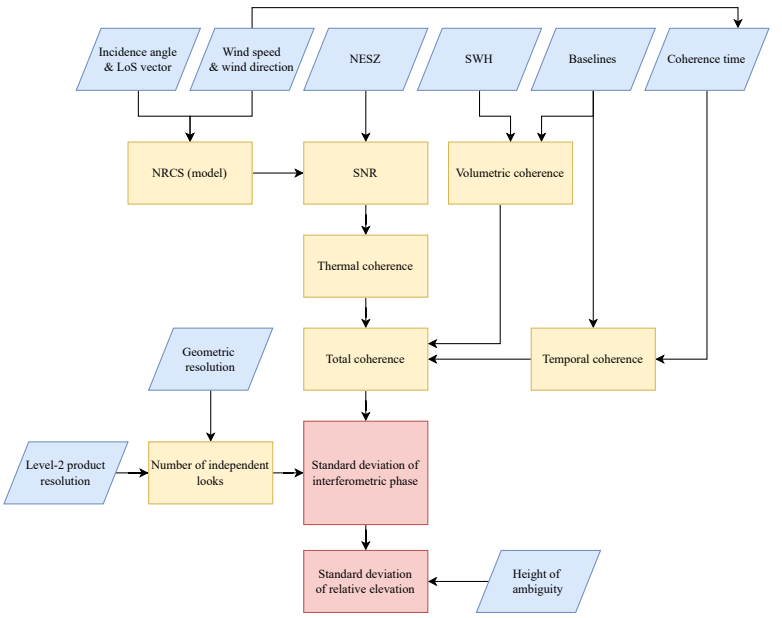

Figure 2.11.: Flowchart of the interferometric height standard deviation calculation.

nominal geometric resolution ρ_{2D}

$$N_l = \gamma_B \frac{\rho_{\mathrm{L2}}}{\rho_{\mathrm{2D}}}. \tag{2.21}$$

Sentinel-1 in IW mode has a spatial resolution of $5\,\mathrm{m} \times 20\,\mathrm{m}$. The level-2 product resolution depends on the accuracy we want to achieve. For relative elevation measurements with accuracy of $10\,\mathrm{cm}$ over the majority of the swath and latitudes, $3\,\mathrm{km} \times 3\,\mathrm{km}$ is sufficient which corresponds to $N_l = 90 \times 10^3 \gamma_B$.

With the geometry of the formation, the number of looks, and the SNR determined we compute the total coherence of the interferometer

$$\gamma = \gamma_{\mathrm{SNR}} \gamma_t \gamma_{\mathrm{Vol}}. \tag{2.22}$$

Following the same procedure, we also calculate the coherence due to the temporal and thermal decorrelation of the ATI phase estimate. Volumetric decorrelation does not impact the on-board along-track phase estimate because the separation of the phase centers only has a small residual perpendicular component. The standard deviation for these two sources of uncertainty is calculated using the Cramer-Rao lower bound given in (2.16). Due to the addition of the estimation error to the estimate of the topographic phase (2.14), the uncertainty of the

ATI phase estimate contributes to the overall system uncertainty

$$\sigma_\phi = \sqrt{\sigma_{\phi_n}^2 + \left(\frac{B_\parallel}{B_{\parallel s}}\right)^2 \sigma_{\hat{\phi}_{\mathrm{ATI}}}^2}. \tag{2.23}$$

The addition of the two uncertainties implicitly assumes that the two are statistically independent. Figure 2.11 shows a schematic representation of the method used to obtain the standard deviation of the height estimate. The process illustrated in the flowchart is applied separately to the main interferometer, formed by the Helix formation of SAR satellites, and to the along-track on-board interferometer, formed by the two wing phase centers on-board each satellite, to calculate σ_{ϕ_n} and $\sigma_{\hat{\phi}_{\mathrm{ATI}}}$. The SNR of the latter is less than the SNR of the former because only one of the phase centers of the receive antenna is used to obtain the on-board ATI phase estimate. Additionally, the temporal coherences of the two systems differ due to the different geometry of the satellite formation compared to the two phase centers on-board one of the two companions. The on-board ATI phase estimate has a fixed purely along-track baseline between the two phase centers while the effective baseline of the main interferometer varies along the orbit due to the Helix formation.

2.3. Performance Analysis

The interferometric model presented in Section 2.2.2 is applied to two case studies: the Harmony companions with Sentinel-1 as the transmitter; A pair of SARs in a Helix formation with one of the two acting as the transmitter. We use a wind speed of $5\,\mathrm{m\,s^{-1}}$ in both case studies, while the performance of Harmony is also evaluated at $U = 10\,\mathrm{m\,s^{-1}}$ and $U = 15\,\mathrm{m\,s^{-1}}$ to assess the change in performance with wind speed. For the purposes of interferometric performance the track is symmetric over the ascending and descending parts of the orbit; hence, only the descending part of the orbit is used to compute the results. In both case studies, once the state vector of the main satellite of the Helix formation is determined, the position of the deputy satellite is computed by applying the formation parameters to (2.3). Then, the relative position vector and the line of sight of the main satellite are used in (2.5) and (2.9) to calculate the effective baselines. With the effective baselines computed, the measurement uncertainty is calculated as explained in 2.2.3.

2.3.1. Harmony

Sentinel-1 [35] defines the reference orbit and the Harmony companions fly in a Helix formation lagging Sentinel-1 by $350\,\mathrm{km}$. The parameters relevant to the model are listed in Table 2.1. Once the orbit of Sentinel-1 is computed, the position of the first companion, Concordia, which is used as the reference vehicle of the close formation, is calculated using the same orbital parameters as Sentinel-1 but with the mean anomaly of the orbit at the same epoch shifted to lag S1 by $350\,\mathrm{km}$. Thus, Concordia travels in the same orbital plane as S1 with a mean lag of

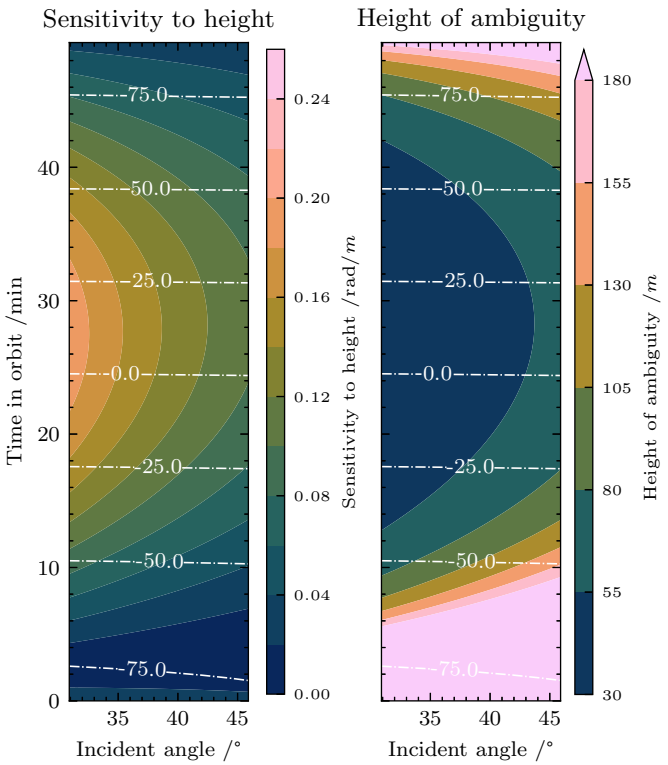

Figure 2.12.: Harmony's sensitivity to height and height of ambiguity of the optimized formation. The latitudes of maximum sensitivity and minimum height of ambiguity occur where the effective perpendicular baseline reaches its maximum.

$350\,\mathrm{km}$ and Discordia has an orbit relative to Concordia determined by the formation parameters.

SAR imaging requires sufficient overlap of the transmitter and receiver beam on the imaged surface. Hence, Concordia steers its antenna beam to align with that of Sentinel-1 on the surface, leading to a range-dependent squint. As a result, $\tan\eta$ cannot freely adhere to (2.6) to minimize $B_{\parallel}$. $B_{\parallel}$ passes through zero if the ratio of e_Y to $\Delta\Omega$ follows (2.6). However, the squint of the receiver decreases with range as it tracks the line of sight of the illuminator. Consequently, $B_{\parallel}$ cannot be reduced to 0 for the entire swath.

The close formation is defined by two parameters: the vertical separation due to a difference in the magnitude of the eccentricity vector $a\Delta e$, and a horizontal separation due to a difference in the ascending nodes $a\Delta\Omega$. Two formations are considered in the analysis: One that does not follow the condition shown in (2.6) for minimizing $B_{\parallel}$; and a second formation that does so that the effect of using the squint to enhance performance can be illustrated. The parameters of the two

Table 2.1.: Relevant orbital and processing parameters. IW refers to Sentinel-1's Interferometric Wide Swath operating mode. The number of independent looks is calculated according to (2.21) for a product resolution of $3\,\mathrm{km} \times 3\,\mathrm{km}$ and the nominal geometric resolution of S1 in IW mode ($5\,\mathrm{m} \times 20\,\mathrm{m}$).

Parameter	Value	Unit
Center frequency	5.405	GHz
Platform mean speed	7590	$\mathrm{m\,s^{-1}}$
Incident angle Sentinel-1 (IW)	30–46	°
Lag between Sentinel-1 and Harmony formation	350	km
Separation due to inclination difference	0	m
Companion constant along-track separation	0	m
Number of independent looks	90×10^3	-

formations are listed in Table 2.2.

The careful reader would raise the question of the optimal combination of Δe and $\Delta\Omega$. Forcing the along-track baseline to go through zero can be achieved by selecting Δe and $\Delta\Omega$ to follow the ratio of (2.6). However, the condition places no constraints on the magnitude of the values. A strategy of having the smallest $B_{\parallel}$ at all latitudes and incidence angles would require selecting the smallest possible values that are operationally safe. Yet, this would mean that sensitivity to height would be too small to achieve good performance. On the other hand, raising the two parameters leads to higher sensitivity at the cost of higher extreme values of along-track baseline and smaller height of ambiguity. Heights of ambiguity smaller than $30\,\mathrm{m}$ can cause phase-unwrapping problems in regions with rough terrain.

Since Harmony will also perform acquisitions over land, the formation parameters of the optimized case were selected as the highest values that provide a minimum $h_a = 30\,\mathrm{m}$. Figure 2.12 shows the sensitivity and height of ambiguity of Harmony for the optimized formation. The sensitivity reaches its maximum at the middle latitudes, where the effective perpendicular baseline is at its largest value. The sensitivity varies from $0.01\,\mathrm{rad\,m^{-1}}$ to $0.24\,\mathrm{rad\,m^{-1}}$, except for a zone from $67.5°$ to $75°$S where the satellites of the formation cross and the separation tends to zero causing the sensitivity to also tend to zero. The height of ambiguity follows the inverse progression ranging from a minimum of $30\,\mathrm{m}$ to a maximum of $1000\,\mathrm{m}$. Values above $180\,\mathrm{m}$ are not shown in the plot to avoid losing the detail in the variation of the small values of h_a which are critical. The sensitivity and height of ambiguity of the non-optimized formation follow the same pattern as those of the optimized formation, but the sensitivity has a maximum at $0.25\,\mathrm{rad\,m^{-1}}$ and the height of ambiguity a minimum of $25\,\mathrm{m}$.

An additional parameter that affects the performance is the significant wave height. The volumetric decorrelation depends inversely on the SWH and the sensitivity. Figure 2.13 illustrates γ_{Vol}, at the latitude with the largest perpendicular

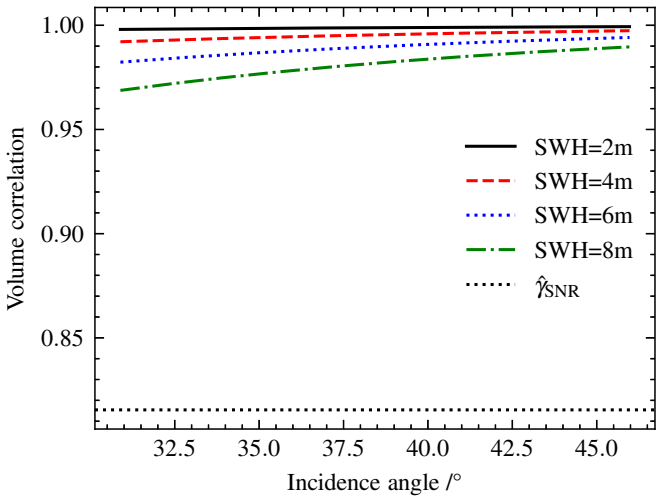

Figure 2.13.: The volumetric correlation as a function of incidence angle for different values of significant wave height. The mean thermal coherence is plotted using the black dashed line.

baseline of the optimized formation, for different values of SWH and the mean γ_{SNR} as a function of incidence angle. The figure shows that even at $8\,\mathrm{m}$ of significant wave height, the volumetric decorrelation is not as significant as thermal decorrelation. From this point on, we assume a significant wave height of $6\,\mathrm{m}$ for both case studies, which is a conservative number since the majority of the ocean has smaller waves.

Figure 2.14 illustrates the estimated sea surface height error of the interferometer at a wind speed of $5\,\mathrm{m\,s^{-1}}$. The error shown in the figure is due to the thermal, temporal, and volumetric decorrelation of the signal. The results indicate that the error is within $5\,\mathrm{cm}$ over the majority of the swath and latitudes. The performance rapidly deteriorates close to the poles because the two companions fly over one another and $B_{\perp}$ tends to its minimum value. In turn, the height of ambiguity tends to its maximum, pushing the uncertainty up. At the midpoint of an ascending or descending pass, the coherence due to the time lag τ is at its minimum because $B_{\parallel}$ reaches its maximum at the near range. However, this is not visible because $B_{\perp}$ tends to a maximum at the same point and compensates for the loss of along-track coherence. The orbital parameters of the second formation are chosen to minimize $B_{\parallel}$ at the mid-range, resulting in a wider valley of low error in the second formation compared to the unoptimized formation. Both plots show a slight deterioration of performance at the far range due to the decrease of NRCS with increasing incidence angle.

Both plots in Figure 2.14 exhibit discontinuities at $\theta_i = 36.5°$ and $\theta_i = 41.9°$. The discontinuities are caused by the jumps in the NESZ of the illuminator between subswaths 1–2 and 2–3 as shown in Figure 2.9. These abrupt changes in the NESZ

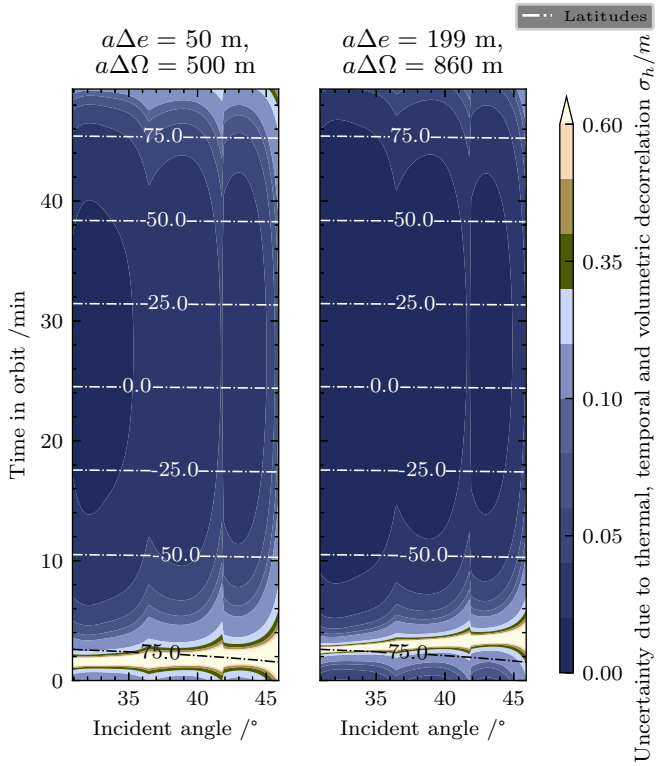

Figure 2.14.: The estimated SSH uncertainty of the system due to thermal, spatial and temporal decorrelation of the signal in terms of 1σ at a wind speed of $5\,\mathrm{m\,s^{-1}}$.

Table 2.2.: The two companion formations considered in the simulations. We refer to the first as the unoptimized formation and to the second as the optimized formation. Each is defined by the vertical separation due to a difference in the magnitude of the eccentricity vector $a\Delta e$, and a horizontal separation due to a difference in the ascending nodes $a\Delta\Omega$.

$a\Delta e$/m	$a\Delta\Omega$/m
50	500
199	860

of the instrument are the result of the TOPS operation [36]. The discontinuities in the NESZ propagate to σ_n and $\sigma_{\hat{\phi}_{\mathrm{ATI}}}$ through (2.20) and (2.16). Hence, they appear in the results of the SSH uncertainty that follow.

The second source of uncertainty comes from the ATI phase estimate produced

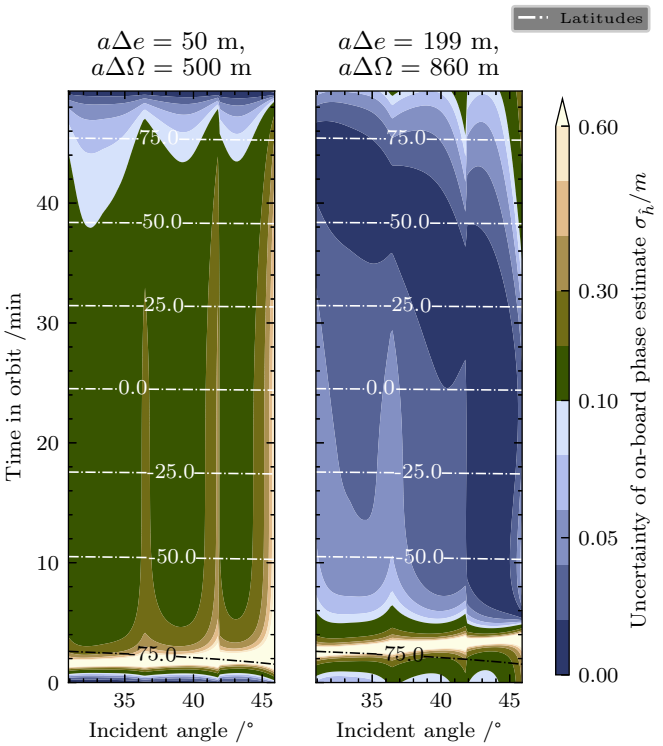

Figure 2.15.: The uncertainty of the phase estimate due to the along-track separation in terms of 1σ at a wind speed of $5\,\mathrm{m\,s^{-1}}$. The ATI phase estimate ϕ_{ATI} is obtained using the two phase centers on-board each Harmony companion.

by the two phase centers on-board the Harmony companions. The error is shown in Figure 2.15. Structurally the uncertainty of the ATI phase is similar to that of the system, with the error peaking close to the poles, and deteriorating towards the far-range of the swath. Yet, we observe that the error contribution of the ATI estimate is larger than the error of the system, particularly in the unoptimized formation. There are two effects driving this phenomenon:

1. The SNR of the two SAR images, coming from the individual on-board phase centers, from which the ATI phase is estimated is $4.25\,\mathrm{dB}$ worse than the SNR of the combined system. The effect of the reduced SNR is particularly visible in the mid to far range of the optimized formation.

2. The scaling factor $h_a B_{\parallel}/B_{\parallel s}$ that converts the individual estimator's standard deviation to the standard deviation of the combined system estimator increases the error. Particularly in the unoptimized formation, where $B_{\parallel}$

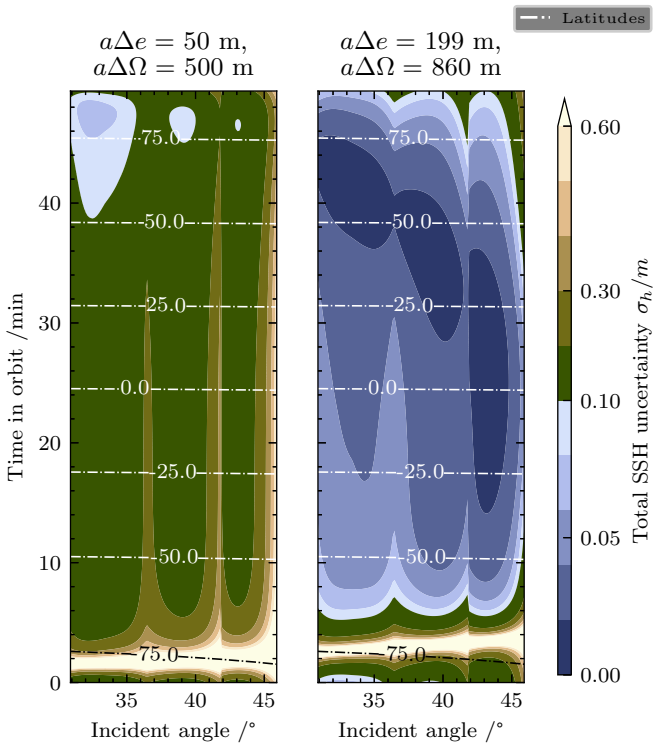

Figure 2.16.: The total SSH uncertainty in terms of 1σ at a wind speed of $5\,\mathrm{m\,s^{-1}}$. The total uncertainty is combined by summing the uncertainty of the interferometer shown in Figure 2.14 with the uncertainty due to the ATI phase estimate shown in Figure 2.15. In order to sum the two uncertainties the assumption that they are uncorrelated is made. From the results it can be seen that the uncertainty due to the ATI phase estimate dominates the overall performance of the interferometer.

does not tend to $0\,\mathrm{m}$ at any point, the scaling of the error by the ratio of the system along-track baseline to the on-board baseline dominates the error.

The total error of the SSH measurement is shown in Figure 2.16. The total standard deviation is found using (2.23). The error is in the order of $10\,\mathrm{cm}$ over the majority of the swath, throughout the orbit, except towards the poles. The best performance is achieved near the Equator because at that point the formation has the largest cross-track baseline. The performance of the optimized formation shown in Figure 2.16 achieves a standard error of $6\,\mathrm{cm}$ or less over the entire swath, and over the majority of the track. At latitudes below $50°$S and above $75°$N the standard error increases, particularly in the far range. The latitudes that correspond to the crossing point of the formation show a severe deterioration of performance

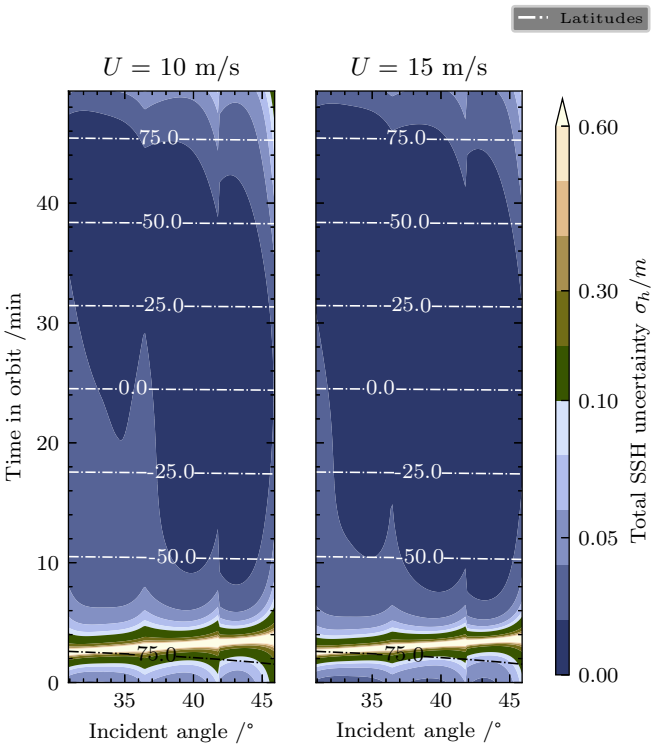

Figure 2.17.: The total SSH uncertainty in terms of 1σ for the optimized formation. The left panel shows the error at a wind speed of $10\,\mathrm{m\,s^{-1}}$ and the right panel at a wind speed of $15\,\mathrm{m\,s^{-1}}$.

due to the perpendicular baseline tending to zero. The standard error of the optimized formation at wind speeds of $10\,\mathrm{m\,s^{-1}}$ and $15\,\mathrm{m\,s^{-1}}$ is shown in Figure 2.17. The error is considerably improved at higher wind speeds, with $4\,\mathrm{cm}$ or less at almost the entire range and all latitudes except for the crossing point of the Helix formation. The improvement in performance is driven by the higher SNR due to the brighter NRCS of the sea surface.

2.3.2. Quasi-monostatic Interferometer

Importantly, despite the improvement that using a squinted line of sight to decrease the effective along-track baseline brings to the interferometric height estimate, there are two factors limiting the performance of a bistatic interferometer like the one presented in the Harmony case study. The first is the drop in SNR, particularly in the signal coming from the individual phase centers at the far range which is visible at low wind speeds, where the surface is less bright. Since the SNR is driven by the NESZ of the instrument and the NRCS, improving this aspect of

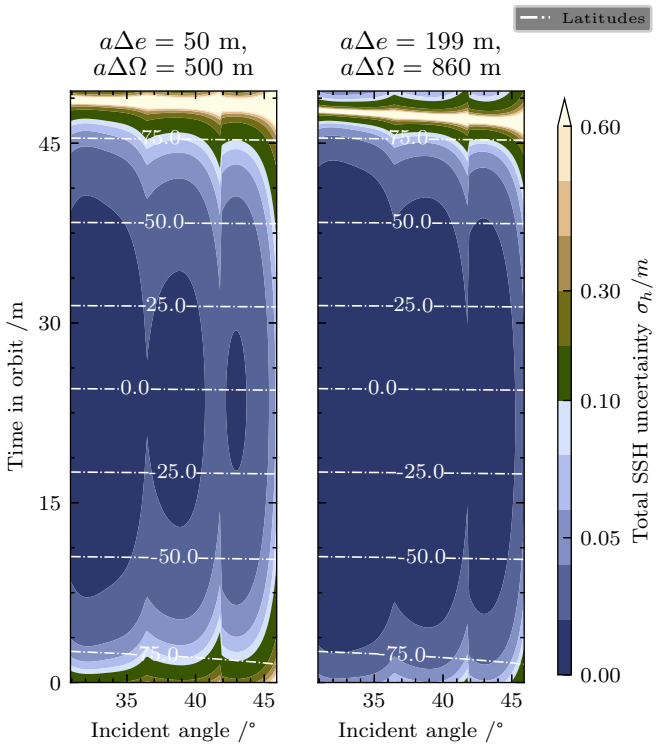

Figure 2.18.: The total SSH uncertainty in terms of 1σ of the quasi-monostatic interferometer at a wind speed of $5\,\mathrm{m\,s^{-1}}$.

the performance can only be achieved by changing the design of the instrument, which is outside the scope of this chapter.

The second factor is the dependence of the squint on the incidence angle. The dependence means that for a given point in the satellite formation, there is not a single squint angle that minimizes $B_{\parallel}$ but rather a locus of angles. Minimizing $B_{\parallel}$ would require a range-dependent steering of the antenna beam. For Harmony this ranges from $5°$ to $12°$, which is difficult to implement. This requirement can be relaxed if one of the satellites of the Helix formation acts as the transmitter. In other words, one of the two satellites of the Helix formation would be a monostatic SAR with the second satellite being a bistatic receiver. Overlapping the beams, while still necessary, becomes trivial, and the squint is virtually range independent because the along-track transmitter-receiver separation is on the order of meters instead of kilometers.

In this section we present the performance of a quasi-monostatic SAR flying in a Helix formation with a passive companion. The antenna beams are steered according to (2.6) to minimize $B_{\parallel}$. Unless stated, parameters are kept the same with the Harmony case to highlight the effect of the squint on the performance.

Figure 2.18 shows the standard error of the quasi-monostatic configuration.

The results show a lower error at $5\,\mathrm{m\,s^{-1}}$ compared to that of the Harmony case at the same wind speed. Sub-$5\,\mathrm{cm}$ error is achieved for the entire swath between $70°$S and $70°$N and the performance starts to degrade at latitudes higher and lower of $70°$ and $-70°$. The plots are shifted in latitude compared to those of Harmony because the main satellite of the close formation has been assumed to have the mean anomaly of S1, whereas in the Harmony case it is displaced behind S1 by $350\,\mathrm{km}$.

The degradation due to the SNR at the far range only starts to become apparent at the edge of the swath and at the two ends of the latitude where the perpendicular baseline decreases. $B_{\parallel}$ is kept to sub-meter values at all values of incidence angle and latitude. Thus, γ_{ATI} of the formation is kept close to 1 at the far range which keeps the total coherence is still high despite the SNR degradation. The error due to the on-board along-track phase estimate makes a negligible, sub-centimeter, contribution to the total error due to the scaling factor $h_a B_{\parallel}/B_{\parallel s}$ being small.

2.3.3. Spatial and Spectral Scales

To assess the instrument performance in terms of whether it can capture the topography of the ocean at the submesoscales (scales between $10\,\mathrm{km}$ and $100\,\mathrm{km}$), the standard deviation of the height estimate, illustrated in Figure 2.16, needs to be translated into a power spectral density and compared with the variation of the power spectral density of the sea surface height as a function of wavenumber. The density of the instrument's random error forms a noise floor, and its intersection with the density of the SSH signal determines the spatial scales that the instrument resolves.

The power spectral density of SSH is approximated by a power law in the wavelength range of $70\,\mathrm{km}$ to $250\,\mathrm{km}$ derived from along-track altimeter observations. The spectral slope in the $30\,\mathrm{km}$ to $120\,\mathrm{km}$ wavelength range is between -1.56 and -2.14 in the low-latitude ($30°$S–$30°$N) regions [37]. The spectral slope in the $80\,\mathrm{km}$ to $280\,\mathrm{km}$ wavelength range is $-\frac{11}{3}$ in the midlatitudes ($30°$S–$60°$S and $30°$N–$60°$N) and reaches -5 in the high latitude regions on average [38]. We assume that the power law that governs the SSH power spectral density extends down to $1\,\mathrm{km}$, similarly to [19], and extrapolate two SSH power spectral densities with spectral slopes of -1.56 and $-\frac{11}{3}$. The flatter slope is chosen for the low-latitude regions because it is derived from Sentinel-3A data which can resolve finer spatial scales than the altimeters which are used to derive the steeper slope [37]. $-\frac{11}{3}$ is chosen as an average slope representative of the midlatitudes. A spectral slope for high latitudes is not used in the analysis because the perpendicular baseline tends to zero in the polar part of the orbit, and the interferometric performance is not representative of the system capabilities.

The instrument random error is modeled as white noise with a flat power spectral density. The spectral law for altimeter data is specified as a one-dimensional spectrum in the azimuth direction. The level of the density is determined by the

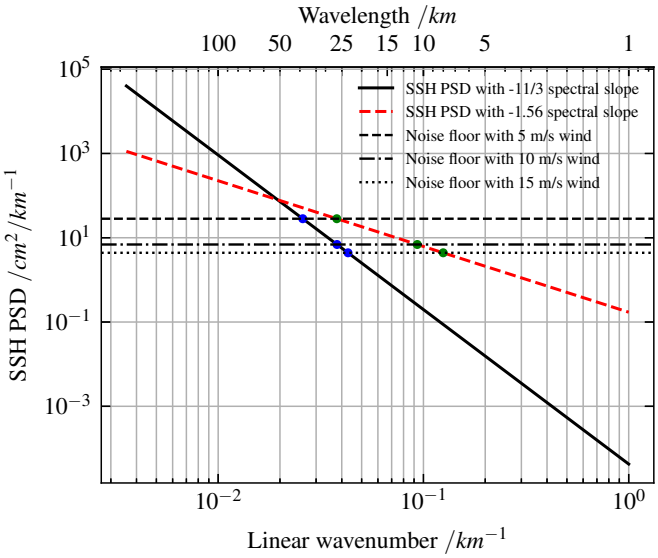

Figure 2.19.: The power spectral density of the sea surface height modeled using a power law and the noise floor of the Harmony interferometer. The solid black line uses a spectral slope of $-\frac{11}{3}$ which is the average at middle latitudes (30°S–60°S and 30°N–60°N). The dashed red line uses a spectral slope of -1.56 which is the average at low latitudes (30°S–30°N). The horizontal dashed, dashed and dotted, and dotted lines are the noise floor for wind speeds of $5\,\mathrm{m\,s^{-1}}$, $10\,\mathrm{m\,s^{-1}}$ and $15\,\mathrm{m\,s^{-1}}$ respectively. The point of intersection of the noise floor with the SSH spectrum determines the smallest wavelength that the system can resolve. The intersections of the noise floors are indicated in blue for the spectrum with $-\frac{11}{3}$ slope and green for the spectrum with a slope of -1.56.

variance of the error and the sampling linear wavenumber of the instrument

$$S_{hh} = \frac{\sigma_h^2}{\nu_{s_x} Q}, \tag{2.24}$$

where S_{hh} is the power spectral density of the random error and ν_{s_x} is the sampling linear wavenumber determined by the level-2 resolution of the relative height estimate. Since the SSH density is one-dimensional in azimuth, we can average the samples in range up to the Nyquist sampling interval that corresponds to the smallest scale that the interferometer should resolve. Q is the oversampling factor in the range direction given by the ratio of the range sampling wavenumber to the Nyquist wavenumber.

To evaluate the noise floor against the spectral density of the measurement we set the smallest separable scale in range to $15\,\mathrm{km}$. Resolving wavelengths down

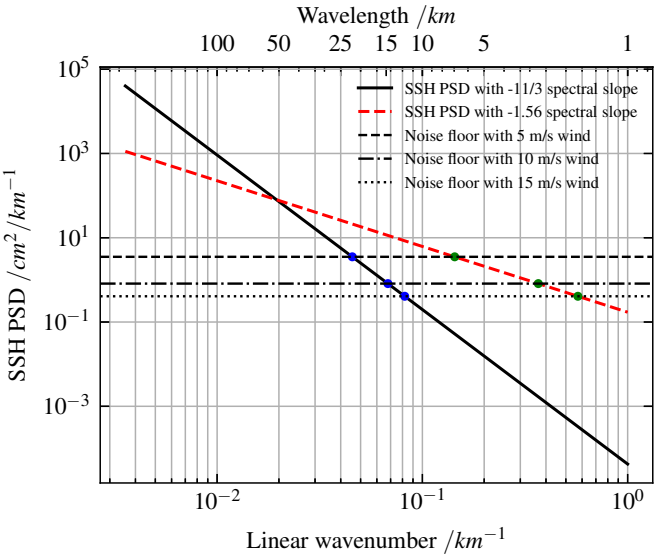

Figure 2.20.: The power spectral density of the sea surface height and the noise floor of the quasi-monostatic interferometer. The PSD of the SSH is the same as the one used in Figure 2.19.

to $15\,\mathrm{km}$ requires a Nyquist interval of $7.5\,\mathrm{km}$ leading to an oversampling factor of 2.5 for a product resolution of $3\,\mathrm{km} \times 3\,\mathrm{km}$. We then convert the one-dimensional power spectral density of the error to a single-sided density by multiplying it by 2.

We use the standard error of the relative height estimate presented in Figure 2.16 to compute the spectral density of the noise floor. As previously discussed, the standard deviation of the relative height estimate varies with range and with the position of the satellite along its orbit. To compare the power spectral density of the SSH and of the error, a singular value is needed for σ_h. Because of the tendency of the error to peak towards high values at the far range that are not representative of the majority of the swath, the median of the standard deviation is used to obtain a representative average value of the standard deviation. The values at the crossing of the two companion satellites are not considered in the calculation because the interferometric performance at that point in the formation is not representative of the system capabilities. In the Harmony case study, the median standard deviation is $3.4\,\mathrm{cm}$, $1.7\,\mathrm{cm}$ and $1.4\,\mathrm{cm}$ while in the quasi-monostatic case, it is $1.2\,\mathrm{cm}$, $0.6\,\mathrm{cm}$ and $0.5\,\mathrm{cm}$ for the three wind speeds, respectively. The density of the noise floor is computed by substituting the median standard error into (2.24). The spectral densities of the SSH, modeled with spectral slopes of -1.56 and $-\frac{11}{3}$, and the noise floors corresponding to Harmony and the quasi-monostatic interferometer are shown in Figures 2.19 and 2.20 respectively. We note that the error spectrum does not include systematic errors which we expect to have a non-flat spectral envelope. Thus, the resolution described in the following paragraphs shows the

potential of formation-flying interferometers, rather than a complete description of the instrument resolution, which will deteriorate when systematic errors with components in the submesoscale wavenumbers are included in the spectrum.

The intersection of the noise floor with the spectrum of the SSH determines the smallest wavelength that can be resolved by the instrument before the estimate is flooded by noise. The intersections of the Harmony noise floor with the steeper spectrum correspond to wavelengths of $38.7\,\mathrm{km}$, $26.4\,\mathrm{km}$ and $23.3\,\mathrm{km}$ for wind speeds of $5\,\mathrm{m\,s^{-1}}$, $10\,\mathrm{m\,s^{-1}}$ and $15\,\mathrm{m\,s^{-1}}$ respectively. In the case of a spectrum with a flatter slope, as is the case with low-latitude regions, a more favorable performance is achieved with wavelengths of $26.4\,\mathrm{km}$, $10.7\,\mathrm{km}$ and $8.0\,\mathrm{km}$ for the same respective wave speeds. The results show that the performance is strongly dependent on wind speed. Higher wind speeds lead to a rougher ocean surface and a higher NRCS, which in turn improves the signal-to-noise ratio and lowers the noise floor. The results suggest that Harmony has the potential to resolve ocean surface height variations at spatial scales of approximately $26\,\mathrm{km}$ and $8\,\mathrm{km}$ wavelengths for moderate to high speeds.

The spectral density plot of the quasi-monostatic interferometer shows better results than the Harmony case. The noise floor intersects the steeper spectral density at wavelengths of $21.9\,\mathrm{km}$, $14.7\,\mathrm{km}$ and $12.2\,\mathrm{km}$ and the flatter density at $7.0\,\mathrm{km}$, $2.7\,\mathrm{km}$ and $1.8\,\mathrm{km}$ wavelengths. It should be noted that wavelengths below $15\,\mathrm{km}$ would not be resolvable in the range direction as a sampling interval of $7.5\,\mathrm{km}$ was assumed. The numbers represent the potential of the instrument in combination with a squinted line of sight that is optimized for a given formation. Figure 2.20 illustrates that the concept of using a squinted line of sight to decrease the effective along-track baseline and reduce the temporal decorrelation of the surface allows the estimation of relative SSH at submesoscales, from $22\,\mathrm{km}$ to $15\,\mathrm{km}$, at all wind conditions and over a wide swath.

2.3.4. Error Breakdown

In addition to the random error of the instrument, systematic errors and oceanic and atmospheric biases also affect the quality of the SSH estimate. Table 2.3 contains a breakdown of the main sources of error that we expect a formation-flying interferometer that uses the optimized formation to have. Since some of the errors are strongly wind dependent, we provide mean values at wind speeds of $5\,\mathrm{m\,s^{-1}}$ and $15\,\mathrm{m\,s^{-1}}$. The random instrument error also depends on the design of the instrument and the operation of the radars (bistatic/quasi-monostatic). In Table 2.3 we show the mean instrument error of Harmony over all incidence angles and latitudes, excluding values above $45°$ of incidence angle and latitudes lower than $70°$S. We exclude these values because the standard error rises sharply in the last $1°$ of the swath and at the latitudes when the two satellites cross, strongly biasing the mean towards a value that is not representative of the majority of the swath and latitudes.

The error due to the troposphere is assumed to be constant with wind speed, and the mean value over the incidence angles is used in the table. The sea-state bias depends on the wind speed and direction. The bias will be constant over

the swath and opposite in sign to near-nadir-looking altimeters. We expect to achieve similar performance in terms of sea-state bias estimation and removal as near nadir-looking altimeters.

The baseline error consists of components in the along-track, perpendicular, and line of sight directions. The first two are in the order of mm, while the third has a slope in range that is significant for relative SSH estimation. We calculate the mean error in the line-of-sight direction for a resolution cell of $3\,\mathrm{km}$ by calculating the mean gradient of the error over all latitudes, except for the latitudes that the satellites cross, integrating it over the length of a resolution cell. Finally, the phase synchronization error shows an allocation of the error that a synchronization algorithm should achieve to ensure centimetric accuracy of the SSH estimate. The systematic errors and the oceanic and atmospheric biases are analyzed in sections 2.4 and 2.5 respectively.

2.3.5. Comparison With Single-platform Designs

One might wonder how a formation-flying cross-track interferometer compares to a single-platform interferometer. Recently the Surface Water and Ocean Topography (SWOT) mission has been successfully launched with the aim of providing accurate measurements of SSH at the submesoscales. SWOT is the current state-of-the-art single-platform ocean altimeter, so it serves as a benchmark for an alternative concept such as the formation-flying XTI.

Under most conditions, SWOT will achieve higher accuracy when estimating SSH. Harmony will provide similar accuracy at high, above $10\,\mathrm{m\,s^{-1}}$, wind speeds. At medium-to-high incidence angles, the dominant scattering mechanism over the ocean is Bragg scattering, which increases with surface roughness. Thus, scattering and by extension, accuracy increases with wind speed, while nadir and side-looking swath altimeters with small incidence angles lose accuracy with wind speed because scattering is primarily specular. Furthermore, side-looking interferometers have larger swaths.

The design of Harmony had to fit in the constraints imposed by using an existing SAR satellite as an illuminator. As such, the squint of the companions is determined by the beam of the illuminator and cannot be freely optimized to reduce the effective along-track baseline throughout the swath. A quasi-monostatic interferometer would not have this constraint and achieves better performance that is comparable to SWOT. Furthermore, the benefit of a formation-flying interferometer is that the formation can be reconfigured in flight to serve the needs of different applications, such as land topography and surface current estimation.

2.4. Systematic Errors

This section provides an analysis of the systematic errors in a formation-flying interferometer. The focus is on identifying and accounting for the main bias contributions to the height estimate rather than on detailed modeling of the biases. We discuss the baseline errors and the phase synchronization error.

Table 2.3.: Error breakdown.

Error component	Mean value /cm	
	$U = 5\,\mathrm{m\,s^{-1}}$	$U = 15\,\mathrm{m\,s^{-1}}$
Instrument random error	4.2	1.6
Troposphere	0.3	0.3
Baseline	2.2	2.2
Phase synchronization	1.0	1.0

2.4.1. Baseline Error

The interferometric model presented in section 2.2.2 uses the cross and along-track baselines to estimate the standard deviation of the sea surface height estimate. The model assumes knowledge of the physical separation of the formation elements, which requires knowledge of the position of the companions. Error-free position information is not possible, and errors in the baseline estimation of the companions will introduce systematic errors in the height measurement.

From sections 2.2.1 and 2.2.1 we know that due to the squinted line of sight of the two SAR satellites, the along-track baseline is a function of the along-track and normal separation of the companions. The perpendicular baseline is a function of the radial and normal components of the separation vector. As a result, an error in the normal component of the separation leads to an error in both the along-track and perpendicular baselines. A systematic error in the knowledge of the effective along-track baseline would result in a bias of the ATI phase estimate. Following (2.23), an error in the effective along-track baseline, ϵ_{ATI}, leads to a bias of the relative height estimate

$$\epsilon_h = \frac{h_a \epsilon_{\mathrm{ATI}}}{2\pi B_{\parallel}} \hat{\phi}_{\mathrm{ATI}}. \tag{2.25}$$

Substituting the relation between interferometric phase and radial velocity into the equation gives

$$\epsilon_h = h_a \frac{\epsilon_{\mathrm{ATI}}}{B_{\parallel}} \frac{\tau_s \sin\theta_i}{\lambda} v_r, \tag{2.26}$$

where τ_s is the time lag due to the on-board along-track baseline and v_r is the relative radial velocity of the surface with respect to the receiver. Therefore, with a height of ambiguity of $60\,\mathrm{m}$, which is typical for the formations presented in this chapter, an error in the knowledge of the effective along-track baseline of $1\,\mathrm{mm}$ translates to a height bias of $\pm 0.10\,\mathrm{mm}$ for a radial velocity of $1\,\mathrm{m\,s^{-1}}$.

Moving on to the perpendicular baseline error ϵ_{B_X}. Given that the height sensitivity is inversely proportional to the perpendicular baseline, the error is [23]

$$\epsilon_h = h \frac{\epsilon_{B_X}}{B_{\perp}}, \tag{2.27}$$

where h is the surface height. For a surface height of $h = 1\,\mathrm{m}$ and an effective perpendicular baseline of $B_\perp = 300\,\mathrm{m}$, a baseline error of $\epsilon_{B_X} = 1\,\mathrm{m}$ will lead to a height error of $\epsilon_h = \pm 3.3\,\mathrm{mm}$.

An error in the position of the receiver along the line of sight direction leads to an over or underestimation of the interferometric phase, resulting in a vertical displacement of the digital elevation model produced by the interferometer [23]

$$\epsilon_h = \frac{h_a}{\lambda}\epsilon_{B_l}. \tag{2.28}$$

As the height of ambiguity varies with look angle, ϵ_h due to an error along the line of sight changes with range. Equation (2.28) gives the error locally at a given range. Since the interferometric height estimate is a measure of the relative height of the surface, the slope of error is more important than the bias of the absolute value. Taking the largest value of h_a for the optimized formation and dividing the difference of h_a between the near and far range with the swath width gives a slope of $0.89\,\mathrm{cm}$ per kilometer of ground range for a $1\,\mathrm{mm}$ error in along the line of sight direction. This will produce a ramp in the height estimate that needs to be accounted for.

2.4.2. Phase Synchronization Error

Bistatic radars have, by definition, separate transmitters and receivers. Each transmitter and receiver has its own modulator/demodulator and its own oscillator. The low-frequency phase errors introduced in the signal by the transmit oscillator are independent from those of the receive oscillator and do not completely cancel out when the receiver demodulates the signal. After demodulation, the signal has a residual phase error due to the mismatch of the transmit and receive oscillator phases. The error defocuses the images produced by the SAR and produces a low-frequency modulation in azimuth in the digital elevation models. The issue applies both when two receivers operate bistatically, such as Harmony, and when one of the two instruments operate bistatically, such as the case discussed in Section 2.3.2.

High-resolution measurement of the ocean surface topography requires synchronizing the receiver oscillators. A model of the synchronization error is out of the chapter's scope. Instead, we focus on setting the requirement of relative phase error appropriate for SSH estimation. To maintain centimetric accuracy, we set the maximum error due to the clock to $1\,\mathrm{cm}$. This translates to 0.175° of phase error for the height of ambiguity of the optimized formation.

A potential solution is the precise orbit determination (POD)-global navigation satellite system (GNSS) scheme presented in [39]. The scheme uses a common reference oscillator for the GNSS receiver and the SAR instrument, making the residual phase error proportional to the GNSS error of the two satellites. Thus, we scale the phase error by $f_l/(\sqrt{2}f_c)$ to convert it to a synchronization error, where f_c is the radar carrier frequency and f_l is the carrier frequency of the navigation signal. For a radar carrier of $f_c = 5.405\,\mathrm{GHz}$ and a navigation carrier of $f_l = 1.5\,\mathrm{GHz}$ the synchronization error is 0.045°.

Alternatively, the error can be remedied in post-processing by a band-stop filter. The error affects the signal in azimuth because of the stability of the oscillator over shorter time scales. Thus, a band-stop filter with a stopband in azimuth covering the affected wavenumbers can mitigate the effect of the error at the cost of losing information over the stopband.

2.5. Oceanic and Atmospheric Biases

2.5.1. Tropospheric Path Delay

The tropospheric delay causes range geolocation errors in SAR images due to an overestimation of the distance between the instrument and the surface along the line of sight. Estimates of the tropospheric delay at the time of acquisition either from models or from radiometers can be used to correct for this range shift. The troposphere also affects interferometric height estimates of single-pass interferometers, such as the one discussed in this chapter. The two SAR instruments of the interferometer image the surface with a different incidence angle. Hence, the paths from a given scatterer to each sensor undergo different tropospheric delays, leading to a residual interferometric phase in the interferogram.

The shift in the interferometric phase leads to a shift in the height estimate. The error in the height estimate is proportional to the product of the tropospheric delay with the tangent of the incidence angle. The variation of the error due to the troposphere is [40]

$$\epsilon_{\mathrm{TPD}} = \left\| \delta_z (\tan^2 \theta_i - 1) \right\|, \tag{2.29}$$

where δ_z is the nadir tropospheric path delay. The error decreases with incidence angle and reaches $0\,\mathrm{cm}$ at $45°$. The dry and wet delay sum to $2.1\,\mathrm{m}$ to $2.5\,\mathrm{m}$ depending on atmospheric conditions. Without correction, this error would be too large for ocean topography estimation.

Numerical weather models, such as ERA5 from the European Center for Medium-Range Weather Forecasts (ECMWF), provide estimates of the tropospheric path delay. Using such models, we can estimate the value of ϵ_{TPD} and correct for it in our estimate of the SSH. After correction, the error becomes the residual between the estimate of the nadir path delay from the model and the true value. Vieira et al. have found that the RMS error between the wet tropospheric delay and the delay measured from radiometers varies from $0.6\,\mathrm{cm}$ to $1.7\,\mathrm{cm}$ [38], depending on latitude. Taking an average value of $1.15\,\mathrm{cm}$ for the residual in the nadir direction and substituting it in (2.29) in place of δ_z provides an estimate of the error after correction. The error decreases from $0.6\,\mathrm{cm}$ at near range to $0\,\mathrm{cm}$ at $45°$ and increases to $0.4\,\mathrm{cm}$ from $45°$ to the far range. Since ϵ_{TPD} varies with incidence angle, its power spectral density will have a component in the wavenumbers that correspond to the submesoscales and the error has to be taken into account in the error budget of the interferometer.

2.5.2. Sea-state Bias

Relative height estimates are obtained from two or more SAR images using the method of interferometry. The modulus of the interferogram is proportional to the normalized radar cross-section. The most commonly used estimator for the relative height in SAR interferometry is the maximum-likelihood estimator, which uses speckled averaged interferometric phase to estimate the relative height. The bias of an estimator is defined as the distance between the expected value of the estimator and the true value of the estimated quantity. If the NRCS is a function of height, then the expected value of the estimator will include a term proportional to the correlation of the NRCS with the surface height which will bias the expectation away from the true value of the height.

In the case of the ocean, the waves on the surface have a difference in roughness between crests and troughs. This leads to more scattering of the SAR signal coming from the crests than the troughs [41], correlating the NRCS with the surface height. The roughness of the ocean surface depends on the wind speed and other parameters related to the state of the sea, giving the name "sea-state bias" to this phenomenon [42]. In this section we present a summary of the effect and the main findings as they relate to bistatic SAR cross-track interferometers. A detailed derivation is included in the appendix.

The height estimated by an interferometer $\hat{h}(x)$ after the formation of an interferogram averaging over independent speckle realizations is given by the convolution of the product of the NRCS $\sigma_0(x)$ and sea surface height $z(x)$ with the square of the instrument response function $\chi(x)$. For simplicity, we will consider only one dimension, so the height estimate is

$$\hat{h}(x) \approx A\frac{1}{\bar{\sigma_0}(x)}(\sigma_0 z * \|\chi\|^2)(x), \tag{2.30}$$

where $\bar{\sigma_0}(x) = (\sigma_0 * \|\chi\|^2)(x)$ and A is a term that includes the antenna gain and constants of proportionality. From this point on, the height estimate is computed for a region around x_0, and the spatial variability of the instrument-response averaged cross-section is assumed to be negligible in this region $\bar{\sigma_0}(x) = \bar{\sigma}$. Additionally, we express $\sigma(x)$ in terms of the average cross-section $\bar{\sigma}$ and a spatially varying component $\delta\sigma(x)$

$$\sigma(x) = \bar{\sigma}(1 + \delta\sigma(x)).$$

Applying this relation to (2.30) yields

$$\hat{h}(x) \approx A((1 + \delta\sigma)z * \|\chi\|^2)(x). \tag{2.31}$$

The bias of the estimator is evaluated by computing its expected value over the ensemble of the waves

$$\mathbb{E}_w[\hat{h}(x)] \approx A(\mathbb{E}_w[z(x)] + \mathbb{E}_w[\delta\sigma(x)z(x)]) * \|\chi(x)\|^2. \tag{2.32}$$

Equation (2.32) demonstrates that the estimator is biased away from the true value of the surface height $z(x)$ because of the second term that arises due to the cross-correlation of the spatial variation of the NRCS with the height. The estimator will

be unbiased only in cases where the cross-correlation $\mathbb{E}[\delta\sigma(x)z(x)]$ is 0. According to the linear modulation theory of Hasselmann and Hasselmann [43], the spatial variation of the NRCS $\tilde{\delta\sigma}(k)$ is related to the surface wave amplitude $Z(k)$ via a modulation transfer function (MTF) $T(k)$ in the angular wavenumber domain

$$\tilde{\delta\sigma}(k) = T(k)Z(k). \tag{2.33}$$

Substituting (2.33) into (2.32) in terms of the inverse Fourier transform of $\tilde{\delta\sigma}(k)$ leads to the following expression for the bias

$$\mathrm{Bias}(\hat{h}, z) = \int T(k)\Psi(k)\,\mathrm{d}k \int \|\chi(x)\|^2\,\mathrm{d}x, \tag{2.34}$$

where $\mathbb{E}[Z(k)Z(k')] := \Psi(k)\delta(k-k')$ is the surface elevation variance spectrum [43]. In cases where the squared instrument response function is normalized, the integral of $\|\chi(x)\|^2$ with respect to x integrates to unity, and the bias is determined by the integral of the modulation transfer function and the surface elevation variance spectrum.

Integrating over all numbers in $\mathbb{R}^2$ is not of interest as we only expect to come across waves with maximum wavelengths of $250\,\mathrm{m}$. Computations of (A.19) using the Elfouhaily spectrum [44] for Ψ and the MTF defined by Schulz-Stellenfleth et al [45] for T were carried out using a dimensionless fetch of 100×10^3. The bias of the height estimate due to the sea-state is shown in Figure 2.21 as a function of wind speed for wind azimuths of $0°$, $45°$ and $90°$, using a solid black line, a dashed red line, and a dotted blue line respectively. The bias is much stronger for winds aligned with the radar look direction than for crosswinds and increases approximately linearly with wind speed between $5\,\mathrm{m\,s^{-1}}$ to $10\,\mathrm{m\,s^{-1}}$ for all wind directions.

Quantitatively, the bias varies between $1.5\,\mathrm{cm}$ to $12.5\,\mathrm{cm}$ which is significant when compared to the standard deviation of the total random error of the height shown in Figure 2.16. Nevertheless, the interferometric height estimate is relative; therefore, a systematic bias that is independent of ground range and azimuth will not impact the accuracy of the relative values as long as the bias does not cause the interferometric phase to wrap over 2π. Given that the formations discussed have a minimum height of ambiguity of $30\,\mathrm{m}$, biases of up to $12.5\,\mathrm{cm}$ are unlikely to cause phase wrapping.

2.6. Conclusion

We have presented a model to estimate the random and systematic errors in the ocean elevation measurement of a bistatic SAR interferometer with a squinted line of sight. Two case studies were used to investigate the performance of the concept: the Harmony mission in its cross-track interferometry phase, and a pair of SAR satellites flying in close formation with one acting as a transmitter and receiver and the other bistatically. The discussion has included the impact of coherence losses due to noise, volume scattering, and temporal lag between acquisitions. We investigated the simulated performance of the two systems over an

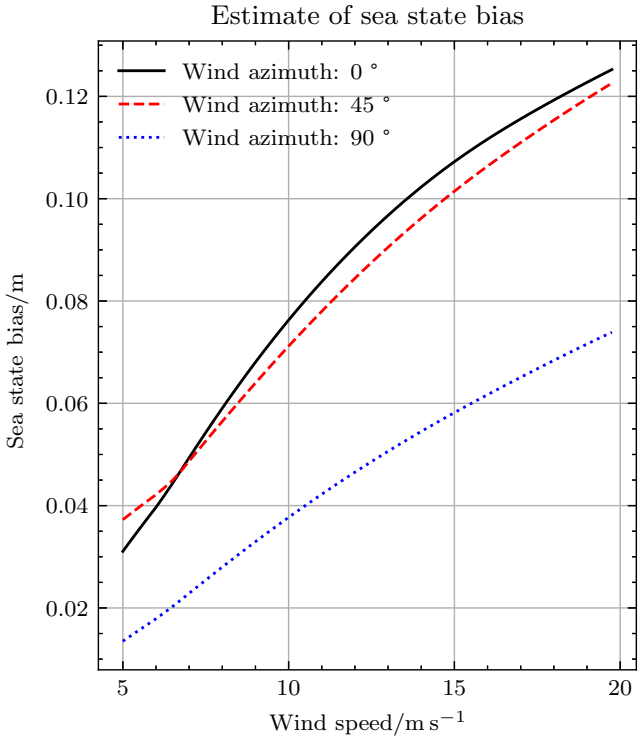

Figure 2.21.: Bias of the height estimate as a function of wind speed for azimuth directions of 0, 45 and 90 degrees.

orbit and the challenges involved in the estimation of relative heights from SAR images of the sea surface. The key benefit of the XTI operation of a closed formation with a squinted line of sight is allowing for effective perpendicular baselines that are sufficiently large to observe the ocean surface with sub-meter accuracy while minimizing the temporal decorrelation without compromising the safety of the formation. Minimizing the temporal delay reduces the temporal decorrelation sufficiently to allow estimation of the relative SSH.

In the case of Harmony, the squinted line of sight is a result of the bistatic operation. The beams of the companions follow that of Sentinel-1, resulting in an off-boresight line of sight at the receivers. However, bistatic operation with an illuminator that is several kilometers displaced along the orbital track is not required; the same effect can be achieved using one monostatic and one bistatic SAR system with a squinted line of sight. The performance of the interferometer can be enhanced by taking advantage of the two on-board phase centers of the receivers to estimate the contribution of the relative surface motion to the interferometric phase and remove it. The results show a standard error of $1\,\mathrm{cm}$ to $8\,\mathrm{cm}$ over the en-

tire swath for optimized formation parameters at a wind speed of $5\,\mathrm{m\,s^{-1}}$, except for towards the poles. This corresponds to spatial scales of $38.7\,\mathrm{km}$ and $36.4\,\mathrm{km}$ for spectral slopes of $-\frac{11}{3}$ and -1.56 respectively. The performance improves at higher wind speeds due to more backscattering. With a wind speed of $10\,\mathrm{m\,s^{-1}}$, wavelengths of approximately $26\,\mathrm{km}$ and $11\,\mathrm{km}$ can be resolved.

In the case of the quasi-monostatic system, the constraint to align the beam of the two SARs in the Helix formation with the beam of an illuminator that is several kilometers ahead along the track is lifted. Thus, the squint of the line of sight is not range dependent as in the case of Harmony, and can be optimized for the entire swath at all latitudes. The performance combined with the wide swath of a SAR enables the recovery of submesoscale ocean features at high wind speeds. The results of the quasi-monostatic system show a standard error of less than $5\,\mathrm{cm}$ for the entire swath with the performance degrading only near the crossing point of the formation. The error translates to resolving scales of approximately $22\,\mathrm{km}$ for $5\,\mathrm{m\,s^{-1}}$ wind and $12\,\mathrm{km}$ for $15\,\mathrm{m\,s^{-1}}$ wind speed for the steeper spectrum.

The estimate of the sea surface height will be impacted by systematic errors. We have considered the main sources of systematic errors including phase synchronization, baseline estimation, and electromagnetic modulation of the backscattered signal. The phase synchronization error has a significant impact on the estimation. Therefore, cross-track interferometers must be designed with this potential limitation in mind. Alternatively, given that the error has a known shape in the wavenumber domain, band limited in the azimuth direction and negligible in the range direction, it could be removed from the signal using a filter. A detailed derivation of the sea-state bias for both a frozen and a dynamic surface has been presented for a bistatic interferometer. In particular, we have shown that the time dependence of the backscattering does not affect the sea-state bias under the assumption of a sufficiently broad SAR processing bandwidth and that the bias is a function of the hydrodynamic modulation and the surface height variance spectrum.

In the future we would like to complete the model by providing spectral envelopes for the systematic errors and biases. Furthermore, a more complete characterization of the phase synchronization error, and mitigation algorithms are needed. Finally, we would like to use the model to compute the azimuth cutoff wavenumber at different latitudes, incidence angles, and wind speeds.

Acknowledgment

The authors would like to thank Prof.ir. Peter Hoogeboom for his constructive feedback during the preparation of the manuscript.

3

On the Sensitivity to Height and Motion of Bistatic SAR Interferometry

A Spectral View

Assessing the performance of interferometers and processing interferograms require accurate knowledge of the temporal lag, sensitivity, and spectral shift. While these parameters are well-defined for conventional interferometric configurations, their definition becomes opaque for complex configurations, such as bistatic systems with formation-flying satellites. According to the principle of diffraction tomography, each instrument samples a distinct region of the scattering surface's Fourier domain. Using this principle, we introduce a wavenumber-domain method for calculating the temporal lag, spectral shift, and sensitivity to height of synthetic-aperture radar (SAR) interferometers. The method calculates interferometric parameters by aligning the ground-projected wavenumber support of the SAR images forming the interferogram. Although the wavenumber-support method agrees with the conventional geometric formulations of the temporal lag and sensitivity in geometrically simple cases, the two methods diverge in more complex geometries. We show that when the two SAR satellites fly in a close-formation or have lines of sight that are squinted with respect to the zero-Doppler direction, then the geometric formulations are inadequate and the wavenumber-support method is needed to accurately estimate the interferometric parameters.

This chapter has been published as A. Theodosiou and P. López-Dekker. 'On the Sensitivity to Height and Motion of Bistatic SAR Interferometry: A Spectral View'. In: *IEEE Transactions on Geoscience and Remote Sensing* 62 (2024), pp. 1–12

3.1. Introduction

WHAT is the temporal lag and the height sensitivity of a synthetic-aperture radar (SAR) interferometer? Scientists familiar with the instrument would consider the answer obvious. When the instrument look direction is perpendicular to the flight direction, these two parameters are proportional to the projections of the antennas' physical separation in the relevant directions. For example, an along-track interferometer (ATI) with two antennas on a single platform has a temporal lag directly proportional to the along-track separation [47–49]. Similarly, a cross-track interferometer (XTI) with sensors that are only separated in the plane normal to the flight direction has a sensitivity proportional to the baseline of the two antennas perpendicular to the line of sight [50, 51].

The link between interferometric parameters, namely height sensitivity and temporal lag, and geometric parameters stems from a geometric approach to interferometry. The geometric approach relates the phase of an interferogram to, in the case of XTI, the elevation of the surface, and in the case of ATI to the radial motion of the surface. This approach hinges on the assumption that the SAR signal is monochromatic. In other words, it assumes that the signal bandwidth in range and azimuth is small enough to be considered negligible. The monochromatic assumption hides the role that the ground reflectivity spectrum plays in interferometry. Gatelli explained the implications of considering the ground-range wavenumber shift for a conventional XTI[30]. One that has separation only perpendicular to the line of sight. This has led to the introduction of spectral shift filtering in the processing of interferograms [30, 52, 53].

Nevertheless, the monochromatic approach remains the primary view of interferometry, if for no other reason than being intuitive. The approach and consequently the geometric methods of calculating interferometric parameters, while intuitive, break down in more complex geometries. Consider an interferometer operating bistatically with a squinted line of sight, e.g. a system similar to TanDEM-X [23] or Harmony [21]. The time taken for the lagging phase center to *see* a given point on the surface with the same viewing geometry as the leading phase center is not a function of the along-track separation alone. Hence, the temporal lag is not equal to half the tangential separation of the phase centers, as is the case for bistatic interferometers with a line of sight perpendicular to the flight direction.

Likewise, since the bistatic lines of sight do not share a common radial-normal plane, they first need to be aligned before calculating the perpendicular baseline, which drives the geometric expression of the sensitivity. However, the lines of sight of the two sensors do not necessarily align during the illumination time of a given point, since the transmitter-receiver pairs have a bistatic line of sight with a common ending point but different starting points and different directions. Thus, applying the geometric method is not possible.

Employing the monostatic equivalent (ME) of each transmitter-receiver pair [22] provides a workaround to this problem and allows one to geometrically compute the interferometric baselines. Nevertheless, the location of the monostatic equivalent of a system that has a three-dimensional separation and squinted line of sight becomes complicated. A different monostatic equivalent exists for each com-

bination of slow time and look angle, as Figure 3.1 shows.

In this chapter, we present a more accurate method to solving this problem. The fundamental relation of diffraction tomography states that the field scattered by an object is directly proportional to the object function's Fourier transform at the wavenumbers that correspond to the incident and scattered wave vectors. Building on this idea, we propose using the wavenumber support of the two SAR images to calculate these interferometric parameters. In the following sections, we show that by finding the temporal and spectral shifts that align the wavenumber supports of the two sensors, we can calculate the temporal lag and the interferometer sensitivity. Our technique applies to all interferometers, monostatic and bistatic, with temporally varying or fixed separations, and regardless of squint.

3.2. A Spectral Approach to SAR Interferometry

3.2.1. The Fundamental Relation of Diffraction Tomography

Before delving into interferometry, we will first motivate our wavenumber-domain approach by linking the fundamental principle of diffraction tomography to the region of support, i.e. the subset of the image domain that maps to non-zero values, of a SAR image. Consider an instrument illuminating an object, with complex reflectivity $o(\mathbf{r_s})$ where $\mathbf{r_s}$ represents the position vector, with a monochromatic electromagnetic wave. A second instrument receives the scattered electromagnetic wave. Assuming that the object is homogeneous, that the Born approximation is valid, and neglecting geometric attenuation, the received field is [54]

$$u(\mathbf{r_T}, \mathbf{r_R}) = \iiint_V o(\mathbf{r'_s}) \mathrm{e}^{-\mathrm{j}k_0(R_T(\mathbf{r_T},\mathbf{r'_s})+R_R(\mathbf{r_R},\mathbf{r'_s}))}\, \mathrm{d}\mathbf{r'_s}, \tag{3.1}$$

where $\mathbf{r_T}, \mathbf{r_R}$ are the positions of the transmitter and receiver respectively, R_T, R_R are the distances to the object from the transmitter and receiver, respectively, and the integration is taken over the volume of the object.

We now consider a small neighborhood around the object at $\mathbf{r_0}$ and carry out the first-order Taylor expansion of the distances for a given position of the transmitter and receiver. The expansion yields the well-known plane wave approximation of spherical waves

$$R_n(\mathbf{r_n}, \mathbf{r_s}) \approx R_n(\mathbf{r_0}) + \nabla R_n(\mathbf{r_0}) \cdot (\mathbf{r_s} - \mathbf{r_0}), \tag{3.2}$$

where the subscript n can be either T or R. ∇R_n is the gradient of the slant range and since R_n represents the distance along a spherical wave, the gradient points in the line of sight direction. For a typical SAR satellite in a low-Earth orbit, such as Sentinel-1, with altitude $693\,\mathrm{km}$, a look angle of $26°$, assuming a rectilinear geometry, and setting $\mathbf{r_s} = (10\,\mathrm{m}, 2.5\,\mathrm{m}, 0\,\mathrm{m})^T$ to correspond to half a resolution cell, the relative error between the expansion in (3.2) and the true slant range is $8.8 \times 10^{-9}\,\%$. Hence, from this point on, we proceed with our analysis using the plane wave approximation.

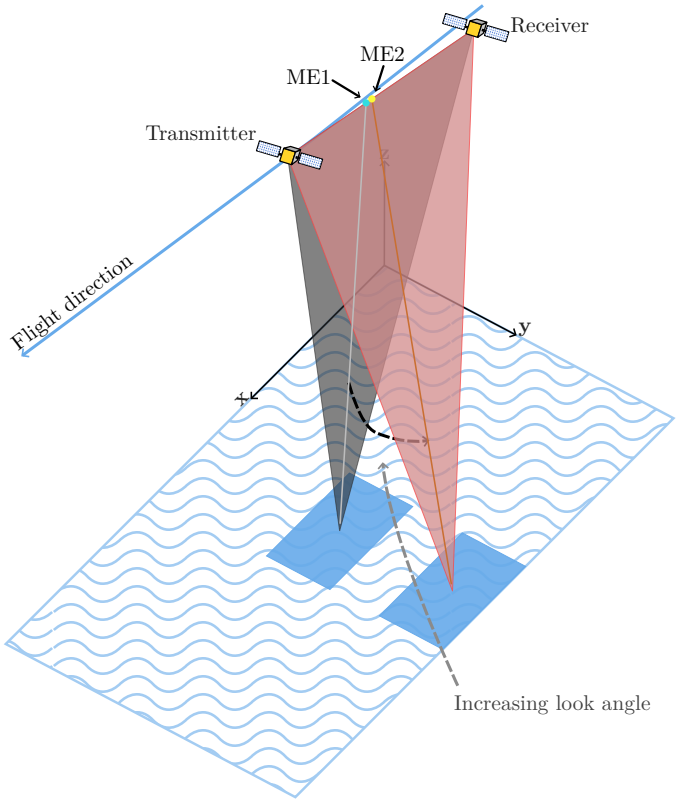

Figure 3.1.: The locations of the monostatic equivalents for a given slow time and two different look angles. As the look angle increases, the location of the monostatic equivalent shifts along the line segment connecting the transmitter to the receiver. Thus, the monostatic equivalent system does not have a single location for a given slow time, as a true monostatic system would.

Substituting (3.2) into (3.1), and moving the constant phase terms out of the integral, we note that the volume integral becomes the three-dimensional Fourier transform of the scattering density $\tilde{o}$ [55]:

$$u(\mathbf{r_T}, \mathbf{r_R}) \approx \tilde{o}(\mathbf{k_T} + \mathbf{k_R}) \tag{3.3}$$

where $\mathbf{k_T} = k_0 \nabla R_T(\mathbf{r_0})$ and $\mathbf{k_R} = k_0 \nabla R_R(\mathbf{r_0})$ are the transmitter and receiver wave vectors respectively, and we have neglected the leading phase term. This is the fundamental principle of diffraction tomography [55, 56]. Equation (3.3) states that the received field is proportional to the Fourier transform of the illuminated object at the components of the total wave vector, $\mathbf{k_T}+\mathbf{k_R}$. The result demonstrates that the instrument samples the Fourier space of the object's reflectivity at

one point in the spatial frequency domain [57]. The line of sight of the instrument and the carrier wavelength determine the point in the spatial frequency domain at which the object is sampled. By varying the viewing geometry, for example, moving the location of the transmitter and receiver or changing the look and squint angles of the antennas, the instrument can sample different points of the Fourier domain.

A SAR samples the scattered electromagnetic field with a certain impulse response. Thus, the signal of the SAR image becomes[50]

$$u(x,\eta) = \mathrm{e}^{-\mathrm{j}k_0 R_0}(f * \chi)(x,\eta), \tag{3.4}$$

where $*$ denotes the linear two-dimensional convolution, $R_0 = R_T(\mathbf{r_0}) + R_R(\mathbf{r_0})$, and we have used the range coordinate, η, and the azimuth coordinate, x, as the image coordinates, and the elevation, ζ, which is perpendicular to both as the third axis. In this expression, we have assumed that setting the azimuth position sets the positions of the receiver and transmitter. $\chi(x,\eta)$ is the system impulse response, and we have defined the following symbol for brevity:

$$f(x,\eta) = \mathrm{e}^{-\mathrm{j}\mathbf{k}\cdot\mathbf{r_s}} \int_Z o(\mathbf{r_s})\,\mathrm{d}\zeta. \tag{3.5}$$

The plane wave exponential has been moved out of the integral because any component of $\mathbf{r_s}$ along the elevation direction will, by definition, be perpendicular to the wave vector. Additionally, the system impulse response does not depend on the elevation, since it is perpendicular to the plane of the SAR image. Consequently, the integral with respect to elevation only contains the object's reflectivity. It represents the projection of the scattering object onto the range and azimuth axes. Thus, each sample in a SAR image is a single tomographic projection of the scattering object, shifted by the plane wave exponential and filtered by the instrument's impulse response [50].

SARs do not transmit and receive monochromatic waves. On the contrary, they use chirp waveforms that have a certain bandwidth. Therefore, with each pulse, the radar samples the Fourier domain of the object along the line $k_0(f_r)(\nabla R_T(\mathbf{r_0}) + \nabla R_R(\mathbf{r_0}))$, where $k_0(f_r)$ is the instantaneous wavenumber that corresponds to the frequency f_r of the chirp signal. Acquiring a second SAR image, from a different position, produces a different tomographic projection of the scattering object. Cross-track interferometry uses these two different projections of the scattering object to infer the relative height of the scatterer.

3.2.2. A Mathematical Derivation of the Spectral Shift in Two Dimensions

The fundamental principle of the method discussed in this chapter is that only the energy that comes from the wavenumbers that coincide between the two images contributes to the interferometric signal. In cases where the wavenumber supports of the two images are disjoint, the interferometric signal drops to zero. Therefore, forming an interferogram aligns the wavenumber supports of the two

images, and the temporal lag and wavenumber shifts correspond to the moment in time and shift in frequency where the wavenumber supports of the two images are aligned. Prati and Rocca first proved this in [53] for the range wavenumbers and for an interferometer that has only a perpendicular separation. Gatelli et al. [30] expanded on the spectral shift due to different look angles and on its exploitation for the improvement of interferometric techniques. The idea that only the overlapping parts of the spectra in two dimensions, in range and azimuth, contribute to interferometric information has also been used in [58] to correct for the large angle between acquisitions coming from satellites that followed crossing orbits. In this section we provide a derivation of this principle in two dimensions, range and azimuth, for a bistatic interferometer with an arbitrary separation between the two SARs that compose it.

Consider a cross-track interferometer where two bistatic SARs illuminate a region on the surface as shown in Figure 3.2. The first pair of instruments illuminate the surface with look angles $\theta_{1_T}, \theta_{1_R}$ and squints ψ_{1_T}, ψ_{1_R}, while the second pair has look angles $\theta_{2_T}, \theta_{2_R}$ and squints ψ_{2_T}, ψ_{2_R}, where subscripts T and R refer to transmitter and receiver respectively. The azimuth direction is x and the ground range direction is y; the two-way slant range to the center of the resolution cell is R_0. The signal representing the processed image of the ith SAR for $i \in \{1, 2\}$ is

$$u_i(x, y) = \mathrm{e}^{-\mathrm{j}k_0 R_0}(f_i * \chi)(x, y), \tag{3.6}$$

where $\chi(x, y)$ denotes the system impulse response in terms of azimuth and ground range. We introduce the following symbols in the interest of brevity:

$$f_i(x, y) = s(x, y)\mathrm{e}^{-\mathrm{j}\mathbf{k_i}\cdot\mathbf{r_s}}, \tag{3.7}$$
$$\mathbf{r_s} = (x, y, z(x, y))^T, \tag{3.8}$$
$$\mathbf{k_{i_T}} = k_0(\sin\psi_{i_T}, \cos\psi_{i_T}\sin\theta_{i_T}, -\cos\psi_{i_T}\cos\theta_{i_T})^T, \tag{3.9}$$
$$\mathbf{k_{i_R}} = k_0(\sin\psi_{i_R}, \cos\psi_{i_R}\sin\theta_{i_R}, -\cos\psi_{i_R}\cos\theta_{i_R})^T, \tag{3.10}$$
$$\mathbf{k_i} = \mathbf{k_{i_T}} + \mathbf{k_{i_R}}, \tag{3.11}$$

where $\mathbf{k_i}$ is the ith bistatic wave vector, and we have assumed that the surface scattering described by the reflectivity $s(x, y)$ is coming from the surface described by $z(x, y)$. The carrier wavenumber, $k_0 = 2\pi/\lambda_0$, depends on the carrier wavelength λ_0 of the instrument, which we assume is common between the two sensors. The wave vectors $\mathbf{k_{i_T}}$ and $\mathbf{k_{i_R}}$ are equivalent to those in Section 3.2.1, but here we have defined them in terms of the look and squint angles of the instruments instead of the gradients of the slant ranges. In monostatic operation, the wave vector $\mathbf{k_i}$ reduces to $2\mathbf{k_{i_T}}$, and the modulus is two times the carrier wavenumber. The modulus of the bistatic wave vector is smaller than $2k_0$.

We express a single realization of an interferogram as

$$V(x, y) = u_1(x, y)u_2(x, y)^*. \tag{3.12}$$

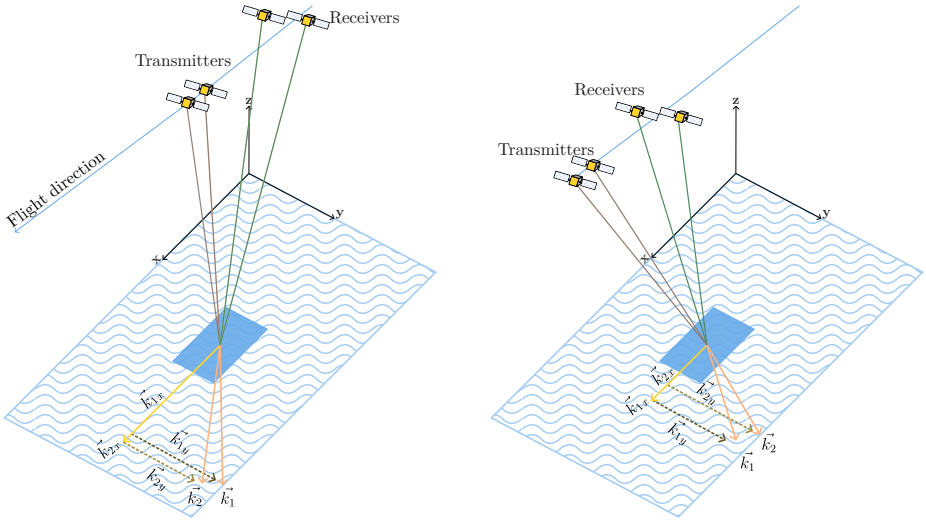

(a) The beginning of an acquisition.

(b) The end of an acquisition.

Figure 3.2.: An illustration of the two SAR instruments sampling ground-projected range and azimuth wavenumbers of a given resolution cell. $\mathbf{k_i}$ is the surface-projected wavenumber vector that the ith instrument samples.

The Fourier transform of the interferogram is

$$\begin{aligned}\tilde{V}(k_x', k_y') &= \mathcal{F}\{u_1(x,y)u_2(x,y)^*\}(k_x, k_y),\\ &= (\tilde{u}_1 \star \tilde{u}_2)(k_x, k_y),\\ &= \iint \tilde{u}_1(k_x, k_y)^* \tilde{u}_2(k_x + k_x', k_y + k_y')\,\mathrm{d}k_x\,\mathrm{d}k_y,\end{aligned} \tag{3.13}$$

where $\star$ denotes the cross-correlation operation and the Fourier transform of the image (3.6) is given by

$$\tilde{u}_i(k_x, k_y) = \tilde{f}_i(k_x, k_y)\tilde{\chi}(k_x, k_y). \tag{3.14}$$

Assuming that the vertical component of $\mathbf{r_s}$ is constant with x and y allows us to express the Fourier transform of the image as the shifted reflectivity filtered by the instrument frequency response in the wavenumber domain

$$\tilde{u}_i(k_x, k_y) = \tilde{s}(k_x + \mathbf{k_i}_x, k_y + \mathbf{k_i}_y)\mathrm{e}^{-\mathrm{j}\mathbf{k_i}_z z}\tilde{\chi}(k_x, k_y), \tag{3.15}$$

where the notation $\mathbf{k_i}_j$ denotes the jth component of wave vector $\mathbf{k_i}$ and $j \in \{x, y, z\}$. Equation (3.15) states that each sensor samples the surface reflectivity across a

band of range and azimuth wavenumbers. Since the surface reflectivity is not band-limited, the bandwidth of the image is determined by the system frequency response. Each ground-range and azimuth wavenumber at which the sensor samples the reflectivity is shifted by $\mathbf{k_{i}}_y$ and $\mathbf{k_{i}}_x$ respectively. Thus, each instrument captures a different wavenumber band of the surface reflectivity. The band that each instrument captures depends on the wave vector of the instrument.

Substituting (3.15) into (3.13) yields the linear cross-correlation of the two image spectra

$$\tilde{V}(k_x, k_y) = \iint \tilde{s}(k_x' + \mathbf{k_1}_x, k_y' + \mathbf{k_1}_y)^* \tilde{s}(k_x' + \mathbf{k_2}_x + k_x, k_y' + \mathbf{k_2}_y + k_y) \\ \mathrm{e}^{\mathrm{j}\Delta\mathbf{k}_z z} \tilde{\chi}(k_x', k_y')^* \tilde{\chi}(k_x{}' + k_x, k_y' + k_y)\, \mathrm{d}k_x'\, \mathrm{d}k_y', \quad (3.16)$$

where $\Delta\mathbf{k}_z = \mathbf{k_1}_z - \mathbf{k_2}_z$ is the z component of the wave vector difference.

We assume that the surface reflectivity, $s(x, y)$, is a circular complex stochastic process. Thus, as shown in the Appendix, the Fourier transform of the surface reflectivity, $\tilde{s}(k_x, k_y)$, is uncorrelated

$$\mathbb{E}[\tilde{s}(k_x, k_y)\tilde{s}(\kappa_x, \kappa_y)^*] = \tilde{R}_s(k_x, k_y)\delta(k_x - \kappa_x, k_y - \kappa_y), \quad (3.17)$$

where $\tilde{R}_s(k_x, k_y)$ is the Fourier transform of the surface reflectivity's spatial correlation. For a wide-sense stationary process $\tilde{R}_s(k_x, k_y)$ is the power spectral density of the surface reflectivity, according to the Wiener-Khinchin theorem. The Dirac delta function in (3.17) represents an idealized case, which follows from the assumption that at the scales of interest, the autocorrelation length of the surface roughness is short. A practical surface can be modeled by replacing the Dirac delta with a finite-bandwidth function, such as a Gaussian kernel, to model the distribution of the power spectral density over a band of wavenumbers.

We are interested in the expected interferogram, so we take the expectation over the surface ensemble of (3.16) and apply (3.17)

$$\tilde{I}(k_x, k_y) = \iint \tilde{R}_s(k_x{}' + \mathbf{k_1}_x, k_y{}' + \mathbf{k_1}_y)\delta(k_x + \Delta\mathbf{k}_x, k_y + \Delta\mathbf{k}_y) \\ \mathrm{e}^{\mathrm{j}\Delta\mathbf{k}_z z} \tilde{\chi}(k_x{}', k_y{}')^* \tilde{\chi}(k_x{}' + k_x, k_y' + k_y)\, \mathrm{d}k_x'\, \mathrm{d}k_y', \quad (3.18)$$

where $\Delta\mathbf{k}_x = \mathbf{k_1}_x - \mathbf{k_2}_x$, and $\Delta\mathbf{k}_y = \mathbf{k_1}_y - \mathbf{k_2}_y$. The Dirac delta function is not a function of the integration variables, so we can move it out of the integral. We describe $\tilde{I}$ as the product of the delta function and the cross-correlation of the frequency response with itself filtered by the power spectral density of the surface reflectivity

$$\tilde{I}(k_x, k_y) = \delta(k_x + \Delta\mathbf{k}_x, k_y + \Delta\mathbf{k}_y)\mathrm{e}^{\mathrm{j}\Delta\mathbf{k}_z z}(\tilde{R}_s' X \star X)(k_x, k_y), \quad (3.19)$$

where $\tilde{R}_s'$ is the shifted Fourier transform of the spatial correlation of the surface reflectivity $\tilde{R}_s'(k_x, k_y) = \tilde{R}_s(k_x + \mathbf{k_1}_x, k_y + \mathbf{k_1}_y)$. Taking the inverse Fourier transform of (3.19) yields

$$\begin{aligned} I(x, y) &= \mathcal{F}^{-1}\{\tilde{I}(k_x, k_y)\}(x, y) \\ &= \mathrm{e}^{\mathrm{j}\Delta\mathbf{k}_z z}\tilde{K}(\Delta\mathbf{k}_x, \Delta\mathbf{k}_y)\mathrm{e}^{\mathrm{j}(\Delta\mathbf{k}_x x + \Delta\mathbf{k}_y y)}, \end{aligned} \quad (3.20)$$

where $\tilde{K}(k_x, k_y) = (\tilde{R}'_s\tilde{\chi} \star \tilde{\chi})(k_x, k_y)$. We can readily interpret (3.20). The expected interferogram is a complex sinusoid in the spatial domain, with phase proportional to the height of the surface. The amplitude is the wavenumber-domain cross-correlation of the product $\tilde{R}'_s\tilde{\chi}$ with the system frequency response, evaluated at the shift between the two images. The product $\tilde{R}'_s\tilde{\chi}$ is the frequency response of the system filtered by the shifted power spectral density of the reflectivity.

3.2.3. The Wavenumber Support

We express the wavenumber support of a SAR image as a function of slow time, t, and range frequency f_r. The wavenumbers forming the support of a resolution cell located at the transmitter look angle θ_l satisfy

$$\mathbf{k_i}(t, f_r; \theta_l) = k_0(f_r)(\hat{\mathbf{l}_{\mathbf{T_i}}}(t) + \hat{\mathbf{l}_{\mathbf{R_i}}}(t)), \tag{3.21}$$

where $k_0(f_r) = 2\pi f_r/c_0$ is the wavenumber magnitude, $\hat{\mathbf{l}_{\mathbf{T_i}}}$ is the unit vector in the direction of the transmitter's line of sight, and $\hat{\mathbf{l}_{\mathbf{R_i}}}$ is the unit vector in the direction of the receiver's line of sight. The line of sight of the ith sensor is

$$\hat{\mathbf{l}_{\mathbf{S_i}}}(t) = \frac{\mathbf{r_{S_i}}(t) - \mathbf{r_p}}{\|\mathbf{r_{S_i}}(t) - \mathbf{r_p}\|}, \tag{3.22}$$

where S is either T for the transmitter line of sight, or R for the receiver line of sight, and $\mathbf{r_p}$ is the position vector of the resolution cell. The time variable for a given resolution cell varies from $\tau_c - \tau_l/2$ to $\tau_c + \tau_l/2$, where τ_c is the beam center time and τ_l is the illumination duration. The range frequency is centered around the carrier frequency, f_c, and its bounds are given by the bandwidth of the transmitted pulse.

Equation (3.21) provides insight into the relationship between the signal space and the observation space. For a given resolution cell, slow time and range frequency parameterize the signal space, while in the observation space range and azimuth wavenumbers are the parameters. Assume the conventional viewing geometry of a monostatic SAR that is looking perpendicular to the azimuth direction. For a given slow time, the instrument samples the resolution cell with a band of frequencies determined by the transmitted pulse. The sampling of the resolution cell repeats every pulse repetition interval during the illumination time. The locus of slow time and range frequency that constitute the samples of the resolution cell are shown on the left panel of Figure 3.3a. The vertical extent of the region is the illumination time of the instrument, and the width is the pulse bandwidth.

The support of the signal in terms of slow time and range frequency maps to wavenumbers projected on the plane tangent to the surface at the resolution cell according to (3.21). The region of support of a resolution cell in terms of wavenumbers is shown in the right panel of Figure 3.3a. The diagram has been produced by exaggerating the illumination time to highlight the curvature of the region of support as time moves away from the beam center time.

We now move on to a bistatic case with a common transmitter. Assume that the transmitter maintains the same viewing geometry and transmits the same pulse as in the previous case. The receiver lags the transmitter along the same orbital plane. As a result, $\hat{\mathbf{l}}_{\mathbf{R}}$ is squinted forward with respect to $\hat{\mathbf{l}}_{\mathbf{T}}$. Since the transmitted pulse and the illumination time have not changed, the time-frequency support of the signal is the same as before. However, the different viewing geometry changes the mapping to the wavenumber domain. The squint of the bistatic line of sight means that for a fixed slow time, as the range frequency is sweeping, both the range and the azimuth wavenumbers are changing, as Figure 3.3b shows. Additionally, for a fixed range frequency the line of sight of the instrument is always squinted, which breaks the symmetry of the wavenumber support about k_x. The coupling of the range and azimuth wavenumbers means that they are no longer separable in terms of time and range frequency. The isolines in the left panel of Figure 3.3b show that a fixed value of range or azimuth wavenumbers traverses both time and frequency.

3.2.4. Temporal Lag and Spectral Shift

We are interested in the difference between the supports of two SAR images acquired by two instruments with a physical separation $\Delta\mathbf{r}(t)$. We express the wavenumbers in the support of the first sensor by setting $i = 1$ in (3.21), and define the support of the second sensor as

$$\mathbf{k_2}(t, f_r; \theta_l) = k_0(f_r)\big(\hat{\mathbf{l}}_{\mathbf{T_1}}(t) + \hat{\mathbf{l}}_{\mathbf{R_1}}(t) + \Delta\mathbf{l}_{\mathbf{T}}(t) + \Delta\mathbf{l}_{\mathbf{R}}(t)\big), \tag{3.23}$$

where

$$\Delta\mathbf{l}_{\mathbf{S}}(t) = \frac{\mathbf{r}_{\mathbf{S_1}}(t) + \Delta\mathbf{r}_{\mathbf{S}}(t) - \mathbf{r}_{\mathbf{p}}}{\|\mathbf{r}_{\mathbf{S_1}}(t) + \Delta\mathbf{r}_{\mathbf{S}}(t) - \mathbf{r}_{\mathbf{p}}\|} - \hat{\mathbf{l}}_{\mathbf{S_1}}(t), \tag{3.24}$$

is the difference between the line of sight vectors due to the relative position of the second instrument with respect to the first. The first-order Taylor expansion of (3.23) about (τ_c, f_c) is

$$\begin{aligned}\mathbf{k_2}(t, f_r; \theta_l) \approx\ & (k_0 + \Delta k)(\hat{\mathbf{l}}_{\mathbf{T_1}}(\tau_c) + \hat{\mathbf{l}}_{\mathbf{R_1}}(\tau_c) + \Delta\mathbf{l}_{\mathbf{T}}(\tau_c) + \Delta\mathbf{l}_{\mathbf{R}}(\tau_c)) \\ &+\ k_0 \frac{\partial}{\partial t}(\hat{\mathbf{l}}_{\mathbf{T_1}} + \hat{\mathbf{l}}_{\mathbf{R_1}} + \Delta\mathbf{l}_{\mathbf{T}} + \Delta\mathbf{l}_{\mathbf{R}})(\tau_c)\Delta t \qquad (3.25) \\ =\ & \mathbf{k_1}(t, f_r; \theta_l) + (k_0 + \Delta k)\Delta\mathbf{l}(\tau_c) + k_0 \frac{\partial \Delta\mathbf{l}}{\partial t}(\tau_c)\Delta t, \qquad (3.26)\end{aligned}$$

where we have used $k_0 = k_0(f_c)$, $\Delta k = \frac{\partial k_0}{\partial f_r}(f_c)(f_r - f_c)$, $\Delta t = t - \tau_c$, $\Delta\mathbf{l} = \Delta\mathbf{l}_{\mathbf{T}}(\tau_c) + \Delta\mathbf{l}_{\mathbf{R}}(\tau_c)$ for brevity, and we have neglected $\Delta f \Delta t$ cross terms.

To align the two images we fix the support of the first image at the beam crossing time and at the center frequency and solve for the $(\Delta t, \Delta k)$ where the second support intersects the first

$$\mathbf{k_1}(\tau_c, f_c; \theta_l) = \mathbf{k_2}(t, f_r; \theta_l). \tag{3.27}$$

Simplifying (3.27) leads to

$$\Delta k(\mathbf{l}+\Delta\mathbf{l}) + k_0 \frac{\partial(\mathbf{l}+\Delta\mathbf{l})}{\partial t}(\tau_c)\Delta t = -k_0\Delta\mathbf{l}(\tau_c), \tag{3.28}$$

where $\mathbf{l} = \hat{\mathbf{l}_{\mathbf{T_1}}}(\tau_c) + \hat{\mathbf{l}_{\mathbf{R_1}}}(\tau_c)$.

Until now, no assumption has been made on the reference frame of vectors $\mathbf{k_1}$ and $\mathbf{k_2}$. Recalling 3.2.2, the information in the interferogram comes from the surface-projected wavenumbers where the regions of support of the two images coincide. Thus, to relate the difference in the support to the temporal lag and spectral shift, we need to solve (3.27) in a reference frame where two of the basis vectors are aligned with the ground range and azimuth directions. Equation (3.28) is an overdetermined system of three equations and two unknowns. However, we can remove one equation from the system by projecting the wavenumbers on the plane tangent to the surface. After coordinate transformation and projection, (3.27) becomes

$$\mathbf{k_{1xy}}(\tau_c, f_c; \theta_l) = \mathbf{k_{2xy}}(t, f_r; \theta_l), \tag{3.29}$$

where $\mathbf{k_{1xy}}(\tau_c, f_c; \theta_l) = \mathbf{\Gamma k_1}(\tau_c, f_c; \theta_l)$ and $\mathbf{k_{2xy}}(t, f_r; \theta_l) = \mathbf{\Gamma k_2}(t, f_r; \theta_l)$ and $\mathbf{\Gamma}$ is a matrix representing the surface projection to the tangent plane of the resolution cell. Figure 3.4 shows the tangent plane for a given point on the surface, the two basis vectors along the plane and the basis vector normal to the plane, and the wave vectors of two instruments and their projections at the temporal lag and spectral shift where they align.

We model the surface projection by

$$\mathbf{\Gamma} = \mathbf{Q_{Xx}}\left(\mathbf{I} - \hat{\mathbf{n}}\hat{\mathbf{n}}^T\right), \tag{3.30}$$

where $\mathbf{Q_{Xx}}$ is the direction cosine matrix from the reference frame that the vectors are expressed in to the local tangent frame, and $\hat{\mathbf{n}}$ is the unit vector normal to the surface expressed in the reference frame of the wavenumber vectors. We define the local tangent plane with two basis vectors that lie within the plane, one aligned with the interferogram's ground range direction and one with the azimuth direction, and complete it with $\hat{\mathbf{n}}$. The second term of (3.30) projects the vector on the tangent plane, while the first term transforms the vector to the local tangent frame. Hence, a vector multiplied by $\mathbf{\Gamma}$ defined in (3.30) will have a third component equal to zero.

Multiplying both sides of (3.28) by $\mathbf{\Gamma}$ yields

$$\begin{pmatrix} k_0\left(\frac{\partial(\mathbf{l}+\Delta\mathbf{l})}{\partial t}(\tau_c)\right)_x & (\mathbf{l}+\Delta\mathbf{l})_x \\ k_0\left(\frac{\partial(\mathbf{l}+\Delta\mathbf{l})}{\partial t}(\tau_c)\right)_y & (\mathbf{l}+\Delta\mathbf{l})_y \end{pmatrix} \begin{pmatrix} \Delta t \\ \Delta k \end{pmatrix} = -k_0\Delta\mathbf{l}. \tag{3.31}$$

Equation (3.31) provides an analytic solution to Δt and Δk, and it is valid if Δt and Δk are sufficiently small for second and higher order terms to be neglected. In cases where the first-order expansion is invalid, we can compute the solution to (3.27) numerically using an optimization method.

3.2.5. Height Sensitivity

After solving for the temporal and spectral shift according to (3.31), the sensitivity can be computed from the difference of the aligned wavenumber supports. The interferometric phase of a resolution cell is

$$\phi(\Delta t, \Delta f) = \Delta\mathbf{k}(\Delta t, \Delta f) \cdot \boldsymbol{\zeta}, \tag{3.32}$$

where $\boldsymbol{\zeta}$ is the elevation vector and $\Delta\mathbf{k}(\Delta t, \Delta f)$ is the difference of the aligned supports

$$\Delta\mathbf{k}(\Delta t, \Delta f) = \mathbf{k_2}(\tau + \Delta t, f_c + \Delta f; \theta_l) - \mathbf{k_1}(\tau, f_c; \theta_l). \tag{3.33}$$

Figure 3.4 illustrates the supports of the aligned surface-projected wavenumber supports. The orange line on the tangent plane represents the surface projection of the first support $\mathbf{k_{1_{xy}}}$ at the beam crossing time τ_c. Examining the definition of the wave vector in (3.21) reveals that by not fixing the range frequency of the wave vector, $\mathbf{k_{1_{xy}}}$ becomes a line that is parallel to the surface projection of the line of sight and passes through the origin. At the solution of (3.29), the surface-projected support of the second wave vector coincides in the Fourier space with the surface-projected support of the first acquisition at the beam crossing time and center frequency. While the surface projections of the supports are equal to each other, their components in the normal direction to the surface are different. The dot product of this difference with the elevation gives rise to the interferometric phase, and drives the sensitivity.

In a SAR image, a scatterer is placed at the intersection of the iso-range and iso-Doppler surfaces. In the monostatic case, these reduce to the known iso-range sphere and iso-Doppler cone. Generally, the range and Doppler surfaces are

$$R \text{ ellipsoid: } R = \|\mathbf{l_T}(t)\| + \|\mathbf{l_R}(t)\| \tag{3.34}$$

$$\begin{aligned} f_D \text{ surface: } f_D &= \frac{1}{\lambda_c}\left(\hat{\mathbf{l_T}}(t) \cdot \mathbf{v_T}(t) + \hat{\mathbf{l_R}}(t) \cdot \mathbf{v_R}(t)\right) \\ &= \tilde{\nu}_c\Big(\hat{\mathbf{l_{T0}}}(t) \cdot \mathbf{v_T}(t) + \hat{\mathbf{l_{R0}}}(t) \cdot \mathbf{v_R}(t) \\ &\qquad + \frac{\mathbf{r}}{\|\mathbf{l_{T0}}(t) + \mathbf{r}\|} \cdot \mathbf{v_t}(t) + \frac{\mathbf{r}}{\|\mathbf{l_{R0}}(t) + \mathbf{r}\|} \cdot \mathbf{v_R}(t)\Big) \\ &\approx f_D(\mathbf{r_0}) + \tilde{\nu}_c \mathbf{r} \cdot \left(\frac{\mathbf{v_T}(t)}{\|\mathbf{l_{T0}}\|} + \frac{\mathbf{v_R}(t)}{\|\mathbf{l_{R0}}\|}\right), \end{aligned} \tag{3.35}$$

where in the equation of the Doppler shift we have expressed the scatterer location as the sum of a reference position and a relative position $\mathbf{r_p} = \mathbf{r_0} + \mathbf{r}$ and approximated $\|\mathbf{l_{T0}}(t) + \mathbf{r}\|$ and $\|\mathbf{l_{R0}}(t) + \mathbf{r}\|$ as $\|\mathbf{l_{T0}}\|$ and $\|\mathbf{l_{R0}}\|$ respectively. The locus of points that satisfy conditions (3.34) and (3.35) is a line. Conventionally, SAR images are focused at the zero-Doppler location, i.e. $f_D = 0$. Thus, the solution lies on a line on the surface of the range ellipsoid. All scatterers at the same range and with the same zero-Doppler location are positioned along this line, regardless of the incidence angle of their location.

Cross-track interferometry (XTI) solves for the missing third dimension by positioning a scatterer at a look angle on the line of constant range and Doppler. After

applying the plane-wave approximation at the vicinity of the scatterer, the curve along which the solution lies becomes a straight line. XTI locates the scatterer along the fronts of the plane wave. Hence, an interferometer is sensitive to the elevation along this line, normal to the range and Doppler directions. The height normal to the surface is related to the elevation

$$z(t) = \zeta(t)\hat{\boldsymbol{\zeta}} \cdot \hat{\mathbf{z}}, \tag{3.36}$$

where $\boldsymbol{\zeta}$ is orthogonal to both the iso-range lines and the iso-Doppler lines

$$\boldsymbol{\zeta} = (\hat{\mathbf{l_T}} + \hat{\mathbf{l_R}}) \times \left(\frac{\mathbf{v_T}}{\|\mathbf{l_T}\|} + \frac{\mathbf{v_R}}{\|\mathbf{l_R}\|} \right) \tag{3.37}$$

and $\hat{\boldsymbol{\zeta}} = \boldsymbol{\zeta}/\|\boldsymbol{\zeta}\|$.

Taking the derivative of the interferometric phase (3.32) with respect to height yields the sensitivity of the interferometer to height

$$\frac{\partial \phi}{\partial z} = \Delta \mathbf{k}_\zeta(\Delta t, \Delta f) \frac{\partial \zeta}{\partial z}, \tag{3.38}$$

where $\Delta \mathbf{k}_\zeta(\Delta t, \Delta f)$ is the ζ component of the aligned support difference and from (3.36) we can express the derivative of the elevation with respect to height as $1/\hat{\boldsymbol{\zeta}} \cdot \hat{\mathbf{z}}$. Thus, the sensitivity is the difference between the aligned supports, in the elevation direction, inverted to the vertical direction.

3.3. Simulations and Results

3.3.1. Simulations

We simulate three different interferometers. In all three, the receiving SAR satellites are flying in a Helix formation [20]. The first has a tangential and radial separation between the two sensors, and we simulate both monostatic and bistatic operation with a common transmitter. The two antennas point in the zero-Doppler direction. The second also looks in the zero-Doppler direction, but only has a normal separation and operates monostatically. Thus, the effective temporal lag is $0\,\mathrm{s}$. The third is a system inspired by Harmony and consists of three SAR satellites: an illuminator and two formation-flying receivers, that lag the illuminator by $350\,\mathrm{km}$ [59]. The Helix formation combines radial, normal, and tangential separations that vary sinusoidally along the orbit. Due to the bistatic operation the two receivers are looking forward, i.e. they have a squint, with respect to the zero-Doppler direction. Table 3.1 lists the parameters of the three simulation scenarios, where $a\Delta e$ and $a\Delta\Omega$ are the magnitudes of the relative eccentricity and relative inclination vectors of the formation, as defined in [20], and both vectors have a phase of $-\pi/2$. Figure 3.5 illustrates the satellite configurations of the three cases.

The first two scenarios use a formation that models a pure ATI and a pure XTI respectively. In the first case, we expect the temporal lag calculated using the wavenumber method to match the along-track physical separation between the

Table 3.1.: The parameters of the interferometer used in the different simulation scenarios.

Case	$a\Delta e$ / m	$a\Delta\Omega$ / m	Operation
1	50	0	Monostatic & Bistatic
2	0	650	Bistatic
3	125	650	Bistatic

two formation satellites. Similarly, we expect the sensitivity of the cross-track interferometer to match the sensitivity calculated from the conventional equation in the second case. We simulate the second case in a flat-Earth frame to eliminate the effect of the Earth's rotation and curvature. In the other cases, we carry out the simulations in an Earth-centered Earth-fixed frame before transforming to a local-tangent local-normal frame as discussed in (3.30).

The last scenario poses challenges, as it cannot be accurately modeled with conventional geometric approaches. The combination of bistatic operation and a squinted line of sight results in under or overestimating the temporal lag if only the physical separation is used. Locating the shift needed for the lines of sight of the two receivers to align yields a more accurate estimate, but the bistatic operation means that the two receivers do not have a single line of sight between them and the surface.

Using the monostatic equivalent can offer a way out, but the questions of where to place the equivalent system and how to convert the along-track and perpendicular baselines of the formation to those of the equivalent system are not trivial. Our numerical experiments have shown that using the geometric method of aligning the monostatically equivalent lines of sight of the two systems approaches the results of the wavenumber method when the monostatic equivalent system is placed at the intersection of the bistatic line of sight and the line segment between the transmitter and receiver. Hence, a unique ME exists for each combination of incidence angle and slow time, as Figure 3.1 illustrates. The geometric method is explained in detail in the Appendix.

3.3.2. Results

In this subsection, we present the temporal lag and sensitivity to height of three different interferometric configurations based on computational simulations. Figure 3.6 shows the temporal lag of a Helix interferometer with only an $a\Delta e$ component (case 1). This means that the along-track separation of the interferometer varies sinusoidally along the orbit with an amplitude of $2a\Delta e$ [20]. The temporal lag of a monostatic interferometer that looks perpendicular to the flight direction is equal to the along-track separation divided by the flight velocity. If the interferometer operates bistatically, then the along-track baseline halves. The along-track baseline, calculated using the wavenumber method of (3.31), matches the expected result.

Figure 3.7 illustrates the sensitivity to height of a Helix formation that has a separation only in the normal direction (case 2). The sensitivity is calculated as follows:

1. Find the temporal lag and a frequency shift given by (3.31).
2. Compute the spectral support of the first sensor at the beam crossing time and the center frequency. Compute the spectral support of the second sensor at the shifts found in the previous step.
3. Calculate the sensitivity using (3.38).

The sensitivity of a monostatic cross-track interferometer with an unsquinted line of sight is described by the well-known expression in the literature [50, 51]. The right panel in Figure 3.7 shows the relative error between the sensitivity calculated using the method proposed in this chapter and the classical expression of the interferometric sensitivity.

Moving on to a more complex geometry, Figure 3.8 shows the temporal lag of Helix interferometer with $a\Delta e = 125\,\mathrm{m}$ and $a\Delta\Omega = 650\,\mathrm{m}$ (case 3). In this case, two factors complicate the geometry:

1. The bistatic operation of the receivers with an illuminator that is significantly ahead of the Helix formation.
2. The significant line-of-sight squint of the receiving instruments that is needed to follow the transmitter's beam.

We compare the temporal lag obtained using the wavenumber method to the temporal lag calculated using the geometric method of finding the along-track shift that aligns the lines of sight of the monostatic equivalents. The absolute error between the two methods peaks at $0.40\,\mathrm{ms}$.

The sensitivity to height of the configuration is shown on the left panel of Figure 3.9. The right panel displays the relative difference between the spectrally derived sensitivity and the sensitivity calculated using the monostatic equivalent method explained in the Appendix. We used the angle between the monostatic equivalent's line of sight and the normal to the surface as the incidence angle when computing the sensitivity with the geometric method. A different result, which is closer to the sensitivity obtained with the spectral method, is obtained when the complementary angle to the angle between the elevation direction $\hat{\zeta}$ and the normal to the surface is used as the incidence angle. We have defined this angle mathematically in (C.7). Figure 3.10 shows the relative difference between the spectrally derived sensitivity and the sensitivity based on the geometric method, with the latter definition of the incidence angle.

3.4. Discussion

The first two simulation scenarios act as tests to validate that the proposed wavenumber method for calculating the temporal lag and sensitivity produces sensible results. In the first scenario, we are testing the calculation of the temporal lag.

Hence, we set up a Helix formation whose separation vector has a dominant along-track component, and a smaller radial component. In the baseline case, which is shown in the left panel of Figure 3.6, we model both instruments as monostatic SARs with no squint. In this case, we expect to see the along-track baseline to closely match the along-track separation of the formation and to have a small dependence on range. If the second receiver operates bistatically, using the first instrument as a transmitter, then the along-track baseline should be half the along-track separation. The results in Figure 3.6 match these results.

In the second simulation scenario, we set up a Helix formation with a significant normal separation. Like the first scenario, we assume that the instruments operate monostatically and look in the zero-Doppler direction. Hence, we expect the spectrally derived sensitivity to agree with the expression for the sensitivity found in the literature. Figure 3.7 shows that the results are in agreement with the conventional expression for the sensitivity.

We have verified that the wavenumber method agrees with the conventional expressions of along-track baseline and sensitivity for geometrically simple cases. We now move on to the more interesting case of a bistatic interferometer with an illuminator that leads the receivers by $350\,\mathrm{km}$. The receivers are flying in a Helix formation with both an ascending node difference and an eccentricity difference. Thus, the separation of the receiving satellites varies in all three directions, the radial, the normal, and the tangential, sinusoidally with time.

Figure 3.8 shows the temporal lag estimated using (3.31) on the left, and the geometric approximation on the right. Here we are starting to see the two methods diverging. While a peak absolute difference of $0.40\,\mathrm{ms}$ might sound small, it is considerable when two SAR images need to be precisely aligned before processing is carried out to produce interferometric estimates. Furthermore, considerable effort was spent to have the geometrically calculated temporal lag approach the spectral temporal lag. Each satellite position and each incidence angle produce a unique monostatic equivalent system for each of the two pairs of transmitter and receiver.

The computationally cheaper and conceptually simpler approach of positioning the monostatic equivalent at the midpoint of the transmitter and receiver, thus having a common ME position for all incidence angles at a given instance of time, performs worse compared to the results presented in Figure 3.8. The simpler geometric method overestimates the extremes of the temporal lag by $7\,\mathrm{ms}$ and misses its distribution with respect to time and range. In contrast to both variants of the geometric approach, the wavenumber method works for both monostatic and bistatic systems without requiring the calculation of virtual equivalent systems.

Figure 3.9 illustrates the sensitivity to height of the same Helix formation in the left panel. The distribution of the values, and the variation with time and incidence angle are in agreement between the two methods. There is a small but not insignificant difference in the magnitude of the sensitivity. The relative difference in the sensitivity estimated with the two methods is plotted in the right panel. The largest difference, which tends to 7%, is in the near range and over the equator,

which is where the normal separation of the formation also reaches its maximum.

During our experiments, we have found that changing the incidence angle used for the computation of the geometric sensitivity to the one defined by the complementary angle to the angle between the elevation and the normal directions reduces the relative error between the spectral sensitivity and the geometric sensitivity in scenarios that involve a complex formation, such as in the third scenario of Table 3.1. Figure 3.10, illustrates the improvement in the relative error, with a reduction of the maximum relative difference from 7% to 0.12% in the near range at equatorial latitudes, and a marked improvement throughout the domain. The latter definition of θ_i accounts for the fact that the line of sight and the elevation direction are not coplanar, when the line of sight is squinted. The spectral method accounts for this directly by computing the wavenumber support difference along $\hat{\zeta}$. Thus, making this adjustment to the geometric method brings the results closer to those obtained with the spectral method.

Furthermore, for both sensitivity calculations of scenario 3 we have scaled the expression of the sensitivity by the modulus of the bistatic line of sight. Whereas in a true monostatic system the scaling factor would be equal to 2, in a bistatic system, the modulus of the line of sight is less than 2. The divergence of the modulus from 2 increases as the bistatic angle increases. Thus, in the monostatic equivalent of such an interferometer, the true modulus of the line of sight should be used. We discuss the line of sight modulus scaling factor and its effect on the results further in the Appendix.

We note to the reader that we were able to arrive to these modifications to the conventional expression of the sensitivity by iteratively experimenting with different adjustments and scaling factors. In light of this, the result of Figure 3.10 serves as a cross-check of the geometric method against the spectral method. In configurations with larger bistatic angles or larger separations, the two methods diverge further.

The divergence stems from the fact that no monostatic system can capture the radiometric and interferometric properties of a bistatic system with sufficiently large baselines over different look angles and slow-time instants. As Figure 3.1 shows, different look angles have different monostatic equivalent positions. Yet the difference between these positions is significantly larger than the distance that the satellite would travel in the time taken for the echoes of adjacent resolution cells to reach the instrument. Thus, the spectral method of calculating the temporal lag, spectral shift, and sensitivity to height is superior, as it works regardless of the complexity of the separation between the two SARs or whether the system operates mono- or bistatically without the need to compute virtual systems and introduce scaling factors.

3.5. Conclusion

We have presented a method that uses the wavenumber support to compute the temporal lag and sensitivity of single-pass interferometers. Our method solves the problems that arise due to the difficulty of applying the monostatic equivalent ap-

proximation to interferometers with complex geometries. The proposed method accommodates both monostatic and bistatic interferometers without requiring adjustments to switch between the two. Furthermore, using the first-order linear expansion of the spectral support provides a simple system of equations that can be efficiently solved computationally.

Results from simulations show that for a Helix formation, the geometric method overestimates the temporal lag. Furthermore, the sensitivity estimated using the geometric method has a relative difference of up to 7% compared to the sensitivity estimated using the wavenumber method. Accurate knowledge of these parameters is necessary when designing cross-track interferometers to estimate the relative topography of dynamic surfaces, such as the ocean. Additionally, accurate knowledge of the temporal lag and wavenumber shift between SAR surveys will benefit the processing of interferograms from future SAR missions that will feature squinted lines of sight and bistatic operation. The method is also useful for repeat-pass interferometry, as it allows the accurate computation of the reference orbits for processing. In the future, we aim to expand on this work by validating the method with an end-to-end simulation of SAR observables from a dynamic surface.

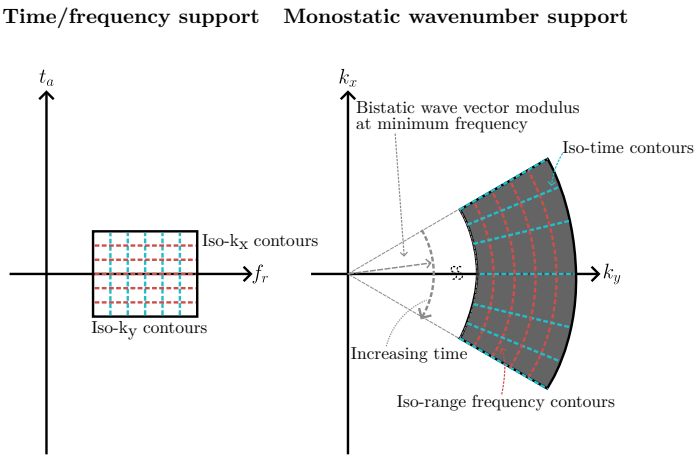

(a) Monostatic interferometer

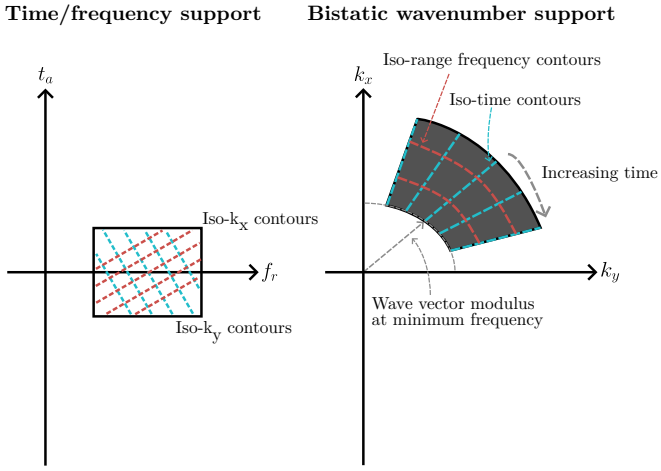

(b) Bistatic interferometer

Figure 3.3.: The time-frequency and the corresponding wavenumber region of support of a resolution cell for (a) a monostatic and (b) a bistatic interferometer. We note that the modulus of the bistatic wave vectors is smaller than that of the monostatic wave vectors for the same range frequency. We illustrate the modulus of the bistatic wave vector at the minimum range frequency in both support diagrams. The difference of the moduli is exaggerated in the diagram for the purposes of illustration. Furthermore, the aperture time that we consider for these diagrams is larger than what is typically used in real-world systems to illustrate the shape of the region of support. In a real-world radar, the wavenumber region of support in (a) would look rectangular, and that in (b) trapezoidal, as they would only be a slice of illustrated regions.

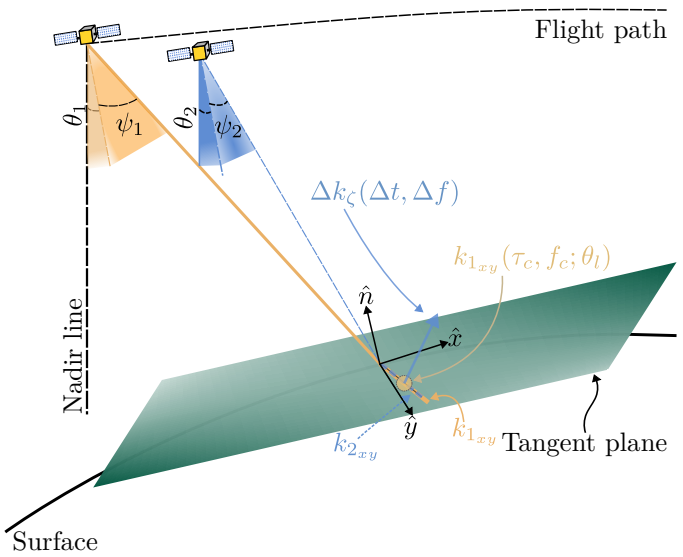

Figure 3.4.: The figure shows the plane tangent to a given point on the surface and the basis vectors of the reference frame used to align the wavenumber support of the two SAR systems. Two SAR satellites with different look angles and squints are shown. The wave vectors of the first and second system are shown in orange and blue colors, respectively. For ease of illustration, the figure omits the transmitting satellites and instead displays two monostatic satellites; thus the bistatic wave vector reduces to $\mathbf{k_i} = 2\mathbf{k_{i_T}}$. The concept remains the same for bistatic systems. The surface-projected wave vectors of the two instruments, $\mathbf{k_{1_{xy}}}$ and $\mathbf{k_{2_{xy}}}$, at the moment of alignment, are shown on the tangent plane. The circle at the midpoint of $\mathbf{k_{1_{xy}}}$ represents the point at which we fix the support of the first acquisition when solving (3.29). The figure also illustrates the component of the difference of the aligned wave vectors in the elevation direction, $\Delta\mathbf{k}_\zeta(\Delta t, \Delta f)$. The difference of these vectors drives the sensitivity to the surface height.

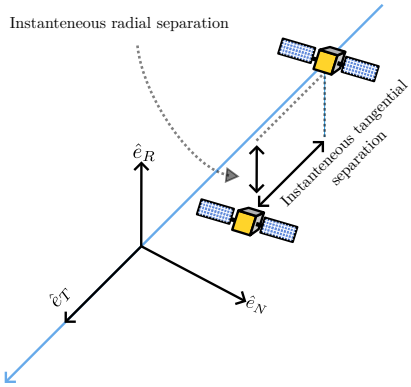

(a) The first case, with a tangential and radial component that vary with time.

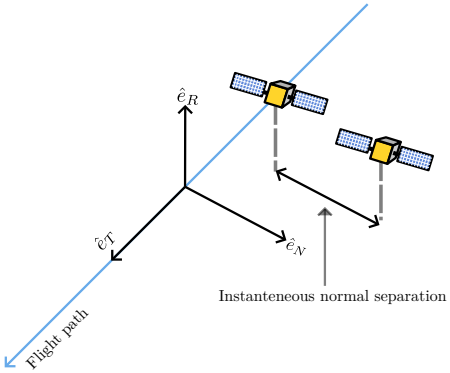

(b) The second case, with only a normal component that varies with time.

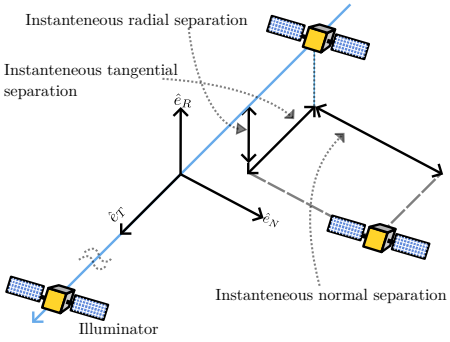

(c) The third case, with separations in the three directions varying with time.

Figure 3.5.: An illustration of the three different satellite configurations used for the simulation experiments.

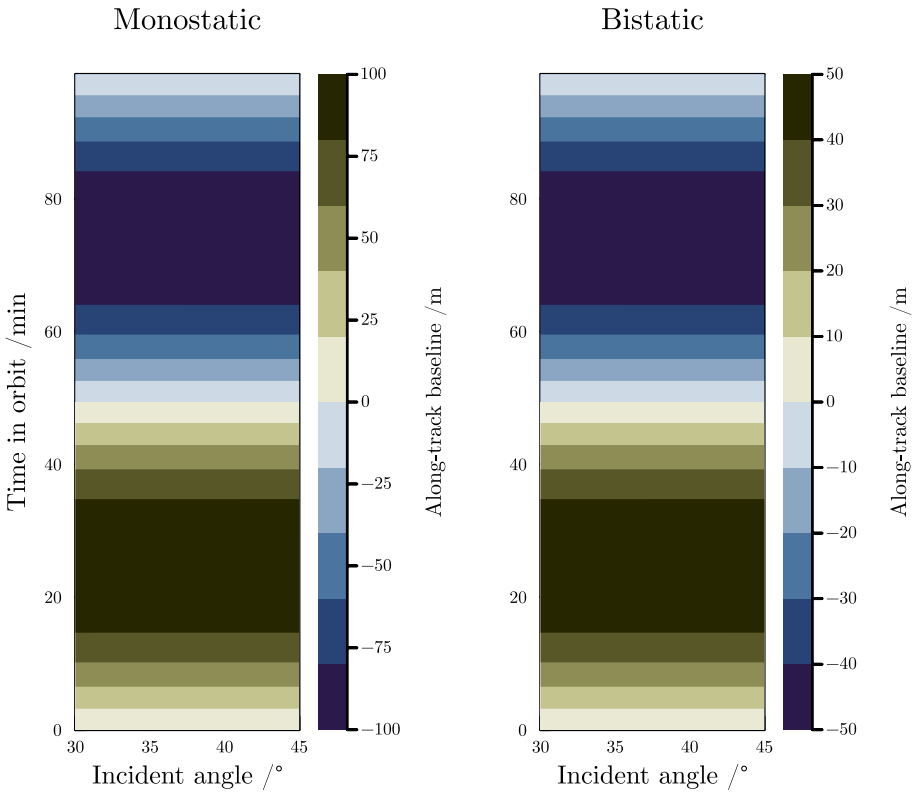

Figure 3.6.: The temporal lag of case number 1 in Table 3.1. The left panel shows the temporal lag of monostatic interferometer and the right panel that of a bistatic interferometer.

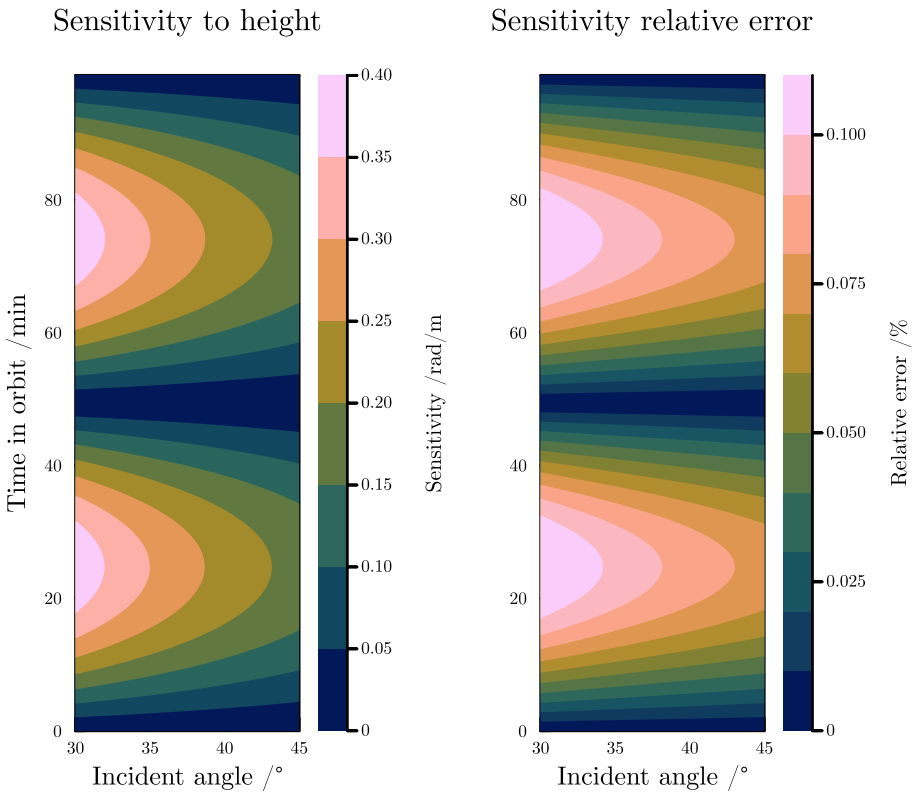

Figure 3.7.: A formation with a 650 m ascending node difference. Left panel: The sensitivity to height. Right panel: The relative error of the sensitivity calculated using the wavenumber method with respect to the conventional sensitivity expression.

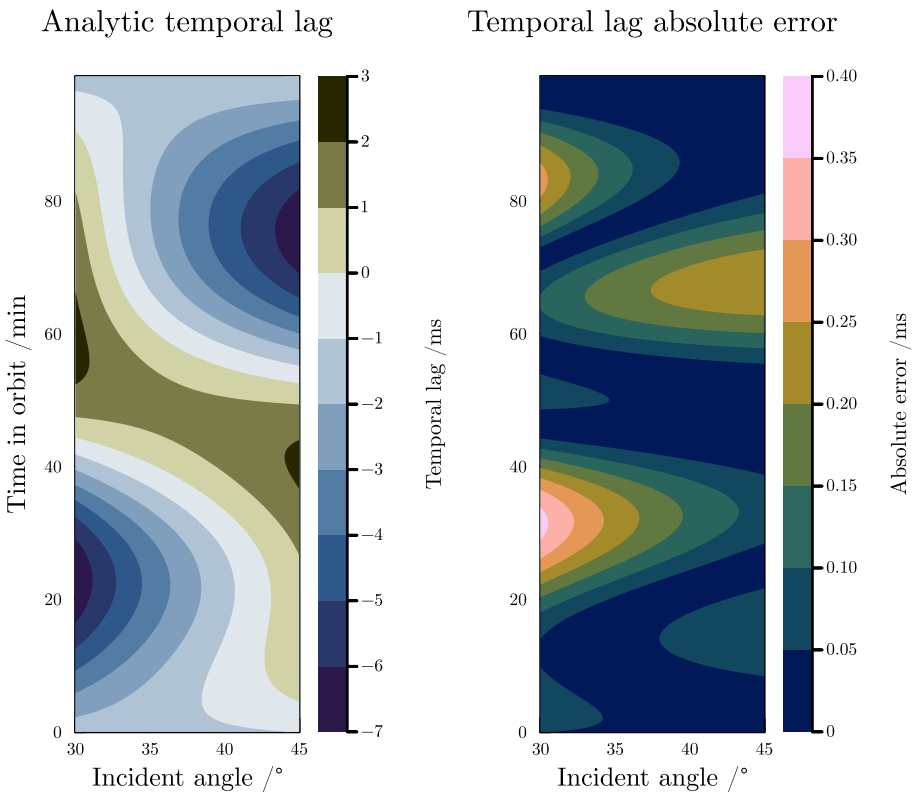

Figure 3.8.: A formation with a $650\,\mathrm{m}$ ascending node difference and a $125\,\mathrm{m}$ radial difference. Left panel: The temporal lag using the wavenumber method. Right panel: The absolute error between the temporal lag calculated spectrally and the temporal lag calculated using the geometric method.

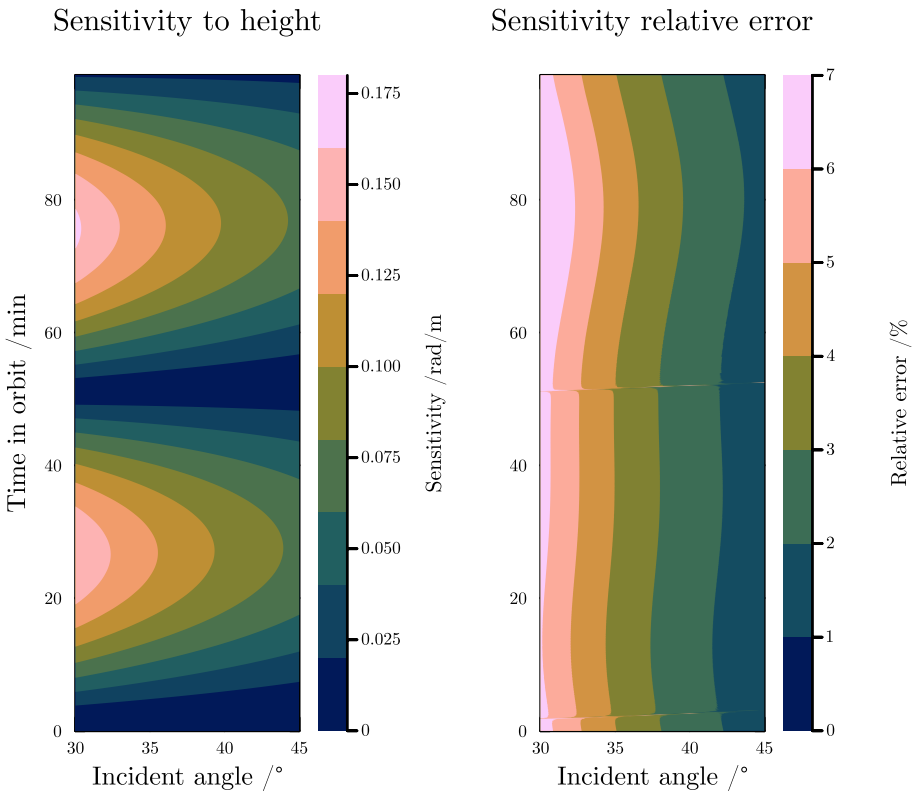

Figure 3.9.: A formation with a 650 m ascending node difference and a 125 m radial difference. Left panel: The sensitivity to height. Right panel: The relative error of the sensitivity calculated using the wavenumber method with respect to the conventional sensitivity expression.

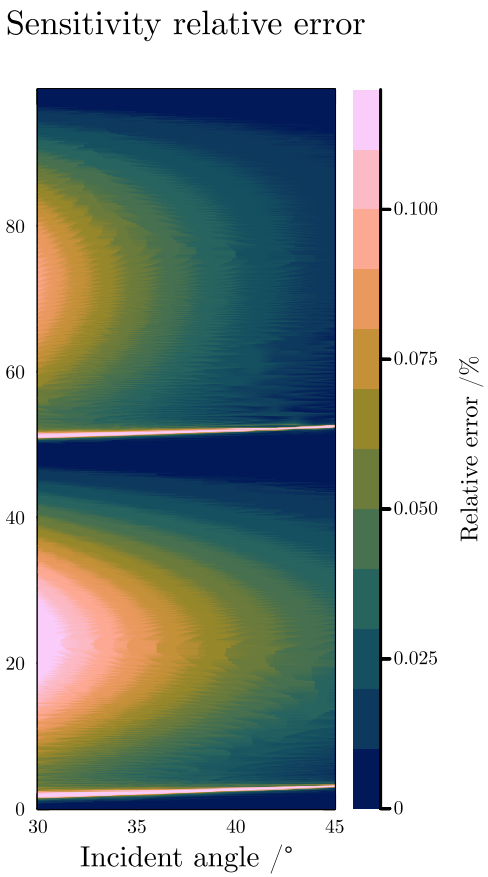

Figure 3.10.: The relative difference between the height sensitivity obtained with the proposed wavenumber-domain method and the range-dependent adjusted geometric approach discussed in the Appendix.

4

Synchronizing Bistatic SAR Signals from Data

Or How to Tackle the Elephant in the Room

The Harmony mission features two bistatic synthetic-aperture radar (SAR) companions of Sentinel-1. As with any multistatic system, frequency deviations among the oscillators of the receivers cause a phase error in the phase of the demodulated SAR signal. Given that interferometry will be used to retrieve geophysical parameters from Harmony's radar instruments, an erroneous phase difference between the SAR signals of the two companions will bias the retrieval. The companions will use a global-navigation system (GNSS)-based method to synchronize the phase of the signals. The residual phase that remains after the synchronization is significant enough to make the retrieval of relative sea-surface height (RSSH) impossible. In this chapter, we present a data-driven algorithm to remove the synchronization residual. The algorithm uses the multisquint processing approach, together with the overlap regions of the TOPSAR acquisition mode, to estimate the derivative of the residual. After running the algorithm, simulations suggest that the error signal reduces from a standard deviation of 4° *to* 0.01°*, allowing the retrieval of RSSH from Harmony data.*

4.1. Introduction

BISTATIC and multistatic synthetic-aperture radars (SARs) offer the following advantages over monostatic SARs: flexible interferometric baselines, line of sight diversity, lower cost and simplicity of electronics due to a common transmitter. These benefits come at the cost of the complexity, in terms of mission planning, operations, and processing. By definition, bistatic SARs use different oscillators to modulate the radar carrier at the transmitter and to demodulate the carrier at the receiver. Any deviation in the instantaneous frequency or phase of the oscillators introduces a phase error in the radar signal. The error will degrade any measurement that leverages the phase of the signal, such as synthetic-

aperture radar interferometry (InSAR) and synthetic-aperture radar tomography based measurements. Thus, in addition to the aforementioned costs, phase synchronization is an unavoidable challenge of multistatic systems.

One such application of single-pass cross-track interferometry (XTI) is the measurement of the sea-surface height (SSH). SSH is the elevation of the sea surface with respect to the reference ellipsoid, and XTI measures the height variation relative to the mean height of the surface. In this chapter, we refer to this relative elevation as relative sea-surface height. Using the height of the mean surface of an acquisition relative to the reference ellipsoid, one can obtain the SSH from measurements of the RSSH. Oceanographic studies, both theoretical and numerical, show that flows with horizontal scales in the order of $0.1\,\mathrm{km}$ to $10\,\mathrm{km}$, the so called *submesoscales* [2], play a critical role in the oceanic and atmospheric energy transfer, the mixing of heat and nutrients, and the sea state [2, 5, 6, 60]. Measurements of the SSH at a resolution sufficient to resolve these scales are necessary to validate these studies and improving our understanding of oceanic physics.

Until recently, no remote sensing instrument was able to provide such measurements. The observational gap [19], was one of the primary motivations for the Surface Water and Ocean Topography (SWOT) mission of NASA/CNES [61]. SWOT characterizes ocean circulation from SSH measurements at spatial resolutions of $15\,\mathrm{km}$, by using a single-platform cross-track interferometer made of two Ka-band SARs.

Harmony, the European Space Agency's 10th Earth Explorer [21], consists of two satellites that will fly together with Sentinel-1. Each spacecraft will carry a passive SAR that will use Sentinel-1 as a transmitter, and a thermal infrared instrument. Harmony is a multipurpose mission, that aims to quantify small-scale motion and deformation fields of the ocean surface, glaciers and ice sheets, and solid Earth [21]. In [62], the authors propose a measurement concept to retrieve RSSH using a formation of bistatic SARs, with the potential to resolve submesoscale RSSH. We have been working to introduce an experimental RSSH product for Harmony using this concept. However, the concept requires phase synchronization to work.

There are different techniques to synchronize bistatic SAR data. The most direct method is using a bidirectional synchronization link between the satellites to exchange clock information, as employed in TanDEM-X [23, 63]. We refer to bistatic systems that exchange clock information as cooperative [64]. Cooperative systems require additional hardware to enable the information exchange between the satellites.

Phase synchronization of non-cooperative systems, i.e. systems that do not exchange clock information, unavoidably relies on information either directly from the SAR signals or from auxiliary data. Harmony is a non-cooperative system, as it does not have the means to exchange information between the companions. The impact of the lack of synchronization on bistatic SAR imaging was first discussed by Auterman in [65]. Massonet and Vadon discussed the use of repeat-pass interferometry to estimate the clock drift of the European Remote Sensing satellite [66]. The DLR-ONERA team discussed the synchronization of bistatic SAR signals, and

demonstrated bistatic XTI from an airborne system [67]. The synchronization was based on information from the monostatic and bistatic SAR signals. Estimating the synchronization phase from the received signals, also known as autosync, has been demonstrated with a spaceborne sensor using TanDEM-X experiments [68]. Autosync's performance depends on the backscattering of the scene, making it suboptimal for interferometric applications.

Recent advances in the field show that the phase synchronization error can be reliably corrected using a global navigation satellite system (GNSS) based technique [69]. This follows from the fact that the part of the GNSS solution is the phase difference between the GNSS-receiver reference clock and the GNSS reference. Therefore, after making sure that the GNSS receiver and the radar payload share a common reference oscillator, phase-synchronization becomes a by-product of the Precise Orbit Determination (POD) step. The results of [69] suggest that this approach can estimate the phase synchronization error if systematic errors are suppressed. Specifically, at C-band the method achieves synchronization with a standard deviation of $1.6°$. Since the estimation of the error happens at the carrier frequency of the GNSS signal (L-band), the solution degrades, assuming spectral purity of frequency conversion stages, linearly with frequency, reaching a cutoff in terms of usability near X-band [69].

Harmony's RSSH error budget allocates a synchronization error with a $1.0\,\mathrm{cm}$ standard deviation [62]. This value is set to allow the resolution of RSSH at the submesoscales. By using the minimum and maximum interferometric sensitivity of Harmony reported in [46], we convert this value to a phase error of $0.04°$ to $0.10°$. Therefore, we need to improve upon the GNSS-based phase synchronization to make the retrieval of RSSH possible.

In this article, we present a data-driven calibration algorithm that reduces the residual phase synchronization error that is left in the radar signal after the GNSS-based synchronization has been carried out. The algorithm suits the retrieval of small signals that require a high sensitivity, such as RSSH. Our algorithm builds upon the multisquint processing introduced in [70, 71], as well as autosync [68], and uses the system inversion approach similarly to [72]. It leverages the overlap regions, where samples are acquired twice for the same region on the surface, of the Terrain Observation by Progressive Scans (TOPSAR) mode by using the samples at the overlaps as additional, more robust estimates of the finite difference of the phase synchronization residual.

The structure of the chapter is as follows: We start by introducing a model for the phase of the bistatic SAR signal due to the non-synchronous operation, and a model for the residual error that remains after GNSS-based synchronization in Section 4.2. In Section 4.4, we simulate the RSSH that Harmony would retrieve for a scene based on the outputs of a coupled ocean-atmosphere model in the Bay of Biscay, France, and run the algorithm on the simulated data. Section 4.5 discusses the results and the performance of algorithm in terms of the semivariogram, identifies two sources of errors, discuss potential solutions. Finally, in Section 4.6 we conclude the article by giving an overview of potential improvements to the algorithm.

4.2. Origin and Characteristics of Phase Synchronization Error in Bistatic SAR

4.2.1. Where Does The Error Come From?

The separation of transmitter and receiver inherent in bistatic systems leads to the need for three different types of synchronization [73]:

1. Time or reception window synchronization: The reception window of the receiver must align or include the transmission window of the transmitter for the duration of the acquisition.
2. Beam synchronization: The transmit and receive antennas must illuminate the same region on the ground at the same time.
3. Phase synchronization: The difference in the instantaneous phases of the oscillators in the transmitter and the receiver must be minimized.

The algorithm of this article tackles 3). Bistatic SARs have spatially separate transmitter and receivers. Therefore, each receiver has its own oscillator with an independent instantaneous phase. The instantaneous phase of the ith receiver is [65, 74]

$$\psi_i(t) = 2\pi \int_{\tau_0}^{t} f_i(\tau)\,\mathrm{d}\tau + \phi_{i,0}, \tag{4.1}$$

where τ_0 is the initial time offset, $\{f_i(t), t \geq 0\}$ is a stochastic process representing the instantaneous frequency of the ith oscillator, and $\phi_{i,0}$ is a constant phase offset. f_i is the sum of the oscillator's central frequency, $f_{i,c}$, and a zero-mean stochastic process representing deviations from the central frequency, $\{\delta f_i(t), t \geq 0\}$ [69]

$$f_i(t) = f_{i,c} + \delta f_i(t). \tag{4.2}$$

Setting $i = u$ for the first receiver and $i = v$ for the second, we see that each oscillator will introduce a different instantaneous phase during the demodulation of the signals. When two SAR images from different receivers are interfered to form an interferogram, the phase of the first SAR signal is subtracted from that of the second. This operation leaves a phase synchronization error, $\psi_{vu}(t) = \psi_v(t) - \psi_u(t)$, present in the phase of the interferogram. The error remains even when the oscillators have the same central frequency as the deviations from the central frequency are independent processes.

The severity of the phase synchronization error depends on its magnitude relative to the geophysical signal that the instrument is estimating. As an example, consider a single-pass cross-track interferometer with a $30\,\mathrm{m}$ height of ambiguity. A phase synchronization error of 1° translates to an error of $8.3\,\mathrm{cm}$ in the retrieved relative height. For land topography which can have relative heights of meters, such an error might be accommodated. However, for smaller-scale parameters, such as RSSH which spans at most tens of centimeters, such an error would completely degrade the measurement. Thus, the retrieval of smaller-scale geophysical parameters using single-pass bistatic interferometry, such as the retrieval of RSSH by Harmony, requires a refinement of the GNSS-based phase synchronization.

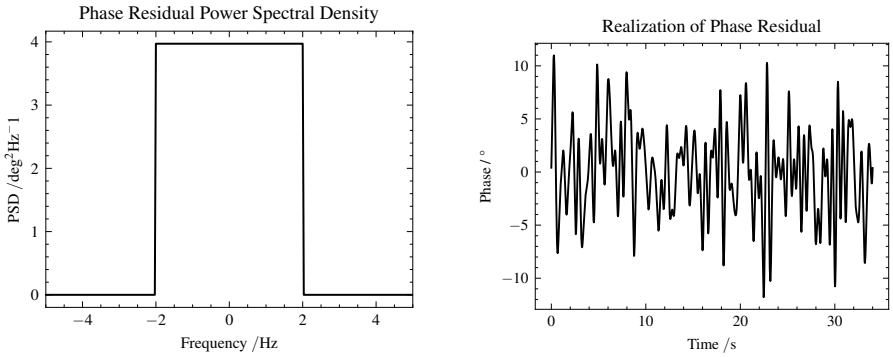

(a) Power spectral density

(b) A realization of the stochastic process

Figure 4.1.: The phase residual after applying the GNSS-based synchronization scheme is a stochastic process characterized by a flat narrowband spectrum.

4.2.2. Post-GNSS Synchronization Phase Residual

In [69] Rodrigues-Silva et al. present a GNSS-based synchronization scheme for multistatic SAR systems such as Harmony. By designing the system to share the oscillator between the satellite's GNSS receiver and the payload, the scheme estimates and corrects the phase synchronization from the combined navigation and precise-orbit determination data. The scheme achieves a residual error after correction with a standard deviation of $1.6°$ at C band. As discussed in 4.2, such a standard deviation is insufficient for retrieval of RSSH.

Before correcting for it, one ought to first characterize the residual error signal after the GNSS synchronization. We model the signal as a stochastic process, $\{\psi_c(t), t \geq 0\}$ with a flat non-zero power spectral density (PSD) between $0\,\mathrm{Hz}$ and f_b, and a zero PSD outside this band

$$S_{\psi_c}(f) = \begin{cases} \dfrac{\sigma^2_{\psi_c}}{2f_b}, & \text{if } -f_b \leq f \leq f_b, \\ 0, & \text{otherwise.} \end{cases} \tag{4.3}$$

The non-zero part of the PSD has a value of $\sigma^2_{\psi_c}/(2f_b)$ and units of $\mathrm{rad}^2/\mathrm{Hz}$, where $\sigma^2_{\psi_c}$ is the variance of the residual phase post-GNSS correction. For the purposes of the simulations in this article, we set $f_b = 2\,\mathrm{Hz}$, $\sigma_{\psi_c} = 4°$. We have arrived at the spectral characterization given by (4.3) after consulting the authors of [69].

We simulate realizations of the residual error that adhere to (4.3) with the following procedure [75]:

1. Discretize the PSD.

2. Convert the discrete PSD to the amplitude of the Discrete Fourier Transform

of ψ_c according to $\sqrt{N f_s S_{\psi_c}[f]}$, where N is the number of points in the discrete PSD, and f_s is the sampling frequency.

3. Assign a random phase to each point of the DFT of ψ_c for $f \geq 0$, sampled from a uniform distribution between 0 and 2π.

4. Set the phase of the negative frequencies of the DFT so that the DFT is even symmetric.

5. Compute the inverse DFT.

Figure 4.1a shows the PSD described by (4.3) and Figure 4.1b shows a realization of the stochastic process that has such a PSD. We have simulated the realization from the PSD according to the procedure we have described in the previous paragraph.

4.3. Calibration Algorithm

The algorithm that we are presenting is designed to work on the interferometric phase residual after the GNSS-based synchronization of [69]. Consequently, the algorithm estimates a realization of the stochastic process described by (4.3) from noisy observations of its finite difference, i.e. approximations of the derivative obtained by the difference of the signal sampled at two different instants of time. We obtain the finite difference via two distinct methods, by computing the differential interferometric phase of the overlap regions, and by computing the differential interferometric phase of subaperture images. We introduce the terms overlap regions, and subapertures images in the following two paragraphs.

The algorithm assumes the following: the SAR image has azimuth lines that are sampled twice at different instants of time, not more than a few seconds apart. From here on, we call these azimuth lines "overlap regions". The overlap regions occur periodically at fixed azimuth intervals, as is the case in TOPSAR mode [36]. In TOPSAR, the overlap regions occur whenever the instrument completes a scanning cycle and returns to a given subswath. To ensure that no gaps occur in azimuth between bursts the first azimuth lines of a burst overlap with the last azimuth lines of the preceding burst. These overlap regions are typically not visible in processed SAR images because processors merge bursts by keeping the samples of only the early or the late burst for a given azimuth to create a continuous image.

The algorithm's second source of observations come from subaperture images. SAR processing focuses the echoes that the instrument collects from each scatterer at different time instants, and consequently squint angles, during the illumination time to the correct resolution cell. The length of the synthetic aperture and the instrument's line of sight define the range of squint angles. The raw signal can be focused with a different central squint than that of the instrument, resulting in a SAR image with reduced bandwidth, known as a subaperture image. Several subaperture images can be formed out of a SAR image by focusing the raw signal with different central squints. Each subaperture image contains signal collected during the illumination time by a different part of the full aperture.

A fundamental assumption of the algorithm is that the geophysical signal remains constant during the illumination time, while instrument and platform induced errors vary continuously. Hence, by comparing the signal from different subaperture images, the instrument, and platform errors can be estimated. This technique is known as multisquint processing [76], and it has been used to correct for residual motion errors [70], estimate the azimuth motion of glaciers [71], and it has been proposed to synchronize the phase of tomographic acquisitions[72].

The heart of the algorithm lies in leveraging the variance and invariance of the synchronization residual and the topographic phase, respectively, between interferograms of adjacent subapertures and overlap regions. We model the interferometric phase of the interferogram between the ith subapertures as

$$\phi_i(t,\tau) = \phi_t(t,\tau) + \phi_m(t_{c,i},\tau) + \psi_c(t_{c,i}) + n_i(t,\tau), \tag{4.4}$$

where t represents the slow time corresponding to an azimuth position in the focused image, $t_{c,i}$ represent the azimuth beam-center time of the ith subaperture, and τ is the range (fast) time. ϕ_i has several components, the topographic component ϕ_t, in the case that there is an along-track baseline between the SAR acquisitions a motion component ϕ_m, the synchronization residual ψ_c, and noise n_i.

We explicitly include the subaperture index i as subscript to highlight the assumption that the topographic phase stays constant in each subaperture, while the other phase contributions change with subaperture. Furthermore, we have assumed that the residual ψ_c does not vary with range because for a given azimuth position, samples are collected over the swath width in fractions of a millisecond, a time interval that is much shorter than the period of the highest frequency component of ψ_c.

The beam-center time of the ith subaperture is

$$t_{c,i} = t - \frac{T_a}{2} + \frac{T_a}{N}\left(i - \frac{1}{2}\right), \tag{4.5}$$

where T_a is the aperture time, and N is the number of subapertures [77]. Thus, the interferograms from different subapertures capture the phase synchronization residual at different time instants. Furthermore, the interferometric phase due to the motion of the surface also changes between the subapertures. The phase due to motion, also known as the along-track interferometric (ATI) phase is[49]

$$\phi_m = \frac{2\pi B_{\parallel}}{\lambda v_p}\mathbf{v_s}\cdot\hat{\mathbf{l}}_\mathbf{i} \tag{4.6}$$

where $B_{\parallel}$ is the effective along-track baseline of the interferometer, v_p is the velocity of the platform, v_s is the vector representing the velocity of the surface, and $\hat{\mathbf{l}}$ is a unit vector parallel to the instrument's line of sight. Since each pair of subaperture images corresponds to processing the signal with a different central squint, $\hat{\mathbf{l}}$ changes for each subaperture. The line of sight unit vector of the ith subaperture

is

$$\hat{\mathbf{l}}_\mathbf{i} = \begin{pmatrix} \sin(\eta + \eta_i) \\ \cos(\eta + \eta_i)\sin\theta \end{pmatrix}, \tag{4.7}$$

where η is the squint of the line of sight, $\eta_i = -\frac{\beta}{2} + \frac{\beta}{N}(i - \frac{1}{2})$ is the squint offset with respect to η of ith subaperture, and β is the instrument's azimuth beamwidth.

The phase of the differential interferogram between the interferogram of subaperture images i and that of subaperture images $i+1$, which we call the spectral diversity phase [70], is given by the following equation:

$$\Delta\phi_i(t,\tau) = \phi_m(t_{c,i+1},\tau) - \phi_m(t_c,\tau) + \psi_c(t_{c,i+1}) - \psi_c(t_{c,i}) + n_{i+1}(t,\tau) - n_i(t,\tau). \tag{4.8}$$

Equation (4.8) shows that the topographic phase cancels out in the differential interferogram. The phase due to motion, however, does not as it depends on the look direction which changes with subaperture. Thus, if the cross-track interferometer has an effective along-track baseline, which is unavoidable in formation-flying systems, the spectral diversity phase will have a motion component, a residual synchronization component, and noise.

The motion component of the spectral diversity phase is [78]

$$\begin{aligned} \Delta\phi_{m,i}(t,\tau) &= \frac{2\pi B_\parallel}{\lambda v_p} 2\sin\frac{\beta}{N}\big(-2s_\rho\sin(\eta+m_i) \\ &\qquad + 2s_a\cos(\eta+m_i)\big), \end{aligned} \tag{4.9}$$

$$= \frac{2\pi B_\parallel}{\lambda v_p} 2\sin\left(\frac{\beta}{N}\right)\mathbf{v_s}\cdot\hat{\mathbf{x}}_\mathbf{i}, \tag{4.10}$$

where $m_i = \beta(-1/2 + i/N)$, $\eta + m_i$ is the mean squint of the subapertures used to form the spectral diversity phase, and $\hat{\mathbf{x}}_\mathbf{i} = (\cos(\eta+m_i), -\sin(\eta+m_i))^T$ is the azimuth direction defined by m_i. We have identified the term inside the brackets in (4.9) as the projection of the velocity vector on the mean azimuth direction of the subapertures that form the differential interferogram. Therefore, the spectral diversity phase of adjacent subapertures is directly proportional to the motion in the mean azimuth direction. Importantly, for N subapertures, one can form $N-1$ spectral diversity phases and each will have an azimuth motion component. The mean azimuth direction rotates in increments of $\frac{\beta}{N}$ between successive subaperture pairs.

Spectral diversity techniques, including multisquint processing, assume that no geophysical signal is present in the spectral diversity phase. Thus, they treat the spectral diversity phase as an estimate of the derivative of azimuth errors. The integral of the spectral diversity phase yields an estimate of the azimuth error, which they use to correct the interferograms. The assumption is valid in scenes where the surface is static in the time between the SAR acquisitions, which is the case over land. From (4.10), we can tell that this assumption is invalid for dynamic surfaces, such as the ocean.

Consequently, we need to remove the azimuth motion component from the spectral diversity phase before using it to estimate the phase synchronization residual. The Harmony satellites feature an antenna that has a fore and an aft phase center. Each satellite forms two SAR images from the signals received by the fore and aft phase centers. We will refer to these as the individual phase center (IPC) images. They then combine the signals received by these phase centers to create an improved SAR image that we will call the combined phase center (CPC) image.

The phase centers are separated along the longitudinal axis of the antenna, thus having an effective along-track baseline. Therefore, we can perform along-track interferometry with the SAR images from the individual phase centers to estimate the ATI phase. By scaling the estimate by the ratio of the effective along-track baseline of the formation to the along-track baseline of the on-board phase centers, we can compute the ATI phase of the CPC interferogram. Once we have an estimate of ϕ_m we can subtract it from the phase of the interferogram[62]. Then, the subaperture-dependent motion component will be eliminated from the spectral diversity phase and (4.8) will only include the synchronization residual term and noise. Figure 4.2 shows a flowchart of the interferogram generation, including the correction of the ATI phase.

The ATI phase estimate from the IPCs will have an error with respect to the true ATI phase that is determined by the coherence of the IPC SAR images. Scaling the ATI phase and subtracting it from the interferometric phase of the CPCs will increase the noise of the interferometric phase. Therefore, removing the bias due to surface motion comes at the cost of making the interferometric, and by extension the spectral diversity, phase noisier.

4.3.1. Phase Synchronization using Multisquint Processing

Once the subaperture interferograms have been cleaned from the phase due to motion, the spectral diversity phase becomes

$$\Delta\phi_i(t,\tau) = \psi_c(t_{c,i+1}) - \psi_c(t_{c,i}) + n_{\mathrm{sd},i}(t,\tau), \tag{4.11}$$

where $n_{\mathrm{sd},i}$ represents the noise of the spectral diversity phase. $n_{\mathrm{sd},i}$ includes the error from the subaperture interferogram and the error of the ATI phase correction. Hence, we can now treat the spectral diversity phase as the finite difference of the synchronization residual and apply an adaptation of Enhanced Multisquint Processing [70].

We can convert the finite difference of the residual to the derivative by dividing $\Delta\phi_i$ by the temporal separation of adjacent subapertures $\Delta t = T_a/N$. The fraction of the aperture time used to form each subaperture determines the quality of the derivative. The SAR produces the phase synchronization residual by integrating the synchronization error weighted by the azimuth envelope along the aperture. Therefore, a smaller subaperture captures the high frequency components of the residual and leads to a better estimate. On the other hand, longer subapertures use more of the azimuth bandwidth, leading to less noise.

Using multiple subapertures and then coherently combining them as per Multisquint Processing, combines the benefit of short aperture times while making use

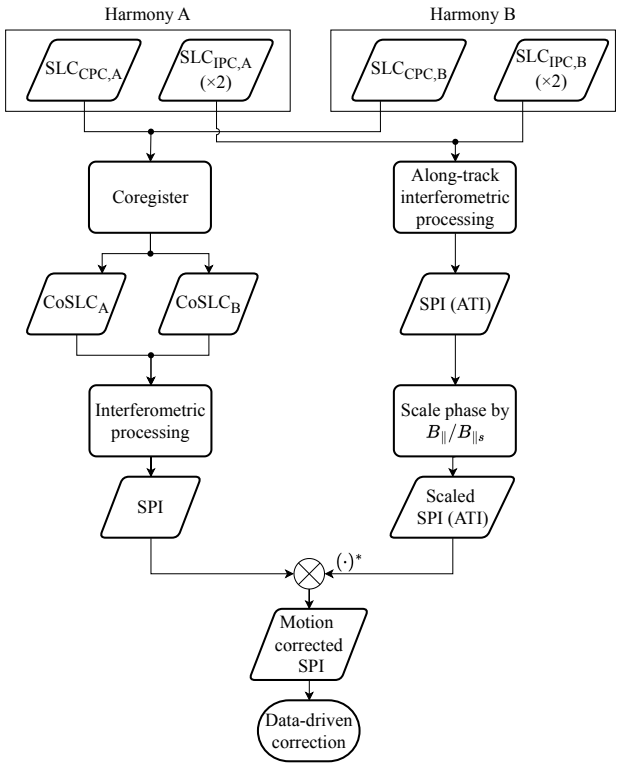

Figure 4.2.: High-level flowchart of the Harmony single-pass interferogram generation, including the removal of the ATI phase. $\mathrm{SLC}_{\mathrm{CPC,i}}$ stands for the SLC image of the combined phase center, and $\mathrm{SLC}_{\mathrm{IPC,i}}$ represents the SLC image of the individual phase centers coming from the wing antennas of each Harmony companion, where subscript i can be A or B to refer to the first or second companion respectively. $\mathrm{CoSLC_i}$ refers to the coregistered SLC image, SPI is the single-pass interferogram, $B_{\parallel}$ is the interferometric along-track baseline of the satellite formation, and $B_{\parallel s}$ is the along-track baseline of the fore and aft phase centers. In the diagram, the $\times 2$ annotation next to the $\mathrm{SLC}_{\mathrm{IPC,i}}$ highlights that each companion produces two SLC images from the two wing phase centers, and the along-track interferometric processing involves the creation of an interferogram from two independent pairs of SLC images.

of all the available bandwidth. Thus, we produce N subapertures, from which we create $N-1$ spectral diversity phases. Each spectral diversity phase samples the

finite difference of the interferogram phases at

$$t_{\mathrm{sd},i} = t_{c,i} + \frac{T_a}{2N}. \tag{4.12}$$

As a result, to average the spectral diversity phases, we first need to resample them to the sampling times of the full aperture interferogram. The averaged spectral diversity phase is

$$\Delta\phi(t) = \frac{1}{N-1} \sum_{i=1}^{N-1} \sum_{k=0}^{M-1} \mathrm{sinc}\left(\frac{t - t_{\mathrm{sd},i}[0] - kT}{T}\right) \Delta\phi_i[k], \tag{4.13}$$

where $\Delta\phi_i[k]$ represents the kth sample of the ith spectral diversity phase. The square brackets denote a discrete-time signal $\Delta\phi_i[t] \coloneqq \Delta\phi_i(t_{sd,i}[0] + kT)$ with $T = 1/f_s$ where T is the sampling period and f_s the sampling frequency. Using the same notation, $t_{\mathrm{sd},i,}[0]$ is the initial value of the ith spectral diversity slow time. Finally, M is the number of samples per subaperture.

Taking the mean value of the average spectral diversity phase over range, and dividing by the temporal separation of adjacent subapertures, Δt, yields an estimate of the derivative of the synchronization residual at t,

$$\hat{\psi_c}'(t) = \frac{\mathbb{E}_\tau\left[\Delta\phi(t,\tau)\right]}{\Delta t}, \tag{4.14}$$

where $\mathbb{E}_\tau$ is the expectation operator over range.

Moreover, the differential interferogram between two full-aperture interferograms at the overlap regions measures the finite difference of the synchronization residual, $\Delta\psi_c$, at the azimuths that fall within these regions. The measurements from the overlap regions have less noise than the derivatives obtained using the multisquint method, as they use the full bandwidth of the signal. Thus, these measurements are expected to be more accurate. Finally, since the time difference between the samples of the overlap regions is larger than the difference between adjacent subapertures, the overlap difference constrains the estimate of ψ_c.

To sum up, we have the following two sets of observations:

1. The multisquint-based derivative of the synchronization residual at each instant of sensing time.

2. The difference of the synchronization residual at the overlap regions from the full-bandwidth differential interferogram.

To estimate the synchronization residual from these observations we formulate

the problem as a linear system

$$\begin{pmatrix} \hat{\psi_c}'[0] \\ \hat{\psi_c}'[1] \\ \vdots \\ \hat{\psi_c}'[N-2] \\ \Delta\psi_{co}[0] \\ \vdots \\ \Delta\psi_{co}[K-1] \\ 0 \end{pmatrix} = \begin{pmatrix} \mathbf{\Delta} \\ \mathbf{O} \\ \mathbf{J_{1,N}}/N \end{pmatrix} \begin{pmatrix} \psi_c[0] \\ \psi_c[1] \\ \vdots \\ \psi_c[N-1] \end{pmatrix}. \tag{4.15}$$

$\psi_c[n]$ represents the nth sample of the synchronization residual and the square brackets denote a discrete-time signal $\psi_c[n] \coloneqq \psi_c(nT)$ with $T = 1/f_s$ where T is the sampling period and f_s the sampling frequency. $\Delta\psi_{co}[n]$ is the nth sample of the signal's finite difference at the overlap regions. $\mathbf{\Delta}$ is an $(N-1) \times N$ matrix, $\mathbf{O}$ is a $K \times N$ matrix, and $\mathbf{J_{1,N}}$ is the $1 \times N$ unit matrix. Together they form the system's design matrix. The three matrices are defined as follows:

$$\mathbf{\Delta} = \operatorname{diag}(\mathbf{\Delta t}) \begin{pmatrix} 1 & -1 & 0 & \dots & 0 \\ 0 & 1 & -1 & \dots & 0 \\ 0 & 0 & 1 & \dots & 0 \\ \vdots & \vdots & \ddots & \ddots & \vdots \\ 0 & 0 & \cdots & 1 & -1 \end{pmatrix} \tag{4.16}$$

$$\mathbf{O}_{i,j} = \begin{cases} 1, & \text{if } j \text{ is the early sample of the ith overlap,} \\ -1, & \text{if } j \text{ is the late sample of the ith overlap,} \\ 0, & \text{otherwise,} \end{cases} \tag{4.17}$$

$$\mathbf{J_{1,N}}_k = 1 \tag{4.18}$$

for $k = 1, 2, \dots, N$. We use $\mathbf{J_{1,N}}$ to provide an additional equation to the system, postulating that the mean value of the residual is $0°$. The vector $\mathbf{\Delta t}$ of length $N-1$ represents the temporal separation between subapertures. Since each subswath has a different aperture time, the vector takes values $1/\Delta t_1$, $1/\Delta t_2$, and $1/\Delta t_3$ for the subaperture separation of the first, second, third subswath respectively,

$$\mathbf{\Delta t}_i = \begin{cases} \dfrac{1}{\Delta t_1}, & \text{if the ith sample comes from subswath 1,} \\ \dfrac{1}{\Delta t_2}, & \text{if the ith sample comes from subswath 2,} \\ \dfrac{1}{\Delta t_3}, & \text{if the ith sample comes from subswath 3.} \end{cases} \tag{4.19}$$

Equation (4.15) describes an overdetermined system of equations with N parameters and $N + K$ observations. We estimate the parameters by inverting the

system using weighted least squares (WLS) and setting the weights to the inverse of the variance of the observations. We define the weight matrix as follows:

$$\mathbf{W} = \operatorname{diag}\big(\sigma_{sd}[0]^{-2}, \ldots, \sigma_{sd}[N-2]^{-2}, \sigma_0[0]^{-2}, \ldots, \sigma_0[K-1]^{-2}, (100 \max \sigma_{sd})^{-2}\big), \quad (4.20)$$

where the standard deviation of the spectral diversity derivative of the phase, ψ_c' relates to the standard deviation of the subaperture phase, according to

$$\sigma_{sd}[i] = \frac{\sqrt{2}}{\sqrt{N-1}\boldsymbol{\Delta}\mathbf{t}_i}\sigma_{\text{sub}}[i]. \quad (4.21)$$

σ_{sub} is the standard deviation of the subaperture phase. We use the Cramer-Rao lower bound (CRLB) of interferometric phase and the ratio of the subaperture bandwidth, B_{sub}, to the full-aperture bandwidth, B_a, to define σ_{sub} [25]

$$\sigma_{\text{sub}} = \sqrt{\frac{1-\gamma^2}{2N_L\gamma^2}\frac{B_a}{B_{\text{sub}}}}, \quad (4.22)$$

where γ is the interferometric coherence, and N_L is the number of looks. The standard deviation of the differential phase at the overlap regions is given by

$$\sigma_0[i] = \sqrt{\sigma_{\psi_c}[l_i]^2 + \sigma_{\psi_c}[k_i]^2}, \quad (4.23)$$

where l_i is the late sample of the ith overlap, and k_i is the early sample of the ith overlap. We set the weight of the prior to correspond to a variance that is larger than the maximum variance of the observations. The reason for this is that we want the algorithm to give more weight to the observations than the prior assumption.

4.4. Simulations and Results

4.4.1. Simulations

To assess the performance of the algorithm, we simulate the multilooked interferometric phase that Harmony in its XTI phase would produce. We break down the simulation into three components:

1. We use coupled ocean-atmosphere models to model an oceanic scene. The variables of interest include RSSH, surface current vector, wind vector, and two-directional wave spectrum.

2. We pass the outputs of the ocean-atmosphere model to Harmony's scientific workbench, and run the forward to chain to produce multilooked normalized radar cross-section (NRCS) over the scene.

3. We feed the scene observables and the NRCS into Harmony's XTI performance model [62] to estimate the height of ambiguity and the standard deviation of the interferometric phase.

Once we have the results from these three operations, we can construct synthetic images of the multilooked interferometric phase. We do so by constructing the TOPSAR sensing timeline. We break the interferogram into bursts and assign a sensing time to each azimuth line within each burst. We simulate the burst overlaps by repeating the last azimuth lines of the current burst at the first azimuth lines of the next burst for each subswath. The repeated azimuth lines of the overlaps have non-overlapping sensing times that are separated by the cycle time of the TOPSAR mode.

We assign a phase to each resolution cell of the interferogram by taking the height from the RSSH of the model, converting it to a phase using the height of ambiguity of the cell, and adding noise to it according to the CRLB. Additionally, we generate a realization of the synchronization residual as described in Section 4.2.2 and then resample it to the sensing times of the interferogram cells. Since each azimuth line of each subswath, including the lines of the overlapping regions, has its own sensing time, a different phase synchronization residual is assigned to each cell even if they are spatially overlapping.

Once we have the interferometric phase and the phase synchronization residual of each cell, we proceed with simulating the subapertures. For each azimuth line, we interpolate the synchronization residual to N different times according to (4.5). We then add noise, which we model as a zero-mean Gaussian with a standard deviation given by (4.22), to each of the subaperture phases. Next, we form $N-1$ spectral diversity phases by subtracting adjacent subapertures from one another as per (4.11), and then we coherently average them as described in (4.13).

With the averaged spectral diversity phase computed, we proceed with converting the spectral diversity phases into derivatives by dividing each sample by Δt_i, and averaging in range. Furthermore, we compute the overlap differential phases by finding the difference in interferometric phase at the overlap regions. Finally, we form the linear system of (4.15), define $\mathbf{W}$ using the standard deviation of each cell computed by the performance model, and solve for ψ_c.

4.4.2. Results

We simulate an interferometric acquisition of Harmony over the ocean and in particular over the coast of France. We use numerical model data from the MARC project [79–81] which uses Ifremer's MARS 2D[82], 3D [83] models, and the WAVEWATCH III model [84]. After taking the wind, current, and wave spectra from the data, we resample them to a common $1\,\mathrm{km} \times 1\,\mathrm{km}$ grid, and cut a $250\,\mathrm{km} \times 255\,\mathrm{km}$ slice in range and azimuth, respectively, to use as the acquisition. Figure 4.3 shows the wind, current, significant wave height, and sea-surface height anomaly predicted by the MARC project on 2024-01-01 at midnight, while Figure 4.4 illustrates the directional wave spectrum from WAVEWATCH III.

The region that is used to simulate a Harmony acquisition is enclosed within a

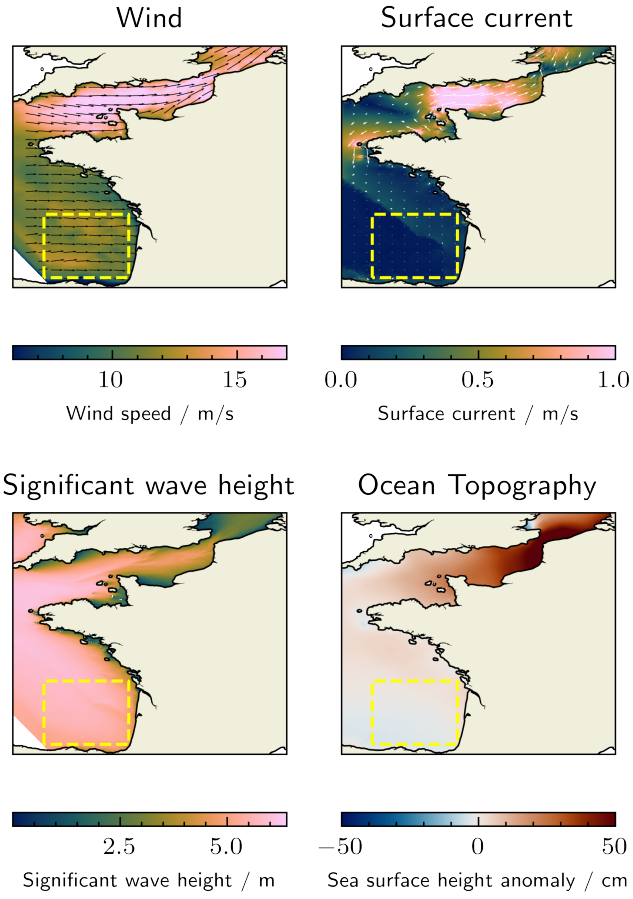

Figure 4.3.: Outputs from ocean-atmosphere coupled model. Clockwise from top left: Stress-equivalent wind; Surface current; Significant wave height; Sea-surface height anomaly. The area used for the simulated Harmony acquisition is indicated by the dashed yellow rectangle.

yellow dashed rectangle. The area shows medium wind and weak current, which will produce a medium signal-to-noise ratio. We note to the reader that the model provides the sea-surface height anomaly, i.e. the height relative to the temporal mean of the sea-surface height at a given location. In our simulations, we use this model output as the RSSH. The two quantities have similar dynamic range over the same spatial scales; thus, the anomaly serves as a realistic simulation of the RSSH. The height anomaly in the region is weak, varying between $-4\,\mathrm{cm}$ to $4\,\mathrm{cm}$. Thus, the scene will be a stress test for both the calibration algorithm and the performance of the instrument (expected accuracy in medium wind of approximately $5\,\mathrm{cm}$).

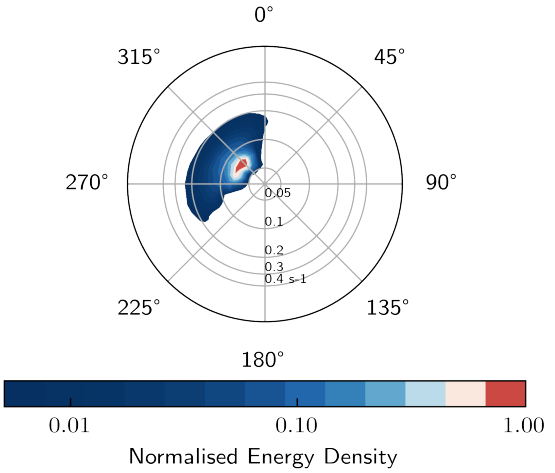

Figure 4.4.: Directional wave spectrum from WAVEWATCH III model.

Collecting the data that Figures 4.3 and 4.4 illustrate corresponds to step 1 of the preprocessing components outlined in section 4.4.1. After completing the remaining steps, we form full- and subaperture images of the interferometric phase and run the algorithm on them. We also run a simplified version of the algorithm that does not use the overlap regions. This simplification corresponds to dropping the samples $\Delta\psi_{co}[0], \ldots, \Delta\psi_{co}[K-1]$ from the observations vector on the left-hand side of (4.15), and $\mathbf{O}$ from the right-hand side of (4.15).

The top panel of Figure 4.5 shows the true RSSH within the acquisition. The field corresponds to the yellow rectangle in the bottom right panel of Figure 4.3. The bottom panel of Figure 4.5 shows the height that Harmony would retrieve without calibration, and with taking the measurement noise into account. There are gaps at the top and the bottom of the three subswaths due to the TOPSAR operation.

Figure 4.6 illustrates the retrieved height after running the calibration algorithm. The top panel shows the result after calibrating without taking advantage of the information at the overlap regions, while the bottom panel shows the result after calibrating with the information at the overlap regions. We illustrate the error between the synchronization residual estimated with the overlaps and the true synchronization residual in Figure 4.7.

The error between the true and estimated signal provides a metric on the performance of the algorithm. However, it lacks information on the spatial dependence of the algorithm performance. We use the semivariogram [85] to assess the spatial dependence of uncalibrated and calibrated signals. We compute the directional semivariograms of the uncalibrated noisy RSSH, i.e. the signal shown in the bottom panel of Figure 4.5. Figure 4.8 shows the semivariogram in the range

direction, and Figure 4.9 shows the semivariogram in the azimuth direction. The top panels of the figures show the histograms of the lag classes used for the experimental semivariograms and the green lines in the bottom panels show a Gaussian model fitted to the data.

Figure 4.10 illustrates a more realistic result. The figure presents the retrieved calibrated height with measurement noise. The measurement has been processed with a Gaussian filter to a resolution of $5\,\mathrm{km} \times 5\,\mathrm{km}$. Figures 4.11 and 4.12 illustrate the directional semivariograms of the corrected RSSH, prior to filtering, in the range and azimuth directions, respectively. We have computed the semivariograms with the Matheron estimator [86], and we have set the maximum lag to not exceed half the extent of the scene [87].

4.5. Discussion

4.5.1. Data-driven Calibration

The top panel of Figure 4.5 introduces the geophysical signal that the interferometer will retrieve. The signal varies from $-4\,\mathrm{cm}$ in the southwest corner of the scene to $4\,\mathrm{cm}$ in the northeast. A prominent front features along the northwest to southeast axis where the height anomaly goes through $0\,\mathrm{m}$.

The bottom panel paints a somber picture and demonstrates the crux of the issue. The post-GNSS phase sync residual dominates the signal and removes the geophysical signature of the signal. The measurement noise is also visible in the figure, particularly at the edges of the subswaths where the NESZ deteriorates. Nevertheless, the noise is not as dominant as the horizontal stripe-like pattern imposed on the data by the phase synchronization residual. This illustrates our earlier assertion that the phase-sync residual, left uncalibrated, will dominate the error budget. Furthermore, it makes clear the need for a calibration of the phase sync residual.

The retrieved heights shown in Figure 4.6 demonstrate that the proposed algorithm successfully estimates and removes most of the phase synchronization residual. The top panel illustrates that calibrating the signal without using the overlaps removes the majority of the synchronization residual. Artifacts are visible particularly near burst boundaries. The lack of sampling of the residual difference between TOPSAR cycles likely causes these artifacts. Taking advantage of the differential phase at the burst overlaps enhances the calibration and removes the block-shaped artifacts, as shown in the bottom panel of Figure 4.6.

The observant reader will notice that the corrected signal is more positive than the true RSSH. This is noticeable particularly at the southeast corner, where the corrected signal has a lighter blue color in Figure 4.6 than in the top panel of Figure 4.5. The shift is due to the unknown integration constant that cannot be estimated from the derivatives of the signal. The last line of (4.15) essentially postulates that the integration constant equals zero, yet this not true. This prior assumption causes the estimator to under- or overestimate the synchronization residual at all times. In cases where the synchronization residual has a positive DC term, the estimator will underestimate the signal while when the residual has a negative DC

term, the estimator will overestimate it as it will always push the estimate towards $0°$. Figure 4.7 demonstrates this shift. The error fluctuates about $0.044°$ which is the mean value of the synchronization residual.

Despite the shift, the estimator follows the true signal and provides an estimate that tracks the high- and low-frequency variations of the synchronization residual. Given that a cross-track interferometer estimates the relative height of the surface, a constant shift becomes a bias that does not affect the relative height error. The calibration accuracy in terms of the root mean squared error (RMSE) is $0.046°$ when the algorithm with the overlaps is used, and it deteriorates to $0.062°$ when the overlaps are neglected. The constant shift dominates the RMSE. To assess the ability of the calibration to capture the fluctuations of the synchronization residual, we compute the RMSE after removing the mean of the residual from it. Then, RMSE drops to $0.010°$ and $0.043°$ for the calibration with the overlaps and without them, respectively. The error budget for Harmony's RSSH estimate sets the upper bound of the phase synchronization error to $0.06°$. Thus, the calibration algorithm meets the requirement.

We highlight to the reader that the calibrated heights in Figure 4.6 are fictitious and not a realistic representation of the calibrated RSSH product. They are fictitious because they do not include any errors, random or systematic, other than the residual from the phase synchronization error that the calibration fails to remove. Such a result would never be visible in the real data, as it would be impossible to remove the measurement noise. However, we are choosing to show the results in this manner to highlight the effect of the calibration without any other factors impacting the visualization of the results. Furthermore, we note to the reader that while the measurement noise is removed from the data for the purposes of visualization, the calibration is run with noisy observations in accordance with the phase model of (4.11) and the statistics defined in (4.21).

In addition to the estimate error shown in Figure 4.7, and the RMSE which provide global metrics of the algorithm's performance, we use the semivariograms of the signal prior to, and post calibration to study the algorithm in terms of spatial lag. Before discussing the features of the directional semivariograms in Figures 4.8 and 4.9, we note that since the synchronization residual dominates the retrieved signal before calibration, the semivariograms describe the statistical properties of the residual. We have verified this finding by computing the directional semivariograms of the synchronization residual and confirming that they closely match those of the uncalibrated noisy signal.

The directional semivariograms in Figures 4.8 and 4.9 show that the principal direction of continuity of the uncalibrated signal is ground range. We can readily confirm this by looking at the retrieved RSSH before calibration in the bottom panel of Figure 4.5, where we see the synchronization residual producing horizontal stripes within each subswath. The range of spatial correlation is $117\,\mathrm{km}$ in the ground range direction, and $7.5\,\mathrm{km}$ in the azimuth direction. The strong anisotropy is because the sync residual is a 1D signal in time that is mapped to two dimensions by the operation of the instrument and formation of the image. Within a burst, the signal varies only with azimuth, or equivalently sensing time.

The switching of the instrument between different subswaths introduces a ground range dependence[36] to the synchronization residual, while the cycle time between adjacent bursts introduces discontinuities in azimuth.

In Figure 4.10 we take the result of calibrating the RSSH with the overlap regions, and we add the measurement noise back, as predicted by the XTI model. We then filter the result to a $5\,\mathrm{km} \times 5\,\mathrm{km}$ resolution to reduce the noise, at the cost of reducing the resolution by a factor of 5 in each dimension. It is striking that the pre-calibration synchronization error dominated signal becomes a noise-limited signal post-calibration. In terms of calibration, this is a positive result as it shows that retrieving the geospatial signal is possible, despite the synchronization residual dominating the error budget of the signal. Finally, the result reveals that the RSSH of this scene lies at the edge of the interferometric performance of the instrument, in line with our expectations.

Figures 4.11 and 4.12 show that the spatial dependence of the calibrated RSSH are significantly different from those before the calibration. The variance in both directions shows an order of magnitude decrease. The ground-range semivariogram shows spatial independence, consistent with the white noise that dominated the calibrated RSSH before filtering, up to lags of $60\,\mathrm{km}$ and an upwards trend for larger lags. The trend is likely due to the increasing variance of the measurement error at the mid- to far range. The azimuth semivariogram shows spatial independence for all lags. We postulate that this is because the noise dominates the signal, making the geophysical signature not visible, and because the dependence of the noise's variance on azimuth is weak. Importantly, the signature of the synchronization residual is missing in both directions at all lags.

4.5.2. Calibration Errors

During our simulations of the acquisition timeline and the calibration algorithm, we have arrived at the conclusion that there are two effects that can cause errors in the calibration. The first effect is due to the incorrect azimuth positioning of scatterers caused by their radial motion [88]. If the translation of scatterers in the averaged spectral diversity phase is the same as the translation in the interferogram, then the estimated phase that will be applied to the interferogram to correct the synchronization residual will also have the same translation, and the calibration will not be affected. In cases, however, where the motion of the scatterers lead to different translations in each subaperture, the spectral diversity phases will be offset with respect to one another. The sensing time assigned to each subaperture will be wrong by different amounts, leading to misaligned averaging and estimation errors.

We recommend two potential solutions to this error. The first solution is to form the subapertures from the raw data, then focus to obtain subaperture SAR images, rather than running the algorithm on subapertures formed from the focused SAR images. Thus, each subaperture will have the correct sensing time, and resampling and averaging can be done without errors. The second solution is to use the Doppler of the subapertures to estimate the velocity and the azimuth

translation due to the radial motion of the scatterers. We can then use the estimate to correct for the misregistration, prior to calibrating.

The second error comes from insufficient sampling of the synchronization residual's derivative. The insufficient sampling occurs when the subaperture duration is not an integral multiple of the sampling period in azimuth. This condition can be readily derived from (4.5). For the sampling of the derivative to have no gaps, the kth sample of subaperture $i+1$ must coincide in time with the $k+n$th sample of the ith subaperture. Setting $t_{c,i}[k+n]$ equal to $t_{c,i+1}[k]$ and solving for the sampling period gives

$$T = \frac{T_a}{nN}, \tag{4.24}$$

where T_a/N is the subaperture integration time, and n is the offset in samples before the sensing times coincide.

In cases where (4.24) does not hold, the interval over which the algorithm computes the finite phase difference is smaller than the step between consecutive samples of the derivative. This leads to gaps in the sampling of the derivative, which cause estimation errors. As the estimator performs an integration step, these errors accumulate. Our simulations confirm that the estimation errors scale with the variance of the synchronization residual. Thus, it is beneficial to match the subaperture integration time to, or a multiple of, the sampling period of the derivative. Practically, this is difficult to achieve because of the bursts produced by TOPSAR, and because of the antenna weighting which would tend to weigh subaperture samples differently, changing the effective sensing times.

4.6. Conclusion

We have presented an algorithm to remove the phase-synchronization residual that remains in the bistatic SAR signal of Harmony after the GNSS-based synchronization. The algorithm takes advantage of the periodic sampling overlaps between adjacent bursts in azimuth that occur in TOPSAR to improve the long-term sampling of the residual's derivative. Furthermore, our phase model accounts for the interferometric phase due to the motion of the surface, and we have shown that with a system like Harmony that can produce SAR images from individual phase centers this component of the phase can be estimated and removed.

To assess the validity of the calibration, we have developed a simulation chain that produces acquisitions of the interferometric phase and estimated RSSH from geophysical model outputs describing the scene. The model outputs include wind, currents, directional wave spectra and RSSH. The simulation chain also models realizations of the phase synchronization error according to the power spectral density of the residual. Running the calibration on the simulated acquisitions shows that we can remove the effect of the synchronization residual and estimate the RSSH. The calibration achieves a root-mean-square error of $0.046°$, which satisfies the limit for the phase synchronization error needed for Harmony to retrieve submesoscale RSSH.

In the future, we plan to improve on the calibration algorithm by estimator. We can derive the autocorrelation length from the PSD of the phase synchronization residual. The autocorrelation of the derivative can then be incorporated in the estimator by using a Wiener filter to reduce the noise in the subaperture phase prior to running the calibration.

Additionally, we have discussed two sources of error in the calibration. The first error results from the motion of the surface. Since the instrument will be sampling the ocean surface, the surface will have a mean motion. Thus, the radial component of the motion will cause an azimuth misregistration. If the misregistration varies with subaperture, then the sensing times assigned to the spectral diversity derivatives will be wrong, which will lead to an error. Forming the subapertures directly from the raw data, instead of filtering the focused full-aperture data, mitigates this problem. We plan to verify this approach using the Harmony end-to-end simulator. The second error is due to gaps in the sampling of the derivative. The gaps are avoided when the subaperture integration time is an integral multiple of the derivative's sampling period.

Acknowledgment

The authors would like to thank Dr.-Ing. Pau Prats-Iraola and Dr.-Ing. Marc Rodriguez-Cassola for the constructive discussions on the topic.

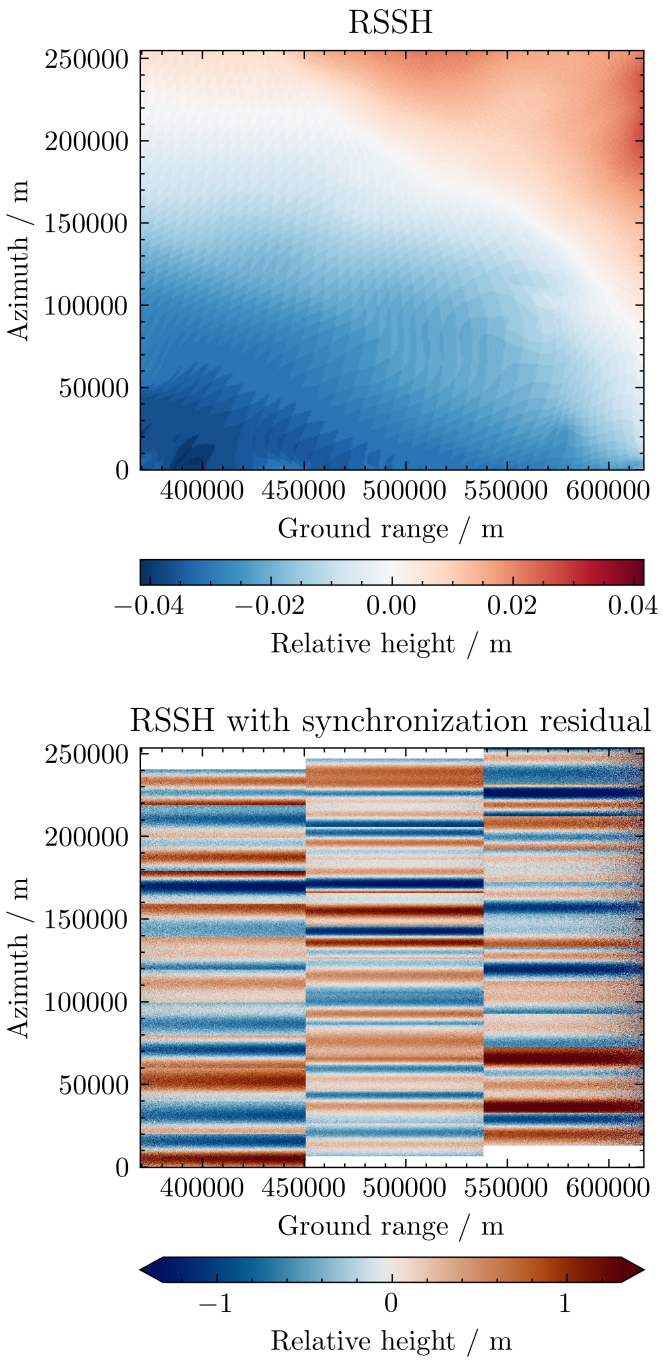

Figure 4.5.: Top: RSSH from the MARS-3D model. Bottom: Retrieved RSSH by Harmony without calibrating for the phase synchronization residual.

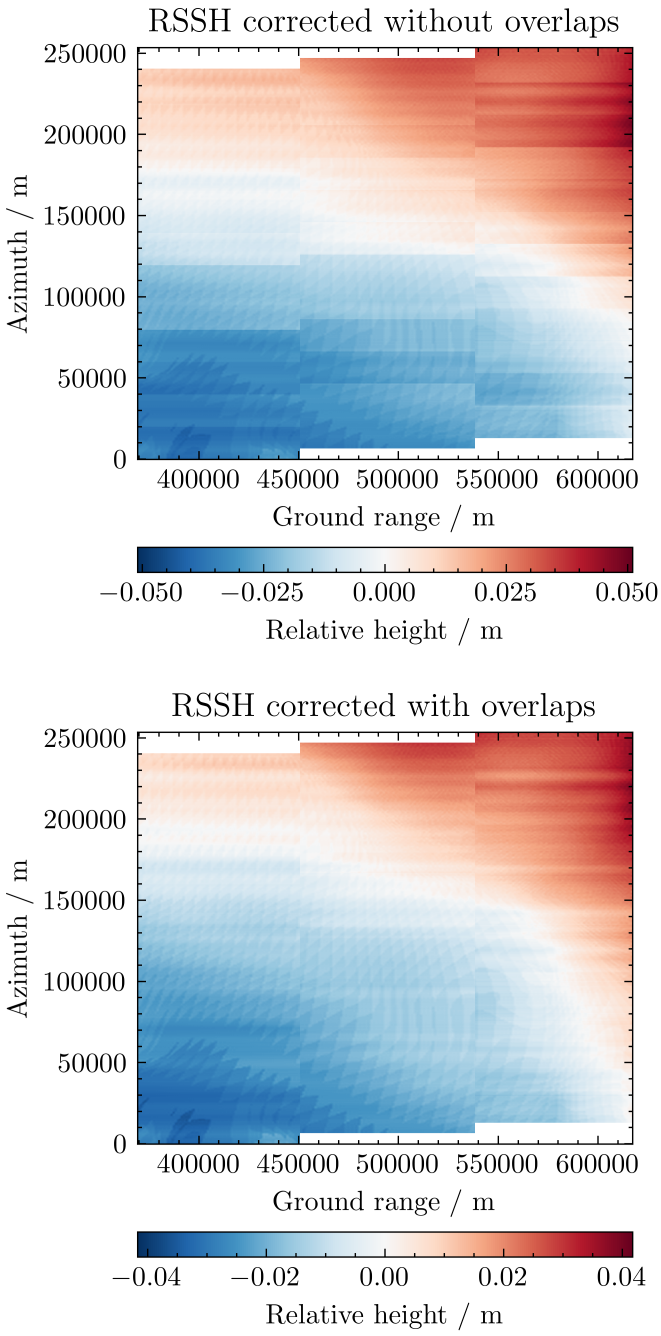

Figure 4.6.: Top: Calibrated retrieved RSSH without using the information in the overlap regions. Bottom: Calibrated retrieved RSSH with the information in the overlap regions.

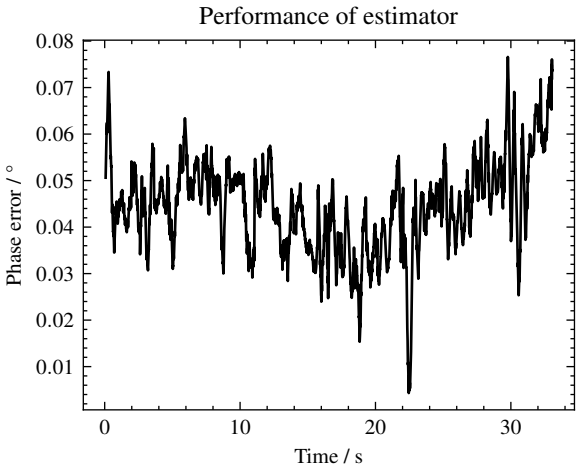

Figure 4.7.: Estimate error between the true phase synchronization residual and the estimated synchronization residual. The error centers about $0.044°$ because of the lack of knowledge of the integration constant during the estimation.

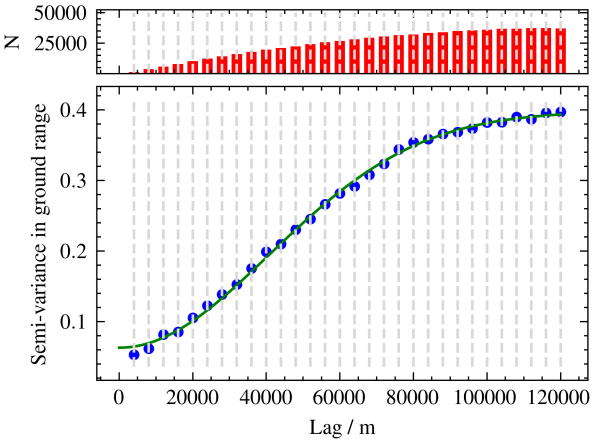

Figure 4.8.: The directional semivariogram of the uncalibrated retrieved RSSH, shown in the bottom panel of Figure 4.5, in the ground range direction. The effective range is $117\,\mathrm{km}$ and binning of the samples used to compute the semivariogram are shown at the top panel.

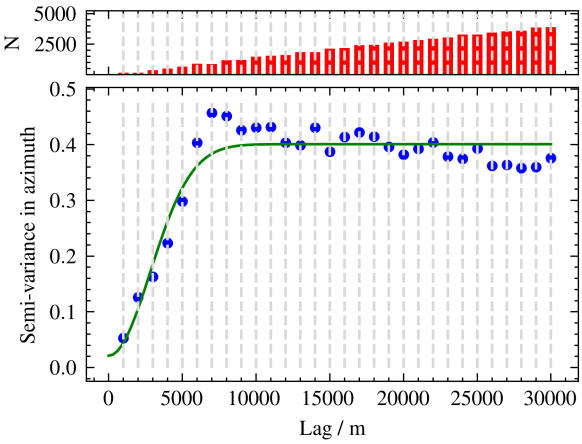

Figure 4.9.: The directional semivariogram of the uncalibrated retrieved RSSH, shown in the bottom panel of Figure 4.5, in the azimuth direction. The effective range is 7.5 km and binning of the samples used to compute the semivariogram are shown at the top panel.

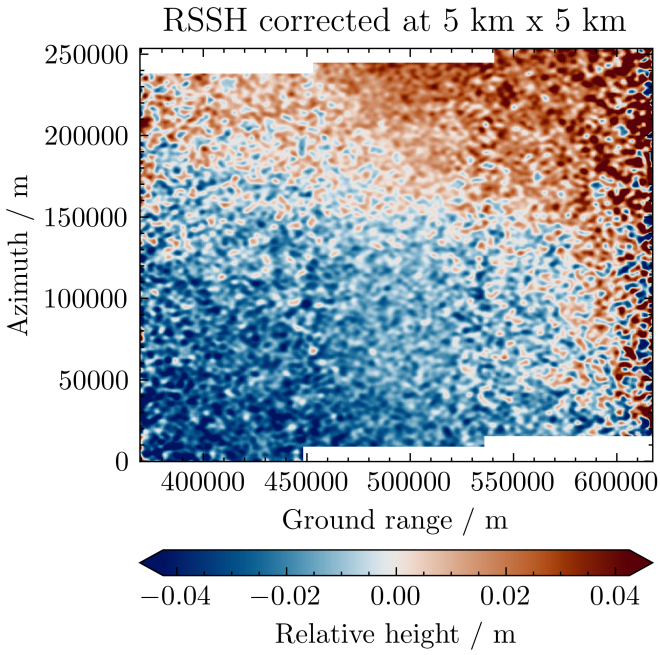

Figure 4.10.: Calibrated retrieved RSSH, with measurement noise filtered at 5 km × 5 km.

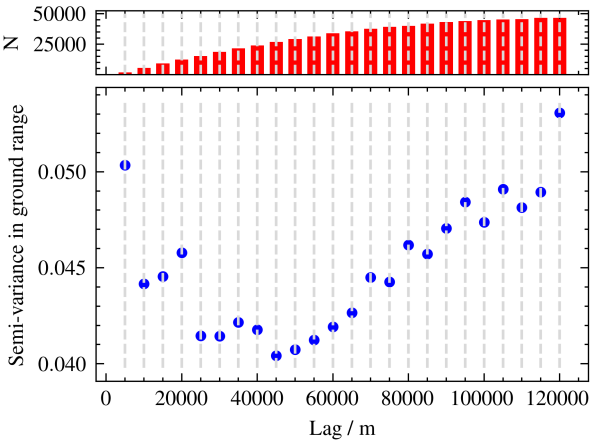

Figure 4.11.: The directional semivariogram of the corrected RSSH in the ground range direction. The semivariogram shows spatial independence.

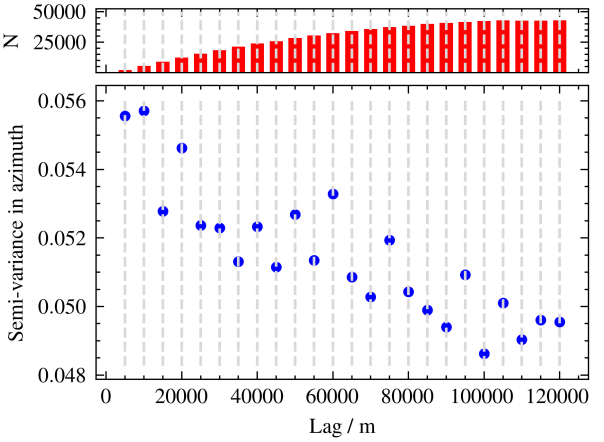

Figure 4.12.: The directional semivariogram of the corrected RSSH in the azimuth range direction. The semivariogram shows spatial independence.

5
Conclusion

How well, if at all, can a multisatellite SAR interferometer estimate OST? The research presented in this dissertation can be summarized as an answer to this question. The research questions, the individual chapters, the motivation for the work, all stem from this question. In Chapter 2 we present the measurement concept, and we model the accuracy of the instrument. While working on Chapter 2, it became clear that the interferometric parameters relevant to the accuracy of the instrument, sensitivity, temporal lag, and spectral shift, have definitions that lose their validity for instruments with significantly squinted beams. Thus, in Chapter 3 we delve into the mathematical fundamentals of interferometry and derive these parameters. In Chapter 4 we present an algorithm that significantly reduces the largest error in the error budget of the measurement, the phase synchronization residual.

5.1. Recapitulation

What is the expected accuracy of interferometric estimates of ocean surface topography obtained from a bistatic system?

We investigate this question by constructing a model to compute the standard error of the OST estimate from a bistatic interferometer. The model considers the thermal, temporal, baseline, and volumetric decorrelation. Formation-flying interferometers suffer from temporal decorrelation because operational safety necessitates a tangential separation. We present a measurement concept that leverages the squint of the radar beam to reduce the effective temporal lag without reducing the physical tangential separation, thus without affecting the operational safety. Specifically, we have found that setting the ratio of the formation's second component of the eccentricity vector to the relative RAAN according to

$$\frac{\Delta e_y}{\Delta \Omega} = \frac{\sin i}{2} \tan \eta, \tag{5.1}$$

reduces the effective temporal lag to $0\,\mathrm{s}$ for a given squint.

We compute the expected standard error of the OST estimate using our performance model for two interferometers: Harmony, and a quasi-monostatic interferometer. Intercepting the noise floor of the instrument with the PSD of the OST shows that Harmony will resolve wavelengths of $38.7\,\mathrm{km}$ to $36.4\,\mathrm{km}$ at winds of $5\,\mathrm{m\,s^{-1}}$ depending on the slope assumed for the density of the OST. At $10\,\mathrm{m\,s^{-1}}$ wind, Harmony will have a resolution of $26.4\,\mathrm{km}$ to $10.7\,\mathrm{km}$ depending on the spectral slope. A quasi-monostatic interferometer is not constrained to synchronize its beams with that of the illuminator. Therefore, it achieves a resolution of $21.9\,\mathrm{km}$ to $7\,\mathrm{km}$ at a $5\,\mathrm{m\,s^{-1}}$ wind, and $14.7\,\mathrm{km}$ to $2.7\,\mathrm{km}$ at a wind speed of $10\,\mathrm{m\,s^{-1}}$.

In addition to the model for the random errors, we have introduced models for systematic errors, i.e. baseline errors, the troposphere error, and the sea-state bias. The model for the sea-state bias shows that it is a function of the surface elevation variance spectrum and the modulation transfer function, and not affected by the instrument's impulse response function. The bias will be between $1.5\,\mathrm{cm}$ and $12.5\,\mathrm{cm}$ depending on the wind speed and direction. Given Harmony's, and other SAR systems', ability to estimate wind speed and wave spectra, we will be able to estimate the bias and remove it from the estimates of OST.

What is the sensitivity of an interferometer with a widely squinted beam?

We answer this question by mathematically analyzing the support of the signals forming the interferogram. We use the Fourier Diffraction Projection Theorem to show that a SAR image gives a tomographic projection of the object, filtered by the impulse response function of the instrument. For a given frequency and time during the illumination time, a SAR recovers the object function for a certain pair of azimuth and range wavenumbers. Over the bandwidth and illumination time of the acquisition, these points trace out concentric circles for monostatic radars, or ellipses for bistatic radars. This region in the Fourier domain is the region of support of the received signal. The information of an interferogram comes from the coherent parts of the interfering signals, which require coincident wavenumbers. Thus, we show that the temporal lag, and the spectral shift are the time shift, and frequency change that achieve wavenumber coincidence in the range-azimuth plane. Moreover, we show that the sensitivity to height is proportional to the elevation component of the wave vector difference at the time and frequency shifts where the wave vectors coincide.

We verify that the wavenumber method of computing the sensitivity and temporal lag converge to the conventional geometric definitions used in the literature for configurations where the assumptions of the geometric definitions are valid. Specifically, we simulate interferometers without squint. For the temporal lag, we use a configuration with only a tangential separation, while for the sensitivity, we use a configuration with a purely cross-track separation.

Furthermore, we compare the conventional expressions of sensitivity and temporal lag, with adjustments for bistatic operation and squinted lines of sight, with the wavenumber methods for a Harmony-like interferometer. The simulations show that the conventional expression for the temporal lag has an absolute error of $0.4\,\mathrm{ms}$. The conventional expression for sensitivity has a relative error of 7%.

From the simulation results, we conclude that the conventional expressions for sensitivity and temporal lag are not as accurate as the wavenumber-based method for interferometers with squinted beams. They require the use of a scaling factor and an equivalent, virtual, system to approach the wavenumber-based method. On the other hand, the wavenumber-based method works for both monostatic and bistatic interferometers, and with all types of viewing geometries.

To what degree can we correct the data to reduce the phase-synchronization error with a data-driven algorithm?

To answer this question, we first set up a simulation chain that produces the interferometric phase that Harmony will observe over a scene in the Bay of Biscay. We use a dataset from the MARC project [79–81] that contains high resolution topography, wind, currents, significant wave height, and directional wave spectra. By using the method for calculating the sensitivity and temporal lag of Chapter 3, and the performance model of Chapter 2, we compute the standard deviation of the interferometric phase due to random errors. Additionally, we simulate the post-GNSS phase synchronization residual from its PSD. We then calculate the acquisition timeline of the instrument according to the TOPSAR parameters that Harmony will use and construct the interferometric phase of the acquisition with random errors and the phase synchronization residual.

Once we have the simulated interferometric phase, we proceed with the calibration using the algorithm presented in Chapter 4. The algorithm uses multisquint processing [70], and the differences in interferometric phase between the overlaps between adjacent bursts within the same subswath [36] to estimate the phase synchronization residual from the corrupted signal. The simulations firstly verify our expectation that the post-GNSS residual dominates the retrieved interferometric phase. Secondly, they show that the algorithm estimates the phase synchronization residual with an unbiased RMSE of $0.010°$. In terms of the algorithm, the findings show that the additional information provided by the TOPSAR overlaps improves the estimate, from an unbiased RMSE of $0.043°$ to $0.010°$, by constraining the low-frequency variation of the phase synchronization residual.

5.2. Contributions

This research has provided the following contributions to the field:

- Development of the multisatellite wide-swath ocean altimetry measurement concept and performance model for the retrieval of relative sea-surface height at the submesoscales from a formation-flying SAR interferometer, leading to the definition of an experimental sea-surface height product for the Harmony mission.

- Development of an analytical model for sea-state bias in measurements of sea-surface height from bistatic single-pass cross-track interferometry.

- Introduction of the wavenumber-support method allowing the accurate determination of the temporal lag, spectral shift, and sensitivity to height of bistatic, and monostatic, SAR interferometers.

- Development of the data-driven phase synchronization algorithm for Harmony's relative sea-surface height product.

The work included in this dissertation was carried out within the Harmony Science Consolidation Studies. The author had the privilege of participating in a breadth of activities, beyond the confines of this dissertation, with a collaborative group. As a result, contributions to the following developments were made that are strongly linked to, but not discussed in this dissertation:

- Development of the Harmony Scientific Workbench software for simulation of Harmony's level-1 and level-2 products from heterogeneous oceanic scenes.

- Harmony's rough surface scattering model, accounting for the bistatic operation and viewing geometry.

- Incorporation of the WaveWatch III, and MARS3D models into Harmony's scientific workbench, allowing the simulation of the RSSH from heterogeneous scenes.

5.3. Recommendations

The thesis presents a complete story, from measurement concept and performance to retrieval of the geophysical parameter of interest, on how to design and model a bistatic interferometer to retrieve OST. It is the sincere hope of the author that the findings of the research will be used not only for the experimental ocean altimetry product of the Harmony mission but also in the design and modeling of future bistatic missions. That is not to imply that the work is complete, far from it. Several questions and ideas arose while carrying out this work that have not been addressed due to lack of time. We elaborate on the most prominent in the following paragraphs.

In Chapter 2 we have assessed the resolution of the instrument in terms of the OST wavelength. While this is the correct approach, as it relates the variance of the instrument errors to the PSD of the geophysical signal at different scales, it can be improved. A reasonable next step would be spectrally characterizing the systematic errors and biases presented in Sections 2.4 and 2.5 and including them in the spectral envelope of the error.

In the analysis of spatial and spectral scales in Section 2.3.3 we use two different models for the PSD of the topography:

1. A power law model with a slope of -1.56 representing the low latitudes.

2. A power law model with a slope of $-\frac{11}{3}$ representing the midlatitudes.

These models were developed from nadir altimeter data, which do not have a swath. Hence, they are 1D models. In our analysis, we have assumed a directionally homogeneous spectral density when converting the standard error of the estimate to a 1D spectral noise floor. A wide-swath ocean altimeter resolves the surface in range, in addition to azimuth. Therefore, in the case of a heterogeneous ocean, the spectrum would be different in range and azimuth, resulting in different range and azimuth resolutions. We expect that with SWOT data, we will be able to test our assumption of a directionally homogeneous spectrum. Additionally, in the future we expect new spectral models of ocean topography to emerge with potentially different spectral slopes in each direction, allowing us to compute the differences in range and azimuth resolution.

Another limitation is that in an attempt to give a global picture, we compute the performance using the median noise floor over an entire track. In a formation-flying system, such as Harmony, there are significant variations of performance over half an orbit. A more accurate picture of performance can be obtained by computing the median noise floor over smaller regions and intersecting it with the spectral model of topography that is valid in that region.

In terms of systematic errors and biases, two errors dominate: the sea-state bias, and the phase synchronization error. In XTI, the sea-state bias results from the cross-correlation between the wave height, the NRCS, and the radial orbital velocities of the surface. The bias can be broken down into the following components:

1. In the near-nadir region of incidence angles, the NRCS changes due to variations of the incidence angle relative to the local surface normal. This effect is known as the tilt modulation, and it decreases with incidence angle up to 45° [89, 90].

2. The interaction between the long waves and the short Bragg resonant waves causes a difference in roughness, and thus a difference in NRCS between the crests and troughs of long waves. Troughs scatter more than crests, hence modulating the NRCS in an effect known as the hydrodynamic modulation [91–93].

3. A radar focuses the signal coming from several points on the surface to a single range cell due to the elevation distribution of waves. This effect is known as range bunching in SAR imaging [28, 94], and tends to mix signal coming from crests and troughs. In a wide-swath altimeter with near-nadir incidence angles this biases the height estimate. The effect diminishes with increasing incidence angle.

4. A SAR shifts signal contributions coming from facets with orbital velocities. This effect is known as velocity bunching[95].

The first two sources of bias are due to the cross-correlation of the NRCS with the surface, and are known as electromagnetic bias in nadir altimetry. We mathematically analyze the bias of the sea-state on the height estimate in Section 2.5.2 and in Appendices A.1, and A.2.

In our analysis we consider the tilt modulation and range bunching negligible at the medium to high incidence angles that we study. We show that the effect of velocity bunching leads to higher or lower density of certain facets in the interferogram which can potentially bias the estimate. During multilooking, the facets with higher and lower densities are averaged together, canceling this effect, as long as the final product resolution is larger than the wavelength. In our analysis we assume that this is true, in which case the bias of a dynamic surface reduces to that of a frozen surface. If, however, the wave steepness is significant, then velocity bunching becomes non-linear and this assumption breaks [96]. Thus, in the future one would need to evaluate the effect and frequency of large wave steepness.

Our computations show that the sea-state bias varies between $1.5\,\mathrm{cm}$ to $12.5\,\mathrm{cm}$. Quantitatively, the sea-state bias is large relative to the dynamic range of the OST. However, a bias that is constant in range and azimuth will not impact the accuracy of the interferometric estimate, which is a relative quantity, as long as it does not cause the interferometric phase to wrap. Given that the height of ambiguity of the interferometers we consider is a few tens of meters, such biases are unlikely to cause wrapping.

Furthermore, the mathematical model that we have established suggests that the sea-state bias depends only on the instrument response function, the MTF, and the elevation variance spectrum of the surface. The MTF has been studied, and there are various models for it in the literature. The instrument response function depends only on instrument parameters and can be readily defined for a given instrument. Thus, if we know the surface elevation variance spectrum, we can compute the sea-state bias and remove it from the height estimates. Harmony, and potentially other future SAR mission, will provide a surface elevation variance spectrum as one of its products [97]. Consequently, we can use estimates of the elevation variance spectrum derived from the same data as the interferometric height to remove the sea-state bias from the latter. We recommend carrying out a study using Harmony's end-to-end simulator [98] to verify this approach to the retrieval.

Moving on to the recommendations regarding the phase synchronization algorithm, the algorithm of Chapter 4 shows satisfactory performance and is smaller than the error budget allocation made in Table 2.3. Nevertheless, we believe we can improve the algorithm by using the synchronization residual's PSD or second-order statistics to adaptively estimate the solution. In the future, we would also like to verify the results of Chapter 4 by running the algorithm on data from Harmony's end-to-end simulator.

Moreover, our simulations of the acquisition timeline and the phase synchronization algorithm have allowed us to reach the following findings:

1. If different subapertures experience different train-off-the-track shifts, then they will have a relative misregistration. This will lead to a wrong resampling step, and the averaging step is no longer coherent.

2. If the subaperture duration is not an integral multiple of the sampling period,

then interval over which the algorithm computes the finite phase difference is smaller than the step between consecutive estimates of the derivative. This leads to a phase estimation error, as the algorithm misses variations of the phase difference that occur in the gaps between samples of adjacent subapertures.

We recommend two solutions to the first issue. The first is to form the subapertures from the raw data, before focusing. Then focus the subapertures, run the algorithm to calibrate to estimate the synchronization residual, remove the estimated phase residual from the raw data, and refocus the full-aperture signals. The second is to estimate the Doppler in each subaperture, use the Doppler to calculate the shift due to the train-off-the-track effect, and apply the correction before calibrating.

The second issue is difficult to solve. In principle, we can solve it by matching the subaperture integration time to the sampling period, or an integral multiple thereof. In practice this is difficult to achieve because of the bursts of the TOPSAR mode, and the antenna weighting of the samples which affect the effective sensing times.

5.4. Looking to the Future

Measurements of RSSH with the accuracy and resolution presented in this dissertation have the potential to enable the quantification of ocean submesoscale dynamics. As a matter of fact, state of the art WSOA has already began to shed light on these processes through the SWOT mission [99, 100]. The improved capability in resolving oceanic spatial scales will bring along a new set of challenges.

The first challenge, which the careful reader might have already pondered, is the retrieval of surface current velocities from RSSH measurements of submesoscale flows. The velocity of oceanic flows is retrieved from altimeter measurements of RSSH by solving the momentum-balance equations under the condition of geostrophy. However, when the velocity gradients approach the Coriolis force, flows are not in geostrophic balance. Submesoscale eddies are not in geostrophic balance, but in gradient wind balance. Thus, retrieving their velocities from RSSH requires solving the momentum balance equations for the non-geostrophic regime [99].

Moreover, while the focus of this dissertation has been on resolving the submesoscales spatially, the temporal sampling of the system is also important. Typical Earth observation missions have repeat cycles of days, resulting in poor temporal sampling for the rapidly evolving submesoscales. Data assimilation techniques could provide a solution to these sampling gaps.

Finally, as the instrument resolves finer scales, more phenomena begin to influence the measurement of RSSH. At the submesoscales, internal waves produce RSSH signatures of comparable magnitude to the currents [99, 100]. Therefore, the surface current retrieval algorithm would have to estimate the internal wave RSSH and remove it from the measurement [101], in a similar way that the wave-Doppler contribution has to be removed from ATI measurements before the in-

stantaneous surface current is retrieved. Flexible multi-domain remote sensing missions, such as Harmony, are uniquely equipped to face these challenges by exploiting simultaneous measurements of different physical quantities, such as SST, wave spectra, surface stress without having to assimilate data from other instruments or models.

These challenges show that the road towards translating the measurement proposed in this work to scientific insight is long. However, at the end of the road new possibilities await. SAR is the only remote sensing instrument capable of measuring submesoscale processes during atmospheric and oceanic extreme conditions. Particularly C-band SAR, as it suffers less from rain contamination than higher-frequency instruments. Thus, the simultaneous measurement of RSSH, SST, surface stress, wave spectra, and potentially surface current vectors, albeit with degraded performance, by Harmony will allow us to parameterize air-sea interactions in TCs, and ETCs. Additionally, the capability of the system to produce this data from the surface below the eye will enable studying the role of oceanic feedback to the intensification of cyclones. For submesoscale flows, RSSH measurements could extend our present estimates of the kinetic energy spectrum down to $10\,\mathrm{km}$ scales, strengthening our knowledge of the ocean energy budget.

Bibliography

[1] L.-L. Fu, T. Lee, W. T. Liu and R. Kwok. '50 Years of Satellite Remote Sensing of the Ocean'. In: *Meteorological Monographs* 59.1 (1st Jan. 2019), pp. 5.1–5.46.

[2] J. C. McWilliams. 'Submesoscale Currents in the Ocean'. In: *Proceedings of the Royal Society A: Mathematical, Physical and Engineering Sciences* 472.2189 (31st May 2016), p. 20160117.

[3] X. Capet, J. C. McWilliams, M. J. Molemaker and A. F. Shchepetkin. 'Mesoscale to Submesoscale Transition in the California Current System. Part III: Energy Balance and Flux'. In: *Journal of Physical Oceanography* 38.10 (1st Oct. 2008), pp. 2256–2269.

[4] M. J. Molemaker, J. C. Mcwilliams and X. Capet. 'Balanced and Unbalanced Routes to Dissipation in an Equilibrated Eady Flow'. In: *Journal of Fluid Mechanics* 654 (July 2010), pp. 35–63.

[5] A. Mahadevan and A. Tandon. 'An Analysis of Mechanisms for Submesoscale Vertical Motion at Ocean Fronts'. In: *Ocean Modelling* 14.3 (1st Jan. 2006), pp. 241–256.

[6] G. Lapeyre and P. Klein. 'Impact of the Small-Scale Elongated Filaments on the Oceanic Vertical Pump'. In: *Journal of Marine Research* 64.6 (1st Nov. 2006), pp. 835–851.

[7] F. Ardhuin, S. T. Gille, D. Menemenlis, C. B. Rocha, N. Rascle, B. Chapron, J. Gula and J. Molemaker. 'Small-Scale Open Ocean Currents Have Large Effects on Wind Wave Heights'. In: *Journal of Geophysical Research: Oceans* 122.6 (2017), pp. 4500–4517.

[8] Y. Quilfen and B. Chapron. 'Ocean Surface Wave-Current Signatures From Satellite Altimeter Measurements'. In: *Geophysical Research Letters* 46.1 (2019), pp. 253–261.

[9] R. H. Stewart. *Introduction to Physical Oceanography*. Robert H. Stewart, 2008.

[10] S. V. Prants, M. Y. Uleysky and M. V. Budyansky. *Lagrangian Oceanography: Large-Scale Transport and Mixing in the Ocean*. 1 online resource vols. Physics of Earth and Space Environments. Cham, Switzerland: Springer Science and Business Media : Springer, 2017. ISBN: 978-3-319-53022-2.

[11] European Space Agency. *Report for Mission Selection: Earth Explorer 10 Candidate Mission Harmony*. ESA-EOPSM-HARM-RP-4129. Noordwijk, The Netherlands: European Space Agency, 2022, p. 369.

[12] W. Mei and C. Pasquero. 'Spatial and Temporal Characterization of Sea Surface Temperature Response to Tropical Cyclones'. In: *Journal of Climate* 26.11 (1st June 2013), pp. 3745–3765.

[13] K. S. Mogensen, L. Magnusson and J.-R. Bidlot. 'Tropical Cyclone Sensitivity to Ocean Coupling in the E CMWF Coupled Model'. In: *Journal of Geophysical Research: Oceans* 122.5 (May 2017), pp. 4392–4412.

[14] T.-L. Chiang, C.-R. Wu and L.-Y. Oey. 'Typhoon Kai-Tak: An Ocean's Perfect Storm'. In: *Journal of Physical Oceanography* 41.1 (1st Jan. 2011), pp. 221–233.

[15] V. Kudryavtsev, A. Monzikova, C. Combot, B. Chapron, N. Reul and Y. Quilfen. 'A Simplified Model for the Baroclinic and Barotropic Ocean Response to Moving Tropical Cyclones: 1. Satellite Observations'. In: *Journal of Geophysical Research: Oceans* 124.5 (2019), pp. 3446–3461.

[16] C. Combot, A. Mouche, J. Knaff, Y. Zhao, Y. Zhao, L. Vinour, Y. Quilfen and B. Chapron. 'Extensive High-Resolution Synthetic Aperture Radar (SAR) Data Analysis of Tropical Cyclones: Comparisons with SFMR Flights and Best Track'. In: *Monthly Weather Review* 148.11 (10th Nov. 2020), pp. 4545–4563.

[17] E. Rodriguez, B. Pollard and J. Martin. 'Wide-Swath Ocean Altimetry Using Radar Interferometry'. In: (July 1999).

[18] A. Theodosiou, M. Kleinherenbrink and P. López-Dekker. 'Wide-Swath Ocean Altimetry Using Multisatellite Single-Pass Interferometry'. In: *IEEE Transactions on Geoscience and Remote Sensing* 61 (2023), pp. 1–21.

[19] L.-L. Fu and R. Ferrari. 'Observing Oceanic Submesoscale Processes From Space'. In: *Eos, Transactions American Geophysical Union* 89.48 (2008), pp. 488–488.

[20] S. D'Amico and O. Montenbruck. 'Proximity Operations of Formation-Flying Spacecraft Using an Eccentricity/Inclination Vector Separation'. In: *Journal of Guidance, Control, and Dynamics* 29.3 (3 May 2006), pp. 554–563.

[21] P. López-Dekker, H. Rott, P. Prats-Iraola, B. Chapron, K. Scipal and E. D. Witte. 'Harmony: An Earth Explorer 10 Mission Candidate to Observe Land, Ice, and Ocean Surface Dynamics'. In: *IGARSS 2019 - 2019 IEEE International Geoscience and Remote Sensing Symposium*. IGARSS 2019 - 2019 IEEE International Geoscience and Remote Sensing Symposium. July 2019, pp. 8381–8384.

[22] D. D'Aria, A. Guarnieri and F. Rocca. 'Focusing Bistatic Synthetic Aperture Radar Using Dip Move Out'. In: *IEEE Transactions on Geoscience and Remote Sensing* 42.7 (July 2004), pp. 1362–1376.

[23] G. Krieger, A. Moreira, H. Fiedler, I. Hajnsek, M. Werner, M. Younis and M. Zink. 'TanDEM-X: A Satellite Formation for High-Resolution SAR Interferometry'. In: *IEEE Transactions on Geoscience and Remote Sensing* 45.11 (11 Nov. 2007), pp. 3317–3341.

[24] A. Moccia and G. Rufino. 'Spaceborne Along-Track SAR Interferometry: Performance Analysis and Mission Scenarios'. In: *IEEE Transactions on Aerospace and Electronic Systems* 37.1 (Jan. 2001), pp. 199–213.

[25] M. Seymour and I. Cumming. 'Maximum Likelihood Estimation for SAR Interferometry'. In: *Proceedings of IGARSS '94 - 1994 IEEE International Geoscience and Remote Sensing Symposium*. Proceedings of IGARSS '94 - 1994 IEEE International Geoscience and Remote Sensing Symposium. Vol. 4. Aug. 1994, 2272–2275 vol.4.

[26] S. Wollstadt, P. López-Dekker, F. De Zan and M. Younis. 'Design Principles and Considerations for Spaceborne ATI SAR-Based Observations of Ocean Surface Velocity Vectors'. In: *IEEE Transactions on Geoscience and Remote Sensing* 55.8 (Aug. 2017), pp. 4500–4519.

[27] P. López-Dekker, Y. Li, L. Iannini, P. Prats-Iraola and M. Rodríguez-Cassola. 'On Azimuth Ambiguities Suppression for Short-Baseline Along-Track Interferometry: The Stereoid Case'. In: *IGARSS 2019 - 2019 IEEE International Geoscience and Remote Sensing Symposium*. IGARSS 2019 - 2019 IEEE International Geoscience and Remote Sensing Symposium. July 2019, pp. 110–113.

[28] E. Peral, E. Rodríguez and D. Esteban-Fernández. 'Impact of Surface Waves on SWOT's Projected Ocean Accuracy'. In: *Remote Sensing* 7.11 (11 Nov. 2015), pp. 14509–14529.

[29] S. Frasier and A. Camps. 'Dual-Beam Interferometry for Ocean Surface Current Vector Mapping'. In: *IEEE Transactions on Geoscience and Remote Sensing* 39.2 (Feb. 2001), pp. 401–414.

[30] F. Gatelli, A. Monti Guamieri, F. Parizzi, P. Pasquali, C. Prati and F. Rocca. 'The Wavenumber Shift in SAR Interferometry'. In: *IEEE Transactions on Geoscience and Remote Sensing* 32.4 (July 1994), pp. 855–865.

[31] H. Zebker and J. Villasenor. 'Decorrelation in Interferometric Radar Echoes'. In: *IEEE Transactions on Geoscience and Remote Sensing* 30.5 (5 Sept. 1992), pp. 950–959.

[32] E. Rodriguez and J. Martin. 'Theory and Design of Interferometric Synthetic Aperture Radars'. In: *IEE Proceedings F - Radar and Signal Processing* 139.2 (Apr. 1992), pp. 147–159.

[33] F. Li and R. Goldstein. 'Studies of Multibaseline Spaceborne Interferometric Synthetic Aperture Radars'. In: *IEEE Transactions on Geoscience and Remote Sensing* 28.1 (Jan. 1990), pp. 88–97.

[34] Y. Yuan. 'Modulation of Radar Observables by Upper Ocean Dynamics | TU Delft Repository'. Delft, The Netherlands: Delft University of Technology, 26th Nov. 2020.

[35] R. Torres, P. Snoeij, D. Geudtner, D. Bibby, M. Davidson, E. Attema, P. Potin, B. Rommen, N. Floury, M. Brown, I. N. Traver, P. Deghaye, B. Duesmann, B. Rosich, N. Miranda, C. Bruno, M. L'Abbate, R. Croci, A. Pietropaolo, M. Huchler and F. Rostan. 'GMES Sentinel-1 Mission'. In: *Remote Sensing of Environment* 120 (May 2012), pp. 9–24.

[36] F. De Zan and A. Monti Guarnieri. 'TOPSAR: Terrain Observation by Progressive Scans'. In: *IEEE Transactions on Geoscience and Remote Sensing* 44.9 (9 Sept. 2006), pp. 2352–2360.

[37] S. Chen and B. Qiu. 'Sea Surface Height Variability in the 30–120 Km Wavelength Band From Altimetry Along-Track Observations'. In: *Journal of Geophysical Research: Oceans* 126.4 (2021), e2021JC017284.

[38] T. Vieira, M. J. Fernandes and C. Lázaro. 'Impact of the New ERA5 Reanalysis in the Computation of Radar Altimeter Wet Path Delays'. In: *IEEE Transactions on Geoscience and Remote Sensing* 57.12 (Dec. 2019), pp. 9849–9857.

[39] E. Rodrigues-Silva and M. Rodriguez-Cassola. 'Analysis of a POD-based Approach for Phase and Time Synchronization of Bistatic and Multistatic SAR Systems'. In: *EUSAR 2021; 13th European Conference on Synthetic Aperture Radar*. EUSAR 2021; 13th European Conference on Synthetic Aperture Radar. Mar. 2021, pp. 1–6.

[40] G. Krieger, F. De Zan, M. Bachmann, P. Lopez Dekker, M. Rodriguez Cassola and J. S. Kim. 'Tropospheric and Ionospheric Effects in Spaceborne Single-Pass SAR Interferometry and Radargrammetry'. In: *EUSAR 2014; 10th European Conference on Synthetic Aperture Radar*. EUSAR 2014; 10th European Conference on Synthetic Aperture Radar. June 2014, pp. 1–4.

[41] P. Dubois and B. Chapron. 'Characterization of the Ocean Waves Signature to Assess the Sea State Bias in Wide-Swath Interferometric Altimetry'. In: *IGARSS 2018 - 2018 IEEE International Geoscience and Remote Sensing Symposium*. IGARSS 2018 - 2018 IEEE International Geoscience and Remote Sensing Symposium. July 2018, pp. 3789–3792.

[42] D. Vandemark, B. Chapron, J. Sun, G. H. Crescenti and H. C. Graber. 'Ocean Wave Slope Observations Using Radar Backscatter and Laser Altimeters'. In: *Journal of Physical Oceanography* 34.12 (1st Dec. 2004), pp. 2825–2842.

[43] K. Hasselmann and S. Hasselmann. 'On the Nonlinear Mapping of an Ocean Wave Spectrum into a Synthetic Aperture Radar Image Spectrum and Its Inversion'. In: *Journal of Geophysical Research: Oceans* 96.C6 (1991), pp. 10713–10729.

[44] T. Elfouhaily, B. Chapron, K. Katsaros and D. Vandemark. 'A Unified Directional Spectrum for Long and Short Wind-Driven Waves'. In: *Journal of Geophysical Research: Oceans* 102.C7 (1997), pp. 15781–15796.

[45] J. Schulz-Stellenfleth, S. Lehner and D. Hoja. 'A Parametric Scheme for the Retrieval of Two-Dimensional Ocean Wave Spectra from Synthetic Aperture Radar Look Cross Spectra'. In: *Journal of Geophysical Research: Oceans* 110.C5 (2005).

[46] A. Theodosiou and P. López-Dekker. 'On the Sensitivity to Height and Motion of Bistatic SAR Interferometry: A Spectral View'. In: *IEEE Transactions on Geoscience and Remote Sensing* 62 (2024), pp. 1–12.

[47] H. C. Graber, D. R. Thompson and R. E. Carande. 'Ocean Surface Features and Currents Measured with Synthetic Aperture Radar Interferometry and HF Radar'. In: *Journal of Geophysical Research: Oceans* 101.C11 (1996), pp. 25813–25832.

[48] R. M. Goldstein, H. A. Zebker and T. P. Barnett. 'Remote Sensing of Ocean Currents'. In: *Science* 246.4935 (8th Dec. 1989), pp. 1282–1285.

[49] R. M. Goldstein and H. A. Zebker. 'Interferometric Radar Measurement of Ocean Surface Currents'. In: *Nature* 328.6132 (6132 Aug. 1987), pp. 707–709.

[50] R. Bamler and P. Hartl. 'Synthetic Aperture Radar Interferometry'. In: *Inverse Problems* 14.4 (Aug. 1998), R1–R54.

[51] H. A. Zebker and R. M. Goldstein. 'Topographic Mapping from Interferometric Synthetic Aperture Radar Observations'. In: *Journal of Geophysical Research: Solid Earth* 91.B5 (1986), pp. 4993–4999.

[52] R. Bamler and G. Davidson. 'Multiresolution Signal Representation for Phase Unwrapping and Interferometric SAR Processing'. In: *IGARSS'97. 1997 IEEE International Geoscience and Remote Sensing Symposium Proceedings. Remote Sensing - A Scientific Vision for Sustainable Development.* IGARSS'97. 1997 IEEE International Geoscience and Remote Sensing Symposium Proceedings. Remote Sensing - A Scientific Vision for Sustainable Development. Vol. 2. Aug. 1997, 865–868 vol.2.

[53] C. Prati and F. Rocca. 'Improving Slant-Range Resolution with Multiple SAR Surveys'. In: *IEEE Transactions on Aerospace and Electronic Systems* 29.1 (Jan. 1993), pp. 135–143.

[54] R.-S. Wu and M. N. Toksöz. 'Diffraction Tomography and Multisource Holography Applied to Seismic Imaging'. In: *GEOPHYSICS* 52.1 (Jan. 1987), pp. 11–25.

[55] S. Tebaldini and F. Rocca. 'Multistatic Wavenumber Tessellation: Ideas for High Resolution P-band SAR Missions'. In: *2017 IEEE International Geoscience and Remote Sensing Symposium (IGARSS)*. 2017 IEEE International Geoscience and Remote Sensing Symposium (IGARSS). July 2017, pp. 2412–2415.

[56] D. Nahamoo, S. Pan and A. Kak. 'Synthetic Aperature Diffraction Tomography and Its Interpolation-Free Computer Implementation'. In: *IEEE Transactions on Sonics and Ultrasonics* 31.4 (July 1984), pp. 218–229.

[57] S. Tebaldini, M. Manzoni, L. Ferro-Famil, F. Banda and D. Giudici. 'FDM MIMO Spaceborne SAR Tomography by Minimum Redundancy Wavenumber Illumination'. In: *IEEE Transactions on Geoscience and Remote Sensing* 62 (2024), pp. 1–19.

[58] P. Lopez-Dekker, P. Prats, F. De Zan, D. Schulze, G. Krieger and A. Moreira. 'TanDEM-X First DEM Acquisition: A Crossing Orbit Experiment'. In: *IEEE Geoscience and Remote Sensing Letters* 8.5 (Sept. 2011), pp. 943–947.

[59] A. Theodosiou, M. Kleinherenbrink and P. López-Dekker. 'Wide-Swath Ocean Altimetry Using Multisatellite Single-Pass Interferometry'. In: *IEEE Transactions on Geoscience and Remote Sensing* 61 (2023), pp. 1–21.

[60] X. Capet, J. C. McWilliams, M. J. Molemaker and A. F. Shchepetkin. 'Mesoscale to Submesoscale Transition in the California Current System. Part I: Flow Structure, Eddy Flux, and Observational Tests'. In: *Journal of Physical Oceanography* 38.1 (1st Jan. 2008), pp. 29–43.

[61] M. Durand, L.-L. Fu, D. P. Lettenmaier, D. E. Alsdorf, E. Rodriguez and D. Esteban-Fernandez. 'The Surface Water and Ocean Topography Mission: Observing Terrestrial Surface Water and Oceanic Submesoscale Eddies'. In: *Proceedings of the IEEE* 98.5 (May 2010), pp. 766–779.

[62] A. Theodosiou, M. Kleinherenbrink and P. López-Dekker. 'Wide-Swath Ocean Altimetry Using Multisatellite Single-Pass Interferometry'. In: *IEEE Transactions on Geoscience and Remote Sensing* 61 (2023), pp. 1–21.

[63] M. Younis, R. Metzig and G. Krieger. 'Performance Prediction of a Phase Synchronization Link for Bistatic SAR'. In: *IEEE Geoscience and Remote Sensing Letters* 3.3 (July 2006), pp. 429–433.

[64] N. J. Willis. *Bistatic Radar*. Institution of Engineering and Technology, 1st Jan. 2004. ISBN: 978-1-891121-45-6 978-1-61353-131-0.

[65] J. L. Auterman. 'Phase Stability Requirements for Bistatic SAR'. In: *IEEE Nat. Radar Conf., Atlanta, 1984*. 1984, pp. 45–52.

[66] D. Massonnet and H. Vadon. 'EES-1 Internal Clock Drift Measured by Interferometry'. In: *IEEE Transactions on Geoscience and Remote Sensing* 33.2 (Mar. 1995), pp. 401–408.

[67] H. Cantalloube, M. Wendler, V. Giroux, P. Dubois-Fernandez and G. Krieger. 'Challenges in SAR Processing for Airborne Bistatic Acquisitions'. In: *Proceedings EUSAR 2004*. European Conference on Synthetic Aperture Radar (EUSAR), Ulm, 25-27 Mai 2004. Ed. by VDE. Vol. 2. Ulm, Germany: VDE Verlag, 2004, pp. 577–580. ISBN: 978-3-8007-2828-2.

[68] M. Rodriguez-Cassola, P. Prats, D. Schulze, N. Tous-Ramon, U. Steinbrecher, L. Marotti, M. Nannini, M. Younis, P. Lopez-Dekker, M. Zink, A. Reigber, G. Krieger and A. Moreira. 'First Bistatic Spaceborne SAR Experiments With TanDEM-X'. In: *IEEE Geoscience and Remote Sensing Letters* 9.1 (Jan. 2012), pp. 33–37.

[69] E. Rodrigues-Silva, M. Rodriguez-Cassola, G. Krieger and A. Moreira. 'GNSS-Based Phase Synchronization for Bistatic and Multistatic Synthetic Aperture Radar'. In: *IEEE Transactions on Geoscience and Remote Sensing* 62 (2024), pp. 1–14.

[70] A. Reigber, P. Prats and J. Mallorqui. 'Refined Estimation of Time-Varying Baseline Errors in Airborne SAR Interferometry'. In: *IEEE Geoscience and Remote Sensing Letters* 3.1 (Jan. 2006), pp. 145–149.

[71] P. Prats, R. Scheiber, A. Reigber, C. Andres and R. Horn. 'Estimation of the Surface Velocity Field of the Aletsch Glacier Using Multibaseline Airborne SAR Interferometry'. In: *IEEE Transactions on Geoscience and Remote Sensing* 47.2 (Feb. 2009), pp. 419–430.

[72] M. Azcueta and S. Tebaldini. 'Non-Cooperative Bistatic SAR Clock Drift Compensation for Tomographic Acquisitions'. In: *Remote Sensing* 9.11 (11 Nov. 2017), p. 1087.

[73] D. Liang, H. Zhang, K. Liu, D. Liu and R. Wang. 'Phase Synchronization Techniques for Bistatic and Multistatic Synthetic Aperture Radar: Accounting for Frequency Offset'. In: *IEEE Geoscience and Remote Sensing Magazine* 10.3 (Sept. 2022), pp. 153–167.

[74] M. D'Errico. *Distributed Space Missions for Earth System Monitoring*. Vol. 31. Springer Science & Business Media, 2012.

[75] A. J. Owens. 'An Algorithm for Generating Fluctuations Having Any Arbitrary Power Spectrum'. In: *Journal of Geophysical Research: Space Physics* 83.A4 (1978), pp. 1673–1675.

[76] P. Prats and J. Mallorqui. 'Estimation of Azimuth Phase Undulations with Multisquint Processing in Airborne Interferometric SAR Images'. In: *IEEE Transactions on Geoscience and Remote Sensing* 41.6 (June 2003), pp. 1530–1533.

[77] K. Ouchi. 'On the Multilook Images of Moving Targets by Synthetic Aperture Radars'. In: *IEEE Transactions on Antennas and Propagation* 33.8 (Aug. 1985), pp. 823–827.

[78] N. B. D. Bechor and H. A. Zebker. 'Measuring Two-Dimensional Movements Using a Single InSAR Pair'. In: *Geophysical Research Letters* 33.16 (2006).

[79] Ifremer, University of Brest, CNRS, IRD, Laboratoire d'Océanographie Physique et Spatiale (LOPS), IUEM, Brest, France. *Data from MARS2D Model Simulations, "Modelling and Analysis for Coastal Research" (MARC) Project.*

[80] Ifremer, University of Brest, CNRS, IRD, Laboratoire d'Océanographie Physique et Spatiale (LOPS), IUEM, Brest, France. *Data from MARS3D Model Simulations, "Modelling and Analysis for Coastal Research" (MARC) Project.*

[81] Ifremer, University of Brest, CNRS, IRD, Laboratoire d'Océanographie Physique et Spatiale (LOPS), IUEM, Brest, France. *Data from WaveWatch III Model Simulations, "Modelling and Analysis for Coastal Research" (MARC) Project.*

[82] L. Pineau-Guillou. 'PREVIMER. Validation des modèles hydrodynamiques 2D des côtes de la Manche et de l'Atlantique'. In: (1st June 2013).

[83] P. Lazure and F. Dumas. 'An External–Internal Mode Coupling for a 3D Hydrodynamical Model for Applications at Regional Scale (MARS)'. In: *Advances in Water Resources* 31.2 (1st Feb. 2008), pp. 233–250.

[84] WW3DG. 'User Manual and System Documentation of WAVEWATCH III Version 6.07, the WAVEWATCH III Development Group'. In: *Tech. Note 326 pp. + Appendices, NOAA/NWS/NCEP/MMAB* (2019).

[85] N. Cressie. *Statistics for Spatial Data.* John Wiley & Sons, 18th Mar. 2015. 931 pp. ISBN: 978-1-119-11518-2. Google Books: MzN_BwAAQBAJ.

[86] O. Schabenberger and C. A. Gotway. *Statistical Methods for Spatial Data Analysis.* New York: Chapman and Hall/CRC, 2nd Feb. 2017. 512 pp. ISBN: 978-1-315-27508-6.

[87] N. Cressie. 'Fitting Variogram Models by Weighted Least Squares'. In: *Journal of the International Association for Mathematical Geology* 17.5 (1st July 1985), pp. 563–586.

[88] R. K. Raney. 'Synthetic Aperture Imaging Radar and Moving Targets'. In: *IEEE Transactions on Aerospace and Electronic Systems* AES-7.3 (May 1971), pp. 499–505.

[89] D. R. Lyzenga. 'Numerical Simulation of Synthetic Aperture Radar Image Spectra for Ocean Waves'. In: *IEEE Transactions on Geoscience and Remote Sensing* GE-24.6 (Nov. 1986), pp. 863–872.

[90] W. R. Alpers, D. B. Ross and C. L. Rufenach. 'On the Detectability of Ocean Surface Waves by Real and Synthetic Aperture Radar'. In: *Journal of Geophysical Research: Oceans* 86.C7 (1981), pp. 6481–6498.

[91] W. C. Keller and J. W. Wright. 'Microwave Scattering and the Straining of Wind-Generated Waves'. In: *Radio Science* 10.2 (Feb. 1975), pp. 139–147.

[92] G. Engen and H. Johnsen. 'SAR-ocean Wave Inversion Using Image Cross Spectra'. In: *IEEE Transactions on Geoscience and Remote Sensing* 33.4 (July 1995), pp. 1047–1056.

[93] J. Schulz-Stellenfleth and S. Lehner. 'Spaceborne Synthetic Aperture Radar Observations of Ocean Waves Traveling into Sea Ice'. In: *Journal of Geophysical Research: Oceans* 107.C8 (1st Aug. 2002), pp. 20–19.

[94] B. Chapron, H. Johnsen and R. Garello. 'Wave and Wind Retrieval from Sar Images of the Ocean'. In: *Annales Des Télécommunications* 56.11 (1st Nov. 2001), pp. 682–699.

[95] W. Alpers and C. Rufenach. 'The Effect of Orbital Motions on Synthetic Aperture Radar Imagery of Ocean Waves'. In: *IEEE Transactions on Antennas and Propagation* 27.5 (Sept. 1979), pp. 685–690.

[96] K. Hasselmann, R. K. Raney, W. J. Plant, W. Alpers, R. A. Shuchman, D. R. Lyzenga, C. L. Rufenach and M. J. Tucker. 'Theory of Synthetic Aperture Radar Ocean Imaging: A MARSEN View'. In: *Journal of Geophysical Research: Oceans* 90.C3 (1985), pp. 4659–4686.

[97] M. Kleinherenbrink, P. López-Dekker, F. Nouguier and B. Chapron. 'Bistatic SAR Mapping of Ocean-Wave Spectra'. In: *IEEE Transactions on Geoscience and Remote Sensing* 62 (2024), pp. 1–12.

[98] G. Monnier, B. Camus, Y.-H. Hellouvry, P. Dubois and E. de Witte. *Synthetic RAW Data Generator for ESA HARMONY Mission*. 16th May 2024. arXiv: 2405.09938 [physics]. URL: http://arxiv.org/abs/2405.09938. Prepublished.

[99] M. Archer, J. Wang, P. Klein, G. Dibarboure and L.-L. Fu. 'Wide-Swath Satellite Altimetry Unveils Global Submesoscale Ocean Dynamics'. In: *Nature* 640.8059 (Apr. 2025), pp. 691–696.

[100] B. Qiu, S. Chen, J. Wang and L.-L. Fu. 'Seasonal and Fortnight Variations in Internal Solitary Waves in the Indonesian Seas From the SWOT Measurements'. In: *Journal of Geophysical Research: Oceans* 129.7 (2024), e2024JC021086.

[101] F. Le Guillou, N. Lahaye, C. Ubelmann, S. Metref, E. Cosme, A. Ponte, J. Le Sommer, E. Blayo and A. Vidard. 'Joint Estimation of Balanced Motions and Internal Tides From Future Wide-Swath Altimetry'. In: *Journal of Advances in Modeling Earth Systems* 13.12 (2021), e2021MS002613.

[102] E. R. Rodriguez and J. Martin. 'Maximum Likelihood Estimation of the Interferometric Phase from Distributed Targets'. In: *IEEE Transaction on Geoscience and Remote Sensing* (1991).

[103] F. Neeser and J. Massey. 'Proper Complex Random Processes with Applications to Information Theory'. In: *IEEE Transactions on Information Theory* 39.4 (July 1993), pp. 1293–1302.

[104] M. Kleinherenbrink, A. Korosov, T. Newman, A. Theodosiou, A. S. Komarov, Y. Li, G. Mulder, P. Rampal, J. Stroeve and P. Lopez-Dekker. 'Estimating Instantaneous Sea-Ice Dynamics from Space Using the Bi-Static Radar Measurements of Earth Explorer 10 Candidate Harmony'. In: *The Cryosphere* 15.7 (6th July 2021), pp. 3101–3118.

[105] A. Theodosiou and P. López-Dekker. 'Data-Driven Phase Synchronisation of Harmony's Ocean Surface Topography Product'. In: *IEEE Transactions on Geoscience and Remote Sensing* (2025).

A

Analysis of Sea-state Bias

A.1. Surface Height Estimate of a Frozen Random Backscattering Surface

In this section we investigate the sea-state bias in the height estimate produced from an interferogram for two cases: a frozen random backscattering surface, and a moving random backscattering surface. In both cases we assume that the interferogram is produced by a pair of images acquired with a zero effective along-track baseline. Consequently, the time dependence of the surface manifests itself in the scattering coefficient but not in the interferometric phase.

In the analysis, we apply the plane wave approximation to the far field of the instrument. $\mathbf{k_q} = k_0(\sin\psi_q, \cos\psi_q \sin\theta_q, \cos\psi_q \cos\theta_q)^T$ is the wave vector, where θ is the look angle, ψ is the squint with respect to the antenna boresight, $k_0 = 2\pi/\lambda_0$ is the wavenumber of the carrier and the subscript $q \in \{T, R\}$ stands for the transmitter and the receiver respectively. R_B is the bistatic range to the location where the plane wave approximation is applied. The image produced by the ith SAR of the interferometer is [50]

$$u_i(x,y) = \mathrm{e}^{-\mathrm{j}k_0 R_{B_i}} \iiint s(\mathbf{r'})\mathrm{e}^{-\mathrm{j}\mathbf{k_{B_i}}\cdot\mathbf{r'}} \chi(x-x', y-y')\,\mathrm{d}V', \tag{A.1}$$

where $s(\mathbf{r'})$ represents the complex scattering coefficient in a Cartesian coordinate system with the origin set at the plane wave expansion point and x being the azimuth direction, y the ground range direction and z the elevation direction. We use the shorthand $\mathbf{r} = (x, y, z)^T$ for functions of (x, y, z). We represent the system imaging transfer function, including the point target response and the processing filters, by $\chi(x, y)$, and the bistatic wave vector by $\mathbf{k_B} = \mathbf{k_T} + \mathbf{k_R}$.

This chapter has been published as A. Theodosiou, M. Kleinherenbrink and P. López-Dekker. 'Wide-Swath Ocean Altimetry Using Multisatellite Single-Pass Interferometry'. In: *IEEE Transactions on Geoscience and Remote Sensing* 61 (2023), pp. 1–21

Let $u_1(x,\rho)$ and $u_2(x,\rho)$ be the two SAR images forming the interferogram

$$\nu(x,\rho) = u_1(x,\rho)u_2(x,\rho)^*,$$

where the superscript * denotes complex conjugation. We assume that the scattering coefficient is a white stochastic process

$$\mathbb{E}_s[s(\mathbf{r_1})s^*(\mathbf{r_2})] = \sigma_0(\mathbf{r_1})\delta(\mathbf{r_1}-\mathbf{r_2}).$$

Then the expected value of the interferogram is

$$\begin{aligned} I(x,\rho) &= \mathbb{E}_s\left[\nu(x,\rho)\right] \\ &= \mathrm{e}^{-\mathrm{j}k_0\Delta R_B}\iiint\iiint \sigma_0(\mathbf{r'})\delta(\mathbf{r'}-\mathbf{r''})\chi(x-x',y-y')\chi(x-x'',y-y'')^* \\ &\qquad \mathrm{e}^{-\mathrm{j}\mathbf{k_{B_1}}\cdot\mathbf{r'}}\mathrm{e}^{\mathrm{j}\mathbf{k_{B_2}}\cdot\mathbf{r''}}\,\mathrm{d}V'\,\mathrm{d}V'', \end{aligned}$$

where $\Delta R_B = R_{B_1} - R_{B_2}$.

We use the even and sifting properties of the Dirac delta function to reduce the expected value of the interferogram to

$$I(x,\rho) = A\iiint \sigma_0(\mathbf{r'})\mathrm{e}^{-\mathrm{j}\Delta\mathbf{k_B}\cdot\mathbf{r'}}\|\chi(x-x',\rho-\rho')\|^2\,\mathrm{d}V', \tag{A.2}$$

where $A = \mathrm{e}^{-\mathrm{j}k_0\Delta R_B}$ and $\Delta\mathbf{k}_B = \mathbf{k_{B_1}} - \mathbf{k_{B_2}}$ is the difference of the bistatic wave vectors.

We are primarily interested in the topographic mapping of the ocean surface, where we can assume that the most prominent contribution to the scattering amplitude comes from the surface. Additionally, the frozen surface $\zeta(x,y)$ is a function of the two horizontal plane coordinates describing the surface height along z. The slant range to a point on the surface at a given azimuth depends solely on the ground range. Thus, (A.2) reduces to an integral over the surface

$$I(x,y) = A\iint \sigma_0(\mathbf{r'_p})\mathrm{e}^{-\mathrm{j}\Delta\mathbf{k}_{R_R}\cdot\mathbf{r'_p}}\|\chi(x-x',\rho-\rho')\|^2\,\mathrm{d}x'\,\mathrm{d}y', \tag{A.3}$$

and the integral can be expressed as the convolution of the backscatter and interferometric phase terms with the norm of the system impulse response function

$$I(x,y) = A(\sigma_0\beta * \|\chi\|^2)(x,y) \tag{A.4}$$

where $\mathbf{r'}_p = (x',y')^T$ is the position vector on the surface and $\beta(\mathbf{r_p}) = \mathrm{e}^{-\mathrm{j}\Delta\mathbf{k}_{R_R}\cdot\mathbf{r_p}}$.

We assume that the wave height is small compared to the height of ambiguity and expand the exponential in β. The expectation of the interferogram after expanding the complex exponential is

$$I(x,y) = A(\sigma_0(1-\mathrm{j}\Delta\mathbf{k}_R\cdot\mathbf{r'_p}) * \|\chi\|^2)(x,y). \tag{A.5}$$

Rodriguez and Martin [102] have shown that the maximum-likelihood estimator of interferometric phase is

$$\hat{\phi} = \arctan\left(\frac{\Im\left(\sum_{n=1}^{N_l} \nu[n]\right)}{\Re\left(\sum_{n=1}^{N_l} \nu[n]\right)}\right), \tag{A.6}$$

where N_l is the number of independent interferometric looks. Noting that for small interferometric phase $\tan\hat{\phi} \approx \hat{\phi}$, the phase and height estimators are

$$\hat{\phi} \approx \frac{\Im\left(\sum_{n=1}^{N_l} \nu[n]\right)}{\Re\left(\sum_{n=1}^{N_l} \nu[n]\right)}, \tag{A.7}$$

$$\hat{h} = -\frac{h_a}{2\pi}\hat{\phi}, \tag{A.8}$$

where h_a is the height of ambiguity. Assuming that the scattering stochastic process is correlation ergodic and that we use a sufficient number of looks allows us to substitute (A.5) into (A.8)

$$\hat{h} \approx \frac{K}{\bar{\sigma}(\mathbf{r_p})} \iint \sigma_0(\mathbf{r'_p})\Delta\mathbf{k}_R \cdot \mathbf{r'}_p \|\chi(x-x', \rho-\rho')\|^2 \,\mathrm{d}S' \tag{A.9}$$

where

$$\begin{aligned} \mathrm{d}S' &= \mathrm{d}x'\,\mathrm{d}y' \\ K &= \frac{h_a}{2\pi} \\ \bar{\sigma}(\mathbf{r}_p) &= \iint \sigma_0(\mathbf{r'_p})\|\chi(x-x', \rho-\rho')\|^2 \,\mathrm{d}x'\,\mathrm{d}y'. \end{aligned}$$

Henceforth, we will assume that the spatial variability of the instrument-response averaged cross-section can be neglected, i.e. $\bar{\sigma}(\mathbf{r}_p) = \bar{\sigma}$. Additionally, we will decompose the radar cross-section into a spatially averaged constant component and a spatially varying component [96] [28]

$$\sigma_0(x,y) = \bar{\sigma} + \bar{\sigma}\delta\sigma(x,y).$$

Then (A.9) can be re-written as

$$\hat{h} \approx K \iint \frac{\bar{\sigma}(1+\delta\sigma(x',y'))\Delta\mathbf{k}_R \cdot \mathbf{r'}_p}{\bar{\sigma}} \|\chi(x-x', \rho-\rho')\|^2 \,\mathrm{d}S', \tag{A.10}$$

which agrees with the equation for the height measurement of the SWOT interferometer presented in [28].

We can see that the first term is proportional to the phase difference of the two SAR images, which is defined by ocean surface but the product in the second

term $\delta\sigma(x',y)\Delta\mathbf{k}_R \cdot \mathbf{r'}_p$ introduces a correlation between the NRCS and the surface height that biases the estimate. The NRCS can, in the context of linear modulation theory as demonstrated by Hasselmann and Hasselmann, be expressed as a function of the surface elevation [43]

$$\sigma_0(\mathbf{r}_p,t) = \bar{\sigma}(1 + \iint_{\mathbf{k}} \tilde{\delta\sigma}(\mathbf{k})\mathrm{e}^{-j(\mathbf{k_w}\cdot\mathbf{r}_p-\omega_w t)}\,\mathrm{d}k_x\,\mathrm{d}k_\rho),$$

where $\mathbf{k}$ is the 2D wavenumber of the surface waves whose positive and negative values are included in the domain of integration. $\bar{\sigma}$ denotes the spatially averaged NRCS and $\omega_w = \sqrt{gk}$ is the gravity wave angular frequency. The cross-section modulation factor $\tilde{\delta\sigma}(\mathbf{k})$ and surface wave amplitude $Z(\mathbf{k})$ are related through the modulation transfer function (MTF) [43]

$$\tilde{\delta\sigma}(\mathbf{k}) = T\big(\mathbf{k}\big)Z\big(\mathbf{k}\big), \tag{A.11}$$

where capital letters represent the Fourier transform of functions notated by the corresponding lowercase symbols. In cases where capitalization leads to a symbol that conventionally has an established meaning, e.g. $\delta\sigma$, we use the tilde to represent the Fourier transform.

Thus, the variation in cross section $\delta\sigma(x,y)$ can be expressed as the inverse Fourier transform of the product of the MTF and the surface wave amplitude

$$\frac{\delta\sigma(x,y)}{\bar{\sigma}(x_0,y_0)} = \mathcal{F}^{-1}\Big\{T\big(\mathbf{k}\big)Z\big(\mathbf{k}\big)\Big\}(x,y). \tag{A.12}$$

Equation (A.12) can be used to simplify (A.10). The dot product of the wave vector difference with the position of the resolution cell is

$$\begin{aligned}(\mathbf{k}_{R_1} - \mathbf{k}_{R_2})\cdot\mathbf{r} = k_{R_1}\big[&2x\sin\Delta\psi/2\cos\psi + y(\sin\theta_1\cos\psi_1 - \sin\theta_2\cos\psi_2)\\ &+ z(-\cos\theta_1\cos\psi_1 + \cos\theta_2\cos\psi_2)\big],\end{aligned} \tag{A.13}$$

where $\psi = (\psi_{R_1} + \psi_{R_2})/2$ and we have assumed that both receivers use the same carrier frequency. In equation (A.13) we have made the assumption that the difference in look angles and squint is small. Substituting back to the expression for the surface wave height estimate

$$\hat{h} = Kq(1 + \mathcal{F}^{-1}\Big\{T\big(\mathbf{k}\big)Z\big(\mathbf{k}\big)\Big\})z * \|\chi(x,\rho)\|^2, \tag{A.14}$$

with

$$q = k_{R_1}(-\cos\theta_1\cos\psi_1 + \cos\theta_2\cos\psi_2),$$

where we have expressed the MLE of the measured height as a convolution of the product of the height and cross section with the instrument response function. Additionally, we have neglected the terms proportional to x and y because while there is a local correlation between (x,y) and the NRCS we expect that globally the offset in NRCS due to the variation of the waves in the horizontal direction

will not be systematic. We express the height of ambiguity in terms of the incident and squint angles

$$\begin{aligned} h_a &:= 2\pi\left(\frac{\partial\phi}{\partial z}\right)^{-1} \\ &= \frac{2\pi}{k_{R_1}(-\cos\theta_1\cos\psi_1 + \cos\theta_2\cos\psi_2)} \end{aligned}$$

which simplifies the leading constant of $\hat{h}$ to unity.

To evaluate the bias of the estimator we need to compute the expected value of the estimator over the ensemble of wave surfaces. We express the expected value of the estimator in terms of the inverse Fourier transforms of $\delta\sigma$ and z. The focus is on the second term of (A.14), which we label $A(x,y) = \delta\sigma(x,y)z(x,y)$

$$\begin{aligned} \mathbb{E}_w[A(x,y)] = &\quad \mathbb{E}_w[\mathcal{F}^{-1}\{T(\mathbf{k})Z(\mathbf{k})\}\mathcal{F}^{-1}\{Z(\mathbf{k})\}] \\ = &\quad \mathbb{E}_w\left[\int T(\mathbf{k'})Z(\mathbf{k'})\mathrm{e}^{-j(\mathbf{k'}\cdot\mathbf{r}_p)}\,\mathrm{d}\mathbf{k'}\int Z(\mathbf{k''})\mathrm{e}^{-j(\mathbf{k''}\cdot\mathbf{r}_p)}\,\mathrm{d}\mathbf{k''}\right], \end{aligned} \tag{A.15}$$

where we can use the fact that the ocean wave field is real $z(x,y) = z(x,y)^*$ and the linearity of the expected value and the Fourier transform to simplify the expression

$$\begin{aligned} \mathbb{E}_w[A(x,y)] &= \iint T(\mathbf{k'})\,\mathbb{E}_w[Z(\mathbf{k'})Z(\mathbf{k''})^*]\mathrm{e}^{-j((\mathbf{k'}-\mathbf{k''})\cdot\mathbf{r}_p)}\,\mathrm{d}\mathbf{k'}\,\mathrm{d}\mathbf{k''} \\ &= \iint T(\mathbf{k'})\Psi(\mathbf{k'})\delta(k'_x - k''_x)\delta(k'_y - k''_y)\mathrm{e}^{-j((\mathbf{k'}-\mathbf{k''})\cdot\mathbf{r}_p)}\,\mathrm{d}\mathbf{k'}\,\mathrm{d}\mathbf{k''} \\ &= \int T(\mathbf{k})\Psi(\mathbf{k})\,\mathrm{d}\mathbf{k}. \end{aligned} \tag{A.16}$$

The definition of the surface elevation variance spectrum, as defined in [96]

$$\mathbb{E}_w[Z(\mathbf{k})Z(\mathbf{k'})] := \Psi(\mathbf{k})\delta(\mathbf{k}-\mathbf{k'}), \tag{A.17}$$

and the sifting property of the Dirac delta function were used to simplify the expression of the bias term. Substituting (A.16) into (A.14) yields

$$\mathbb{E}_w\left[\hat{h}\right] = \mathbb{E}_w[z(x,y)] * \|\chi(x,y)\|^2 + \int T(\mathbf{k})\Psi(\mathbf{k})\,\mathrm{d}\mathbf{k}\iint\|\chi(x,y)\|^2\,\mathrm{d}x\,\mathrm{d}y. \tag{A.18}$$

Equation (A.18) shows that the expected value of the estimator is the ensemble mean of the surface wave height filtered by the instrument response plus an additional term that is a function of the MTF and elevation spectrum. The additional term biases the estimator away from the true value of the surface height. The effect is well known in nadir altimetry as electromagnetic bias [42].

The expression for $\mathbb{E}_w\left[\hat{h}(\mathbf{r})\right]$ gives us the expected height estimate as a function of the spatial coordinates in the horizontal plane. We can obtain a measure of the

bias due to the modulation of the NRCS by the surface-wave height by computing the integral of the second term in (A.18)

$$\mathrm{Bias}(\hat{h}, z) = \int T(\mathbf{k})\Psi(\mathbf{k})\,\mathrm{d}\mathbf{k} \iint \|\chi(x,y)\|^2\,\mathrm{d}x\,\mathrm{d}y. \tag{A.19}$$

For the purposes of investigating the effect of the instrument target response on the bias, let us assume that $\chi(x,y)^2$ is a two-dimensional squared sinc function [28]

$$\chi(x,y)^2 = \frac{1}{\delta\rho_x\delta\rho_y}\,\mathrm{sinc}\left(\frac{x}{\delta\rho_x}\right)^2 \mathrm{sinc}\left(\frac{y}{\delta\rho_y}\right)^2$$

with spatial resolutions $\delta\rho_x$ and $\delta\rho_y$ in azimuth and ground range respectively. The integral over $\chi(x,y)^2$ evaluates to unity, and the bias becomes a function only of the MTF and the elevation spectrum of the surface.

A.2. Surface Height Estimate of a Moving Random Backscattering Surface

The derivation of the height bias for the case of a moving surface largely follows that of a frozen surface presented in the previous section of the appendix with a key difference. Since the surface is now not assumed to be frozen, the scattering coefficient depends on both space and time. The synthetic aperture of the instrument records the temporal variation of the scattering coefficient during the illumination time. Therefore, the interferogram and the height estimate can no longer be expressed as two-dimensional convolutions of the point target response and the NRCS as in (A.3) and (A.18).

The time dependence of the scattering coefficient means that the azimuth processing of the SAR image needs to be accounted for to arrive at an expression of the image. The derivation of the expected value of the interferometric height estimate in this section is based on Hasselmann's [96] derivation of the mean SAR image intensity for a moving surface. To make the analysis easier to follow, we only consider the azimuth coordinate of the scattering coefficient, the point target response, and the impulse response of the processing filter. Given that sensing in the range direction occurs at the speed of light, we are neglecting the motion of the backscattering surface in the range dimension. The results of this subsection can be extended to the range direction by following the derivation of the previous section.

The processed signal is obtained by matched filtering in range, followed by matched filtering in azimuth. Since we are interested in the interferometric height estimate, we include in our equations the phase term due to the range to the surface that is part of the signal after range compression even though we do not go through the range processing in the analysis. Consequently, we express the processed signal as the matched filtering of the received signal and the exponential phase term

$$u_i(x) = \iint f_2(x - x'')f_1(x'' - x')s(x', t'')\mathrm{e}^{-\mathrm{j}k_0 R'_{B_i}}\,\mathrm{d}x'\,\mathrm{d}x'', \tag{A.20}$$

where R_{B_i} is the bistatic range to a scatterer, $f_1(x)$ is the azimuth point target response and $f_2(x)$ is the azimuth matched filter. As noted in [96], (A.20) cannot be contracted into a convolution of two functions of x as in (A.1). The azimuth point target response and the matched filter are

$$f_1(x) = \mathrm{e}^{-\mathrm{j}k_0/Rx^2} w_1(x) \tag{A.21}$$

$$f_2(x) = \mathrm{e}^{+\mathrm{j}k_0/Rx^2} w_2(x), \tag{A.22}$$

where $w_1(x)$ is the antenna pattern in azimuth and $w_2(x)$ is a weighting function over the integration time of the SAR processor T_I.

We substitute the transfer functions (A.21) and (A.22) in the expression for the processed signal, and after expansion of the quadratic terms in the exponentials and making a substitution for the second variable of integration, equation (A.20) may be expressed as an integral over the finite resolution Fourier transform of $s(x,t)$ [96]

$$u_i(x) = \int \mathrm{e}^{-\mathrm{j}k_0 R'_{B_i}} N' \tilde{s}(x', T_I, \omega)\, \mathrm{d}x' \tag{A.23}$$

where

$$\tilde{s}(x', T_I, \omega) = \int w(\hat{t}, \omega) s(x', t' + \hat{t}) \mathrm{e}^{-\mathrm{j}\omega\hat{t}}\, \mathrm{d}\hat{t},$$

$$\omega = \frac{k_0 v(x - x')}{R_{B_i}},$$

and we have grouped the two filter responses into a single function

$$w(\hat{t}, \omega) = w_1(v\hat{t}) w_2\left(\frac{R_{B_i}\omega}{k_0 v} - v\hat{t}\right) N^{-1}.$$

The normalization factors N and N' are the same as in [96] with the bistatic range replacing the monostatic range.

Equation (A.23) is a generalized expression for the imaging of a dynamic backscattering surface analogous to that of a frozen surface (A.1). Therefore, we can proceed as in the previous section to obtain an expression for the height estimate using the maximum-likelihood estimator of interferometric phase. Applying the assumption that the surface is spatially white, and correlation ergodic, and expanding the exponential as in the case of a frozen surface yields

$$\hat{h} = \int \frac{1}{\bar{\sigma}_0(x)} N^2 \sigma_0(x', T_I) z(x') \tilde{R}_{ss}(x', T_I; \omega)\, \mathrm{d}x', \tag{A.24}$$

where in this case the averaged NRCS takes the form

$$\bar{\sigma}_0(x) = \int N^2 \sigma(x', T_I) \tilde{R}_{ss}(x', T_I; \omega)\, \mathrm{d}x'.$$

The model used for the expectation over the ensemble of speckle realizations is [96]

$$\mathbb{E}_s[s(x,t)s(x+x', t+\tau)] = \sigma_0(x,t) R_{ss}(x,t;\tau)\delta(x')$$

and the equivalent relation in the frequency domain is

$$\mathbb{E}_s[\tilde{s}(x,T_I;\omega)\tilde{s}(x+x',T_I;\omega)^*] = \tilde{\sigma}_0(x,T)\tilde{R}_{ss}(x,T_I;\omega)\delta(x').$$

$\tilde{R}_{ss}(x,T_I;\omega)$ is the normalized variance spectrum of the scattering element with azimuth position x at a frequency offset given by ω. The variance spectrum is of finite resolution due to the bandwidth of the SAR processor in azimuth which is set by the integration time T_I. The frequency offset ω arises due to the time dependence, i.e. the motion, of the scatterer at a given azimuth position during the integration time. The spectral components of the surface reflectivity at x' are given by $\tilde{s}(x',T_I;\omega)$. The variance spectrum is a measure of the intensity of the SAR image as a function of the offset frequency. If the Doppler processing bandwidth is larger than the bandwidth of the variance spectrum, then the motion of the surface results in a smearing of the height estimate without loss of spectral information.

Taking the expectation of the estimator over the wave ensemble yields

$$\mathbb{E}_w[\hat{h}] = \int \frac{1}{\bar{\sigma}_0(x)} N^2\, \mathbb{E}[\sigma_0(x',T_I)z(x')]\tilde{R}_{ss}(x',T_I;\omega)\,\mathrm{d}x'.$$

Expanding $\sigma_0(x',T_I) = \bar{\sigma}_0(x)(1+\delta\sigma(x',T_I))$ and substituting the MTF into the expression yields an analogous expression to the one for the frozen surface but instead of the square of the imaging transfer function $\chi(x,y)^2$ we have the finite resolution variance spectrum of the scattering surface

$$\mathbb{E}_w\,[\hat{h}] = \int N^2\, \mathbb{E}[z(x',y)]\tilde{R}_{rr}(x',T_I;\omega)\,\mathrm{d}x' + \int T(\mathbf{k})\Psi(\mathbf{k})\,\mathrm{d}\mathbf{k} \int N^2\tilde{R}_{rr}(x',T_I;\omega)\,\mathrm{d}x'. \quad \text{(A.25)}$$

In the case of multilooking, we can assume that the azimuth bandwidth of surface reflectivity is smaller than the processing bandwidth and N^2 is independent of frequency [96] and can be taken out of the integrals in the numerator and denominator of (A.24)

$$\mathbb{E}_w\,[\hat{h}] = \int \mathbb{E}[z(x',y)]\tilde{R}_{rr}(x',T_I;\omega)\,\mathrm{d}x' + \int T(\mathbf{k})\Psi(\mathbf{k})\,\mathrm{d}\mathbf{k} \int \tilde{R}_{rr}(x',T_I;\omega)\,\mathrm{d}x'. \quad \text{(A.26)}$$

Since the variance spectrum is normalized, $\int \tilde{R}_{rr}(x',T_I;\omega)\,\mathrm{d}x'$ integrates to unity and the height bias is determined exclusively by the MTF and the elevation spectrum of the surface, as in the case of the frozen surface.

B

Circular Complex Wide-Sense Stationary Processes and Their Frequency Components

To prove (3.17) we need to assume that the complex stochastic process $s(x)$ has a mean of zero, $\mathbb{E}[s(x)] = 0$, and that it is circular, i.e. $\mathbb{E}[s(x)s(u)] = 0$. Thus, the second-order statistics of the process are encapsulated by the autocorrelation function

$$\mathbb{E}[s(x)s(u)^*] = R_s(x,u). \tag{B.1}$$

The following proof is an extension of theorem 4 of [103] to continuous processes. The correlation of the Fourier transform of the stochastic process, $\tilde{s}(k_x)$, is

$$\begin{aligned}
\mathbb{E}[\tilde{s}(k)\tilde{s}(\kappa)^*] &= \mathbb{E}\left[\int s(x)\mathrm{e}^{-\mathrm{j}kx}\,\mathrm{d}x\left(\int s(u)\mathrm{e}^{-\mathrm{j}\kappa u}\,\mathrm{d}u\right)^*\right] \\
&= \iint \mathbb{E}[s(x)s(u)^*]\mathrm{e}^{-\mathrm{j}kx}\,\mathrm{d}x\mathrm{e}^{\mathrm{j}\kappa u}\,\mathrm{d}u \\
&= \iint R_s(x-u)\mathrm{e}^{-\mathrm{j}kx}\,\mathrm{d}x\mathrm{e}^{\mathrm{j}\kappa u}\,\mathrm{d}u \\
&= \tilde{R}_s(k)\int \mathrm{e}^{\mathrm{j}(\kappa-k)u}\,\mathrm{d}u \\
&= \tilde{R}_s(k)\delta(k-\kappa),
\end{aligned} \tag{B.2}$$

where the last equality follows from the definition of the delta function. Furthermore, since $s(x)$ is a circular complex process, then by the Fourier inversion theorem $\tilde{s}(k_x)$ is also a circular complex process. Thus, the wavenumber components of $\tilde{s}(k_x)$ are uncorrelated.

This chapter has been published as A. Theodosiou and P. López-Dekker. 'On the Sensitivity to Height and Motion of Bistatic SAR Interferometry: A Spectral View'. In: *IEEE Transactions on Geoscience and Remote Sensing* 62 (2024), pp. 1–12

C

The Geometric Method for Calculating the Sensitivity

In the case of bistatic SAR, where the transmitter has position vector $\mathbf{r_t}$ and the receiver has position vector $\mathbf{r_r}$, the line of sight to a point on the surface $\mathbf{r_p}$ is

$$\mathbf{l_e} = \frac{\mathbf{r_t} - \mathbf{r_p}}{\|\mathbf{r_t} - \mathbf{r_p}\|} + \frac{\mathbf{r_r} - \mathbf{r_p}}{\|\mathbf{r_r} - \mathbf{r_p}\|}. \tag{C.1}$$

We define the monostatic equivalent as the system that would observe a given point with the same line of sight as the bistatic SAR. Thus, the line of sight of the monostatic equivalent is parallel to $\mathbf{l_e}$. We position the monostatic equivalent at the intersection of the line that starts at $\mathbf{r_p}$ and follows $\mathbf{l_e}$, and the line segment that connects the transmitter and receiver. Thus, we can find the position of the monostatic equivalent by solving the following system of equations

$$\mathbf{r_p} + s\mathbf{l_e} = \mathbf{r_t} + q(\mathbf{r_r} - \mathbf{r_t}) \tag{C.2}$$

where s, and q are the unknowns to solve for.

$\mathbf{r_p}$ varies with look angle and time, while the positions of the transmitter and receiver vary with time only. Thus, (C.2) has a unique solution for each combination of look angle and time. Consequently, each resolution cell in the SAR signal will have a corresponding pair of monostatic equivalents, one for each receiver.

Once the two monostatic equivalents for a given resolution cell are found, the relative position vector of the two equivalent systems is

$$\Delta\mathbf{r_e} = \mathbf{r_{e2}} - \mathbf{r_{e1}}, \tag{C.3}$$

where $\mathbf{r_{e2}}$ is the position of the equivalent system of the transmitter with the second receiver, and $\mathbf{r_{e1}}$ that of the transmitter with the first receiver. We use the relative

This chapter has been published as A. Theodosiou and P. López-Dekker. 'On the Sensitivity to Height and Motion of Bistatic SAR Interferometry: A Spectral View'. In: *IEEE Transactions on Geoscience and Remote Sensing* 62 (2024), pp. 1–12

position of the equivalent systems to calculate the effective along-track baseline [59]

$$B_{\parallel} = -\Delta \mathbf{r}_{\mathbf{e}_T} + \Delta \mathbf{r}_{\mathbf{e}_N} \frac{\mathbf{l}_{\mathbf{e}_T}}{\mathbf{l}_{\mathbf{e}_N}}, \tag{C.4}$$

where the subscripts T and N denote the tangential and normal component of the vector respectively. The temporal lag between acquisitions is equal to the effective along-track baseline divided by the flight speed of the satellite.

The perpendicular baseline of the interferometer is

$$B_{\perp} = \Delta \mathbf{r}_{\mathbf{c}} \cdot \hat{\zeta}, \tag{C.5}$$

where $\Delta \mathbf{r}_{\mathbf{c}} = (\Delta \mathbf{r}_{\mathbf{e}_N} \mathbf{l}_{\mathbf{e}_T} / \mathbf{l}_{\mathbf{e}_N}, \Delta \mathbf{r}_{\mathbf{e}N}, \Delta \mathbf{r}_{\mathbf{e}R})^T$ is the relative position after shifting the two equivalent systems to align their lines of sight. We use the perpendicular baseline to calculate the sensitivity to height of the interferometer using the conventional relation [50, 51]

$$\frac{\partial \phi}{\partial h} = \frac{2\pi \|\mathbf{l}_{\mathbf{e}}\| B_{\perp}}{\lambda_0 R_s \sin \theta_i}, \tag{C.6}$$

where in this case the slant range R_s is equal to the slant range from the position of the monostatic equivalent to the resolution cell, and the incidence angle θ_i is the angle formed by the bistatic line of sight and the normal to the surface.

The careful reader would have noticed that the sensitivity is scaled by the modulus of the bistatic line of sight. It effectively scales the wavelength by the inverse of the modulus of the bistatic line of sight. The scaling arises because the modulus of the bistatic line of sight is smaller than the modulus of the monostatic line of sight. While the monostatic, two-way line of sight has a modulus of 2, the bistatic line of sight is smaller than that by the cosine of half the bistatic angle. The smaller modulus scales the wave vector. Hence, where the monostatic wave vector would have a modulus of $2k_0$, the bistatic wave vector would have a modulus of $\|\hat{\mathbf{l}_{\mathbf{T_i}}} + \hat{\mathbf{l}_{\mathbf{R_i}}}\| k_0$, effectively scaling the wavenumber, thus the wavelength.

An alternative for the incidence angle is to calculate it based on the elevation vector and the normal to the surface

$$\theta_i = \arcsin\left(\hat{\zeta} \cdot \hat{\mathbf{n}}\right). \tag{C.7}$$

The two definitions of θ_i are congruent for a monostatic system with line of sight in the zero-Doppler direction.

Figure C.1 shows the relative difference between the spectrally-derived sensitivity and the sensitivity obtained with the geometric method according to (C.6). For this result, we replaced $\|\mathbf{l}_{\mathbf{e}}\|$ by 2 and used (C.7) for θ_i. Comparing the results with Figure 3.10 shows that ignoring the scaling due to the bistatic wave vector, and instead modeling the system as a monostatic interferometer, produces a markedly less accurate result.

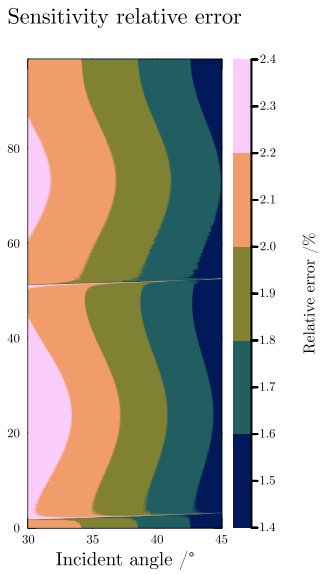

Figure C.1.: The relative error of the sensitivity calculated using the wavenumber method with respect to the conventional sensitivity expression. For the expression of the sensitivity, the incidence angle is computed according to (C.7) and the scaling of the wavelength described in (C.6) is omitted. A scaling factor of 2, corresponding to a monostatic system, is used instead.

Acknowledgments

Beginnings and ends are difficult. I did not, and still don't, know where to start a PhD, and there were many times during the last six years when the end seemed elusive. Similarly, I do not know how to begin this last chapter. What I do know is that I wouldn't like to begin before taking the time to, somewhat impersonally, acknowledge those who have, and continue to, pave the way for people like me to be able to move freely, live safely, and have the privilege to work on interesting problems. Science and technology are inherently social, and research can only be conducted within a society that has the structures to enable it.

First, I acknowledge my supervisor, Paco. Little did I know that six years ago when Klaus stepped into my office asking me if I wanted to work on a future Earth observation mission, I would end up here. I only knew that I was interested, and the subsequent interview with you convinced me that STEREOID was what I should be working on. I started knowing nothing about remote sensing, or oceanography, and I left knowledgeable, perhaps more than knowledgeable although I will let the committee decide. I have learned during my PhD that the most valuable thing is time, and you offered it generously. You gave me time to learn, to experiment, to develop ideas. Even when you knew what the answer was, you appreciated that I had to derive it myself before feeling convinced, and you were happy to let me do it. You even gave me time to come to the realization that I actually wanted a PhD. I will miss our end-of-the-day chats, and I will vividly remember our drive on Mulholland Drive and our trip to New Orleans. On top of all this, you gave me the opportunity to work on Harmony alongside many talented people.

Secondly, I would like to thank my promoter, Ramon, for his meticulous approach to science and language, which has influenced my work. Thanks to Marcel, for teaching me most of what I know about oceanography, for the companionship, the endless discussions about viruses, vaccines, and the immune system during the pandemic, and for always reminding me that few things are actually worth stressing over. "Do what Marcel would do" was the unofficial motto among the PhDs of our group. You still can't rebase your code to save your life though.

I sincerely thank my colleagues in the radar group for the companionship during these years. Tina, you were the first person that greeted me when I moved to the PhD room. Our discussions on staying sane and finishing our PhDs helped me get through it. Yan and Owen thank you for the companionship, for cheering me up when I was frustrated, and I'm sorry for *always* being late. You made the office fun and worth coming to work for.

Thanks to Lucile Gaultier and Dr. Fab of OceanDataLab. Developing the scientific workbench with them was a fun and rewarding experience. I thank Lorenzo Iannini for the interesting discussions on polarimetry.

At the TU Delft Department of Geoscience and Remote Sensing, I would like to thank Debbie, Lidwien, Natascha, and Cindy for helping me with administrative matters and for putting up with me never filling in my timesheets on time. Thank you to Prof. Hoogeboom for his constructive feedback during the first years of my PhD. I would like to thank my fellow doctoral candidates and postdocs for creating a warm and fun atmosphere to work in. The PhD room is special; there's a reason many of us never moved out.

Pau Prats-Iraola of DLR deserves to be acknowledged for sitting down with me after my presentation at IGARSS in Athens and discussing my implementation of multisquint. Your insights were valuable, and I made more progress after that quick lunch than I had made in the many weeks before. Thank you to the committee members Jordi Mallorqui Franquet, Delwyn Moller, Marc Rodríguez-Cassolà, Stefano Tebaldini, and Alex Yarovoy for reading my work and for the constructive feedback.

I'm thankful for my lifelong friends Chris, Panayiotis, Victoras, and Xenophon who have stood by me and supported me. Thank you to Simon and Lena for the company during the last years.

A sincere thank you to my family for encouraging me to keep going. Finally, I thank Kasia for her patience, her dedication during the last six years, and for putting up with my chaotic–lack of–organization and absent-mindedness. I also thank her for reminding me to not get lost in my work and that there's more to life than satellites, currents, and waves.

Curriculum Vitæ

Andreas Theodosiou

Andreas Theodosiou was born in Nicosia, Cyprus, in 1993. He received the Bachelor of Arts and Master of Engineering degrees in Electrical and Information Sciences from the University of Cambridge, in 2018. He is currently working as a Mission Performance Engineer at the European Space Agency in Noordwijk, the Netherlands, where he is involved in the Harmony and ROSE-L missions.

From 2018 to 2019, he was with the RF Payloads Section, of the European Space Agency. In 2019, he joined the Faculty of Civil Engineering and Geoscience, Delft University of Technology, to work on performance models for the, at the time, Earth Explorer 10 candidate mission, Harmony. Despite his insistence that he was not interested in a PhD, in 2021 he started his PhD project at the Department of Geoscience & Remote Sensing of the Delft University of Technology. His research interests include future SAR mission concepts and ocean remote sensing.

List of Publications

Published

3. A. Theodosiou and P. López-Dekker. 'On the Sensitivity to Height and Motion of Bistatic SAR Interferometry: A Spectral View'. In: *IEEE Transactions on Geoscience and Remote Sensing* 62 (2024), pp. 1–12

2. A. Theodosiou, M. Kleinherenbrink and P. López-Dekker. 'Wide-Swath Ocean Altimetry Using Multisatellite Single-Pass Interferometry'. In: *IEEE Transactions on Geoscience and Remote Sensing* 61 (2023), pp. 1–21

1. M. Kleinherenbrink, A. Korosov, T. Newman, A. Theodosiou, A. S. Komarov, Y. Li, G. Mulder, P. Rampal, J. Stroeve and P. Lopez-Dekker. 'Estimating Instantaneous Sea-Ice Dynamics from Space Using the Bi-Static Radar Measurements of Earth Explorer 10 Candidate Harmony'. In: *The Cryosphere* 15.7 (6th July 2021), pp. 3101–3118

In Review

1. A. Theodosiou and P. López-Dekker. 'Data-Driven Phase Synchronisation of Harmony's Ocean Surface Topography Product'. In: *IEEE Transactions on Geoscience and Remote Sensing* (2025)